

**GULF GENERAL ATOMIC**

GULF-GA-A12242

**STUDY OF RADIOISOTOPE SAFETY DEVICES FOR
ELECTRIC PROPULSION SYSTEM****VOLUME II - FINAL REPORT**

by

G. B. Bradshaw, W. G. Homeyer, F. D. Postula,
and E. J. Steeger

(NASA-CR-114506) STUDY OF RADIOISOTOPE
SAFETY DEVICES FOR ELECTRIC PROPULSION
SYSTEM, VOLUME 2: FINAL REPORT G.B.
Bradshaw, et al (Gulf General Atomic)
6 Oct. 1972 148 p

N73-10746

Unclas
46092

CSCL 21C G3/28

Prepared under Contract No. NAS 2-5891 by
GULF GENERAL ATOMIC COMPANY
San Diego, California

for

AMES RESEARCH CENTER
NATIONAL AERONAUTICS AND SPACE ADMINISTRATION

October 6, 1972

GULF GENERAL ATOMIC COMPANY
P.O. BOX 608, SAN DIEGO, CALIFORNIA 92112



GULF GENERAL ATOMIC

GULF-GA-A12242

STUDY OF RADIOISOTOPE SAFETY DEVICES FOR ELECTRIC PROPULSION SYSTEM

VOLUME II - FINAL REPORT

by

G. B. Bradshaw, W. G. Homeyer, F. D. Postula,
and E. J. Steeger

Prepared under Contract No. NAS 2-5891 by
GULF GENERAL ATOMIC COMPANY
San Diego, California

for

AMES RESEARCH CENTER
NATIONAL AERONAUTICS AND SPACE ADMINISTRATION

Gulf General Atomic Project 2113

October 6, 1972

GULF GENERAL ATOMIC COMPANY
P.O. BOX 608, SAN DIEGO, CALIFORNIA 92112

CONTENTS

| | | |
|--------|--|----|
| 1. | SUMMARY | 1 |
| 2. | INTRODUCTION | 3 |
| 3. | SYMBOLS | 5 |
| 4. | REFERENCE DESIGN | 7 |
| 4.1 | Flight Configuration | 12 |
| 4.1.1 | Heat Source | 13 |
| 4.1.2 | Radioisotope Capsule | 17 |
| 4.1.3 | Converter Assembly | 20 |
| 4.1.4 | Emitter Heat Pipe | 20 |
| 4.1.5 | Thermionic Converters | 23 |
| 4.1.6 | Space Radiator | 24 |
| 4.1.7 | Neutron Shield | 24 |
| 4.1.8 | Electrical Connections | 25 |
| 4.1.9 | Transmission Lines and Boom | 25 |
| 4.1.10 | Power Conditioning | 27 |
| 4.2 | Safety Equipment | 28 |
| 4.2.1 | Auxiliary Cooling System | 30 |
| 4.2.2 | Neutron Shielding | 30 |
| 4.2.3 | Secondary Containment Vessel | 32 |
| 4.2.4 | Reentry Shield and Aerodynamic Flare | 33 |
| 4.2.5 | Impact Energy Absorber | 33 |
| 4.2.6 | Structural Components and Blast Shield | 33 |
| 4.2.7 | Launch Pad Fire Protection System | 35 |
| 4.3 | Operating Sequence | 35 |
| 4.3.1 | Final Assembly of the Launch Configuration | 35 |
| 4.3.2 | Assembly and Disassembly for Testing | 36 |
| 4.3.3 | Launch and Flight | 37 |
| 4.4 | System Mass and Power Supply | 37 |

| | | |
|---------|---|----|
| 5. | AEROSPACE NUCLEAR SAFETY | 41 |
| 5.1 | Safety Criteria | 41 |
| 5.2 | Launch Pad Explosion and Fire | 43 |
| 5.2.1 | Launch Pad Thermal Environment | 43 |
| 5.2.2 | Fragment Environment | 49 |
| 5.2.3 | Overpressures | 52 |
| 5.3 | Reentry and Aerothermodynamics | |
| 5.3.1 | Abort Environments | 53 |
| 5.3.2 | Safety Requirements | 53 |
| 5.3.3 | Design Criteria | 54 |
| 5.3.4 | Reentry Heating | 54 |
| 5.3.5 | Thermal Protection System | 54 |
| 5.4 | Impact on Water | 55 |
| 5.5 | Land Impact | 56 |
| 5.6 | Location and Recovery Aids | 57 |
| 6. | SAFETY DESIGN ANALYSES | 59 |
| 6.1 | Launch Pad Fire Analysis | 59 |
| 6.1.1 | Transient Thermal Analysis Model | 59 |
| 6.1.2 | LiH/Zirconia Heat Storage - Insulator Fire Shield . | 61 |
| 6.1.3 | Alternate Fire Protection Concepts | 72 |
| 6.1.3.1 | Heat Storage Materials | 72 |
| 6.1.3.2 | Thermal Switch Composite Materials | 74 |
| 6.1.3.3 | Thermal Expansion Radiation Shields | 76 |
| 6.1.4 | Auxiliary Radiator Heat Pipes | 78 |
| 6.2 | Blast Shielding | 81 |
| 6.3 | Reentry Design Analysis | 84 |
| 6.3.1 | Aeroballistics | 84 |
| 6.3.1.1 | Abort Configurations | 84 |
| 6.3.1.2 | Aerodynamic Design | 89 |
| 6.3.1.3 | Reentry Trajectories | 93 |

| | | |
|---------|--|-----|
| 6.3.2 | Aerothermodynamics | 93 |
| 6.3.2.1 | Aerodynamic Heating | 93 |
| 6.3.2.2 | Shock Layer Radiation | 98 |
| 6.3.2.3 | Separated Flow Heating | 102 |
| 6.3.3 | Thermal Protection System | 102 |
| 6.3.3.1 | Heat Shield Selection | 102 |
| 6.3.3.2 | Structural Temperatures | 107 |
| 6.3.3.3 | Graphite Ablation | 111 |
| 6.4 | Terminal Velocity Impact Systems | 111 |
| 6.4.1 | Aerodynamic Flare/Honeycomb | 111 |
| 6.4.2 | Alternate Energy Absorption System | 117 |
| 6.4.3 | Earth Impact Burial | 119 |
| 6.4.3.1 | System Burial | 119 |
| 6.4.3.2 | Heat Source Temperatures | 120 |
| 6.4.3.3 | Auxiliary Radiator Temperatures | 120 |
| 6.4.4 | Effect of Impact on Fuel Form | 123 |
| 6.5 | Radiation Shielding Tradeoffs | 123 |
| 7. | LIFETIME LIMITING MECHANISM | 129 |
| 7.1 | Effect of Oxygen on the Fuel Capsules | 129 |
| 7.2 | Effect of Oxygen on the Emitter Heat Pipes | 130 |
| 7.3 | Test Program to Determine Oxygen Effects | 131 |
| 8. | COST ESTIMATES | 133 |
| 9. | CONCLUDING SECTION | 135 |

FIGURES

| | | |
|-----|---|----|
| 4.1 | Radioisotope Thermionic Power Supply - Launch Configuration | |
| a) | Overall View | 8 |
| 4.1 | Radioisotope Thermionic Power Supply - Launch Configuration | |
| b) | Detailed View | 9 |
| 4.2 | Separation of Safety Equipment From Flight System | 10 |

| | | |
|------|--|-------|
| 4.3 | Flight Configuration | 14 |
| 4.4 | Portion of Heat Source Including Heat Pipes | 15 |
| 4.5 | Heat Source Door | 18 |
| 4.6 | Isotope Fuel Capsule | 19 |
| 4.7 | Thermionic Converter | 21 |
| 4.8 | Electrical Network | 26 |
| 4.9 | Basic Power Conditioning Module Circuit | 29 |
| 4.10 | Overall Dimensions of Launch Configuration | 39 |
| 5.1 | Liquid Propellant Fireball Radiant Heat Flux and Temperature for a Titan III Launch Abort | 48 |
| 5.2 | Upward Fragment Velocities From 25,000-Pound Project PYRO Experiments (10 Feet From Top Dome) | 50 |
| 5.3 | Upward Fragment Velocities From 25,000-Pound Project PYRO Experiments (10 Feet From Top Dome) | 50 |
| 6.1 | Thermal Model Geometry for the Radioisotope Propulsion Systems Reference Design | 60 |
| 6.2 | Tradeoff of Fire Shield Mass and Equilibrium ΔT with LiH Shield Thickness | 64 |
| 6.3 | Transient Temperature Profiles of RTPS Components During a Launch Pad Fire | 67 |
| 6.4 | Transient Temperature Profiles of RTPS Components During a Launch Pad Fire | 68 |
| 6.5 | Transient Thermal Response of Auxiliary Radiator Heat Pipes and Thermal Switching Shield in a 2616°K Launch Pad Fire . . . | 75 |
| 6.6 | Transient Thermal Response of the Auxiliary Radiator Heat Pipes Surrounded by Radiation Shields and Exposed to a Launch Pad Fire | 79 |
| 6.7 | Potassium Vapor Pressure, Auxiliary Radiator Heat Pipe Stress and Material 1000-hour Rupture Stress as a Function of Heat Pipe Temperature | 80 |
| 6.8 | Effect of Heat Pipe Maximum Operating Temperature on Wall Thickness for 1000-hour Rupture Criteria | 82 |
| 6.9 | Probable Abort Configurations | 85-86 |
| 6.10 | Drag Coefficient vs Flare Angle | 89 |
| 6.11 | Variation of Aeroballistic Parameters With Flare Size | 91 |
| 6.12 | Drag Coefficient and Heating Rate Changes With Increases in Safety System Mass and Diameter | 92 |

| | | |
|------|---|-----|
| 6.13 | Overall Dimensions of Reentry Vehicle | 94 |
| 6.14 | Reentry Trajectory Profiles | 95 |
| 6.15 | Comparison of Reentry Heating at Stagnation Point | 99 |
| 6.16 | Variation of Maximum Stagnation Heating With Entry Angle at Escape Velocity | 101 |
| 6.17 | Comparison of Magnitude of Aerodynamic and Radiative Heating for a Reentry Vehicle at 200,000 Feet | 101 |
| 6.18 | Wedge Induced Separated Flows | 103 |
| 6.19 | Effect of Separated Flow on Heating | 103 |
| 6.20 | Thermal Protection System Computer Model | 108 |
| 6.21 | Comparative Transient Temperatures | 110 |
| 6.22 | Mass Transfer Regimes for Ablating Graphite | 112 |
| 6.23 | Normalized Hypersonic Ablation Rate of Graphite Over the Entire Range of Surface Temperature | 112 |
| 6.24 | Stagnation Point Ablation | 113 |
| 6.25 | Thickness of Honeycomb Energy Absorption Material With Sea Level Terminal Velocity | 115 |
| 6.26 | Tradeoff of RTPS Aerodynamic Flare Mass and Honeycomb Energy Absorber Mass With Flare Diameter | 117 |
| 6.27 | Post Impact Temperature of Auxiliary Radiator Versus Radiator Diameter | 123 |
| 6.28 | Radial Dose Rates From Heat Source After Impact Versus Increase in Mass | 126 |
| 6.29 | Sea Level Terminal Velocity Changes With Increase in Safety System Mass and Diameter | 128 |

TABLES

| | | |
|-----|--|----|
| 4.1 | Thermal Insulation Data | 16 |
| 4.2 | Parameters of Emitter Heat Pipes | 22 |
| 4.3 | Converter Parameters | 23 |
| 4.4 | Parameters for Space Radiator | 24 |
| 4.5 | Power Conditioning Parameters | 28 |
| 4.6 | Auxiliary Heat Pipe Parameters | 31 |
| 4.7 | Structural Components (All Material -- SS 316) | 34 |

| | | |
|------|---|-------|
| 4.8 | System Component Masses | 40 |
| 4.9 | Electrical Performance Parameters | 38 |
| 5.1 | RTPS Safety Package Subsystems | 42 |
| 5.2 | Safety Design Standards for the Transit Heat Source | 44-45 |
| 5.3 | Summary of Composite Abort Environments for the MHW Heat Source | 46 |
| 5.4 | Radiant Heat Input to Safety System From Launch Pad Fire . . . | 47 |
| 5.5 | Fragment Environments | 51 |
| 5.6 | Location and Recovery Aid Design Characteristics | 58 |
| 6.1 | Launch Pad Abort Transient Thermal Analysis Model Parameters . | 62 |
| 6.2 | Summary of Transient Heat Pipe Temperatures During a Launch Pad Fire of 2600 K for 10 Minutes | 66 |
| 6.3 | RTPS System Temperatures From Transient Thermal Analysis Computer Print Out (0.12" Insulation, 2600°K, 10 Minute Fire) | 69 |
| 6.4 | RTPS System Temperatures From Transient Thermal Analysis Computer Print Out (0.12" Insulation, 2600°K, 10 Minute Fire) | 70 |
| 6.5 | Characteristics of the Revised LiH/Zirconia Launch Pad Abort Fire Shield (2600°K Fire, 10 Minutes) | 71 |
| 6.6 | Characteristics of Heat Storage Material to Protect the Safety System Radiator From a Launch Pad Fire | 73 |
| 6.7 | Preliminary Design Characteristics of a Thermal Switch Composite Shield for Launch Day Fire Protection | 77 |
| 6.8 | Comparison of Various Blast Shield Materials | 83 |
| 6.9 | Possible Abort Conditions | 88 |
| 6.10 | Maximum Reentry Heating Summary | 100 |
| 6.11 | Carbon/Graphite Fibrous Composites | 105 |
| 6.12 | Comparison of Properties of Carbon/Graphite Fiber Composites and Bulk Graphite | 106 |
| 6.13 | Maximum Reentry Temperatures | 109 |
| 6.14 | Characteristics of the Honeycomb Energy Absorption System Without Parachutes | 116 |
| 6.15 | Frangible Tube Design Without Parachutes | 119 |
| 6.16 | Computed Burial Depth for Terminal Velocity Impact of the RTPS Onto Various Soils | 122 |
| 6.17 | Summary of Design Characteristics for 200 kg Increase in Safety System Mass Case | 129 |

1. SUMMARY

Continued studies of a radioisotope-thermionic power supply for electric propulsion to the outer planets focused on the safety equipment to protect against dispersal of the isotopic fuel. The safety equipment is designed to be separated from the power supply and jettisoned early in the heliocentric phase of the mission, as soon as Earth escape is verified. Because of this, the mass of the safety equipment has little effect on the mass of the payload delivered to the target planet. The objective of this study was to improve the reliability of the safety equipment and increase safety margins at the expense of some increase in mass.

A new reference design was prepared for the 5 kW(e) thermionic power supply fueled with 44.2 kW(t) of $^{244}\text{Cm}_2\text{O}_3$. The safety equipment in this design is a passive containment system which does not rely on the operation of any mechanisms such as a launch escape rocket or deployment of parachutes. It includes: (1) a blast shield to protect against the explosion of the launch vehicle; (2) a combination of refractory thermal insulation and heat storage material to protect against a sustained launch pad fire; (3) a reentry body with a spherical nose and a large (2.44 m diameter) conical flare at the aft end to stabilize the reentry attitude and lower the terminal velocity in air; (4) composite graphite thermal protection to sustain the reentry heat pulse; (5) crushable honeycomb behind the nose to limit (to 200 G's) the deceleration of the radioisotope source due to impact on land at terminal velocity; (6) a double-walled secondary containment vessel surrounding the isotopic capsules; (7) neutron shielding to reduce external dose rates; and (8) an auxiliary cooling system employing redundant heat pipes to remove the radioactive decay heat from the heat source and reject it to the surroundings or to a forced convection loop. Items 1, 2, 3, and 5 were added or modified during this phase of the study to replace the escape rockets and parachutes considered in the previous phase. The mass of the

power supply is 724 kg at launch, 575 kg of which is jettisoned after the Titan III-D/Centaur launch vehicle has boosted the power supply to an escape trajectory.

The potential for achieving the 36,000-hour lifetime required for some missions was also studied. The Cm_2O_3 capsules (at 2030°K surface temperature) and emitter heat pipes (at 1900°K) are expected to be the limiting components. The effect of oxygen released from the capsules by diffusion through the walls and through the helium vent plug was studied. It was shown that oxygen-induced sublimation of tungsten could remove as much as 0.2 mm from the surface of the fuel capsules in 36,000 hours, but that the loss rate would probably be much less. It was estimated that oxygen permeating the walls of the capsules and heat pipes could oxidize as much as 70 mg of lithium in each heat pipe. The calculations showed that there are large uncertainties in estimating oxygen effects from existing data, but that there is considerable flexibility in the reference design to minimize the effects of oxygen by use of gettering and other techniques.

This study showed the feasibility of protecting a 44.2 kW (1.3×10^6 Curie) source of ^{244}Cm from dispersal during launch accidents. Further work is necessary to establish the technology for long-lived radioisotope capsules and emitter heat pipes. Once the technology is established and lifetime and performance limits are defined, it will be possible, with the help of detailed development plans and cost estimates, to make a more well-founded decision whether this system should be developed for some electric propulsion missions to the outer planets or the deep space environment.

2. INTRODUCTION

A recent study (Ref. 1) examined in preliminary fashion the suitability of an isotope-thermionic power supply for electric propulsion to the outer planets. The main feature was a separable entry safety container which was discarded early in the sun-centered part of the flight. The reference design case was a 5 kW(e) system using a Curium-244 heat source. Because of the preliminary nature of the study, various power levels and system configurations were examined in limited detail.

As the first phase of this study came to a close, frequent mission analyses were carried out using the latest values for estimated power and propulsion system masses. These calculations indicated that in spite of the weight growth during the first phase of the study, the system was still of interest for propulsive application. Furthermore, some of the mission parameters, such as payload, were rather insensitive to some of the propulsion system mass values such as the mass of the separable safety equipment. This meant that continued work could take advantage of these insensitivities to make the design generally more convincing from an engineering and safety viewpoint. Also, a more detailed look at a specific design concept with fewer alternatives could now be justified. As a result of changes in cost and subsystem mass that evolved during the first phase of the contract, such items as the nominal mission target and mission duration were changed for this second phase.

In the continued study effort reported here, the goal was to consider methods by which the separable safety equipment defined in the previous study could be modified to improve the aerospace nuclear safety aspects of the concept. Because these subsystems have low or negligible effect on the mission payload, considerable mass increases could be tolerated. Also, a more detailed examination was made of some of the lifetime and material

compatibility problems as well as unique orbital and superorbital abort possibilities.

As a result of these studies, the reference design reported previously (Ref. 1) was modified substantially. The principal modification was to eliminate the launch escape rocket and parachute systems and replace them with thermal insulation and heat storage materials, a blast shield, an enlarged aerodynamic flare, and a thickened crushable honeycomb section in the nose of the reentry body. The new design is described in Section 4. It is based on the following mission and system constraints:

| | |
|------------------|---------------------|
| Radioisotope | ^{244}Cm |
| Power | 5 kW(e) |
| Mission Duration | 36,000 hours |
| Launch Vehicle | Titan III D-Centaur |

The full power level of 5 kW(e) is required during the first 10,000 hours and the last 10,000 hours of the mission, with low power required during the intervening 16,000 hours. The launch vehicle will inject the radioisotope electric propulsion system directly into a heliocentric trajectory with a hyperbolic speed on the order of 7.5 km/sec.

3. SYMBOLS

| | |
|-------------|--|
| a | rate of deceleration (m/sec^2) |
| A | a constant |
| A_F | projected area of the conical flare |
| A_N | projected or cross-sectional area of the nose |
| C_D | drag coefficient |
| C_{DF} | drag coefficient for the flare |
| C_{DN} | drag coefficient for the nose |
| D | a constant |
| EN^* | reference enthalpy |
| EN_f | local flow enthalpy |
| EN_r | recovery enthalpy |
| EN_w | wall enthalpy |
| F | radiant interchange factor |
| G | design deceleration limit in g's |
| h_L | laminar heat transfer coefficient, lb/hr-ft^2 |
| k | insulation conductivity in $\text{Btu/hr ft } ^\circ\text{F}$ |
| ℓ | Reynolds number length, ft |
| m | mass of fuel |
| \dot{m}_D | diffusion controlled mass loss rate, $\text{lb/ft}^2\text{-sec}$ |
| n | number of radiation shields |
| N | constant, vehicle nose performance coefficient |
| P_e | stagnation pressure, lb/ft^2 |
| P_f | local flow velocity, lb/ft^2 |

| | |
|---------------|--|
| Q_i | heat flux, B/ft ² hr |
| Q_{rad} | radiant heat flow through the shields |
| Q_S | aerodynamic heating rate |
| R_N | nose radius, ft |
| S | soil constant, depends on specific soil conditions |
| t | thickness in inches |
| t_∞ | freestream velocity, fps |
| U_f | local flow velocity, fps |
| V | impact velocity, fps |
| V_∞ | freestream velocity, fps |
| V_T | terminal velocity |
| W | a constant |
| β | hypersonic ballistic coefficient flare angle taken as 45° |
| ρ | density of air at a specified altitude |
| ρ_∞ | freestream density, lb/ft ³ |
| $\rho^*\mu^*$ | "Reference" density and viscosity |
| $\rho_b\mu_b$ | base value density and viscosity |
| σ | Stefan-Boltzmann constant |

4. REFERENCE DESIGN

The reference design of the radioisotope power supply is shown in Fig. 4.1. The launch configuration shown here consists of three subassemblies. These are the radioisotope heat source, the thermionic converter assembly, and the safety equipment. The safety equipment is jettisoned after the power supply is launched into a hyperbolic trajectory relative to the earth. This leaves the flight configuration which consists of the heat source and converter assembly. The separation of the safety equipment from the flight configuration is illustrated in Fig. 4.2.

As shown in Fig. 4.1, the radioisotope heat source consists of the radioisotope capsules and the capsule holder. The capsule holder is covered with thermal insulation to reduce heat leakage. The thermionic converter assembly consists of:

1. The emitter heat pipes which remove heat from the radioisotope capsules and concentrate it in the thermionic converters
2. The thermionic converters, which convert a portion of the isotopic heat to electrical power
3. The electrical transmission lines which transmit the electrical power from the thermionic converters to the power conditioning equipment
4. The radiator heat pipes which reject the waste heat, not converted to electricity, to space
5. The beryllium neutron shield which protects sensitive components in the payload and power conditioning equipment from radiation damage

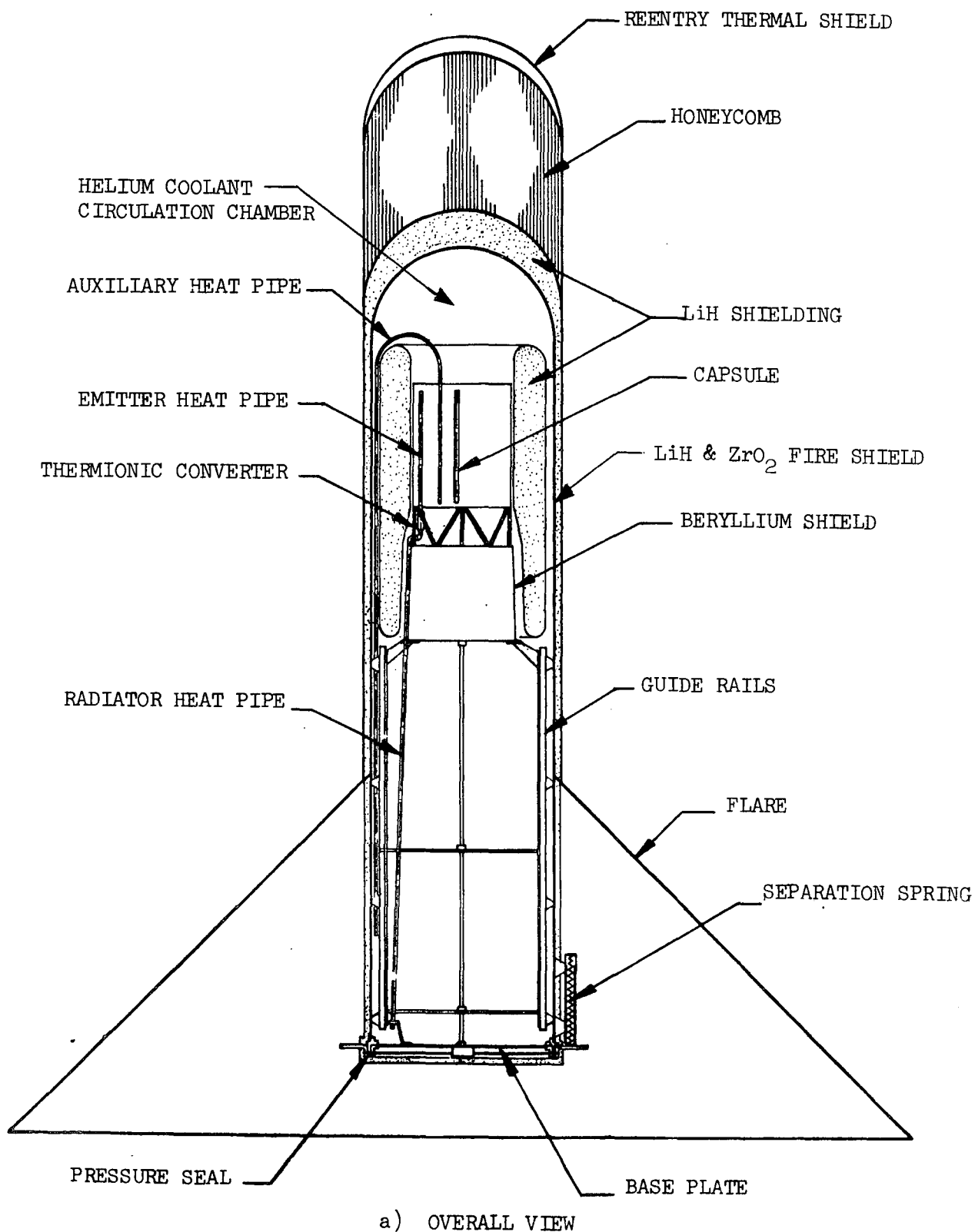


Fig. 4.1. Radioisotope thermionic power supply - launch configuration

Page intentionally left blank

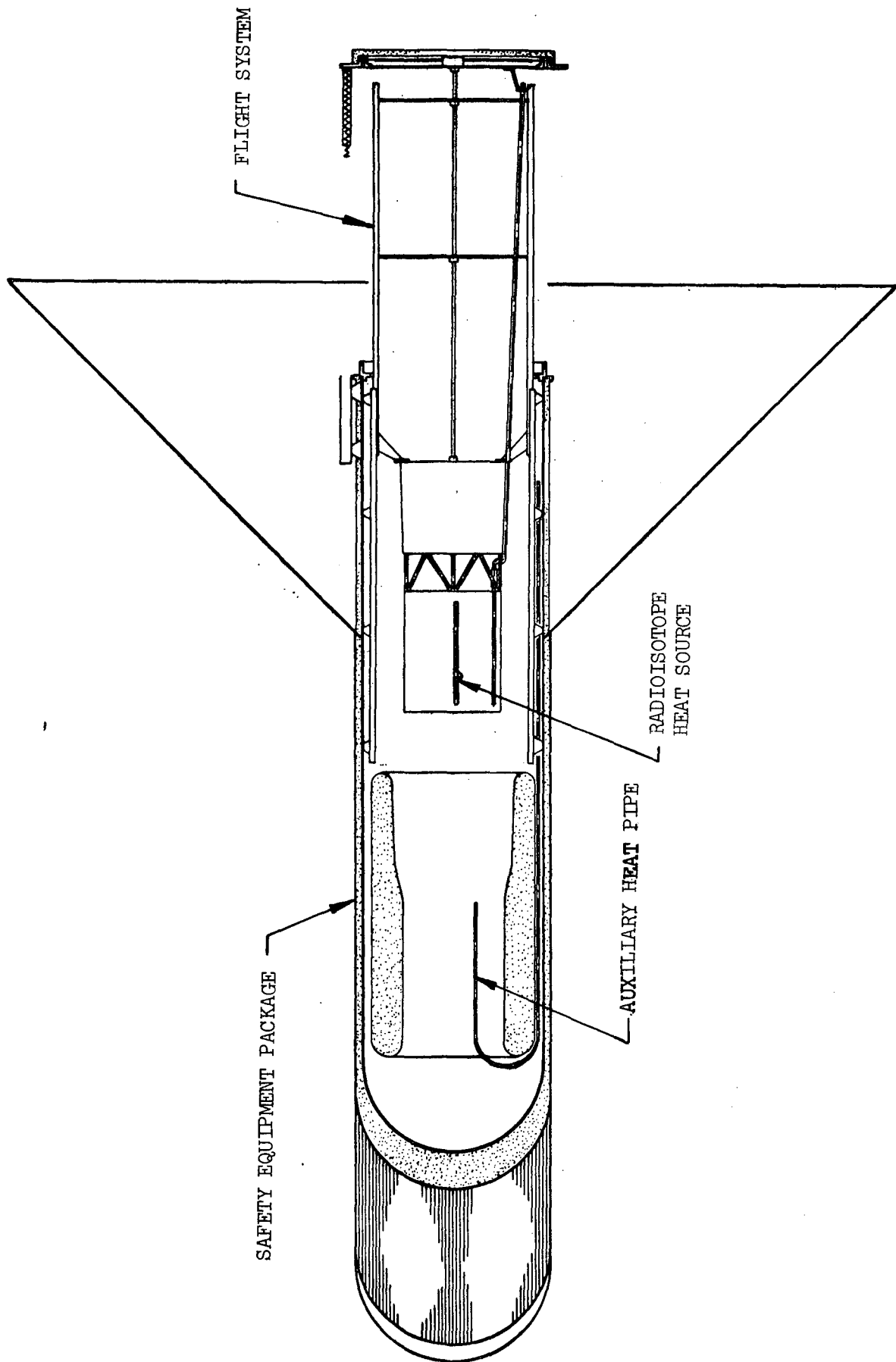


Fig. 4.2. Separation of safety equipment from flight system

6. The extendible boom which moves the radioisotope power source away from the payload and power conditioning after launch
7. The power conditioning equipment (not shown) which converts the 15 V output of the thermionic power source to the levels required by the electric thrusters.

The safety equipment includes:

1. The auxiliary cooling heat pipes which remove heat from the radioisotope capsules prior to and during the launch
2. The containment shell which provides secondary containment of the radioisotope and protects refractory metal components from oxidation in the earth's atmosphere
3. The helium container and circulator to remove isotopic heat prior to launch
4. The lithium hydride neutron shield to protect persons from neutron radiation prior to launch or following launch aborts
5. The graphite reentry shield to protect against aerodynamic heating following a high level launch abort
6. The aerodynamic flare which reduces the ballistic coefficient of the power source and assures a stable reentry attitude
7. The zirconia felt thermal insulation and lithium hydride heat absorber which protect the secondary containment shell and auxiliary cooling heat pipes from overheating during a launch pad fire

8. The impact energy absorber which protects the secondary containment shell and other safety equipment from damage during impact on the earth's surface.

The separation of the safety equipment from the heat source and converter assembly is illustrated in Fig. 4.2. This separation is performed after the power source has reached a hyperbolic trajectory and there is no longer danger of reentry into the earth's atmosphere. Actuation of separation of the safety shell from the flight configuration is by retraction of three pins at the periphery of the aft bulkhead. The pins are actuated by pressurized nitrogen stored in a small cylinder and slide in linear bearings to reduce the frictional load. Since the system is designed to withstand a launch pad fire, pyrotechnic devices for actuation or separation were ruled out.

When the pins are retracted, a separation force is supplied by three coil springs which are stored within the flare volume. During separation, the flight system is guided along three rails so no side force is applied at the moment of separation. The auxiliary cooling heat pipes slide out from between the radioisotope capsules and the emitter heat pipes as the heat source is withdrawn from the safety equipment. When the heat source is fully removed, a hinged, insulated door closes over the end from which the auxiliary heat pipes have been withdrawn, and the temperatures of the heat source and converter assembly rise to their normal operating conditions.

The individual components of the heat source, thermionic converter assembly, and safety equipment are described in detail in the following sections. Section 4.1 deals with the flight configuration, while the safety equipment is described in Section 4.2. The sequence of operations from initial checkout to final electrically propelled flight is given in Section 4.3. Section 4.4 summarizes weight and power information for the radioisotope thermionic power source.

4.1. FLIGHT CONFIGURATION

The radioisotope thermionic power source in the flight configuration is illustrated in Fig. 4.3. Heat is generated in the radioisotope capsules within the heat source. The capsules, at 2030°K, radiate their heat to emitter heat pipes having their boiler section within the heat source. The condenser end of each emitter heat pipe, which operates at 1900°K forms the emitter of a thermionic converter in which electrical power is produced. Waste heat from the collector of each thermionic cell is transferred around the beryllium neutron shield by a radiator heat pipe which radiates to space at a temperature of 1000°K.

The thermionic converters are interconnected in an electrical network. Transmission lines connect to the positive and negative terminals of the network and pass along the outside of the shield and waste heat radiator. The transmission lines are insulated from the shield and radiator and reject heat from electrical resistive losses directly to space, at a temperature of about 370°K. The transmission lines pass through the base plate of the power source to the power conditioning equipment. The power conditioning equipment and the instrument payload are separated from the radioisotope power source by a 6 meter boom to reduce radiation levels.

4.1.1 Heat Source

The heat source consists of the radioisotope capsules and the capsule holder. The capsule holder is covered with thermal insulation to reduce heat leakage from the heat source.

A portion of the heat source assembly including the emitter heat pipes is illustrated in Fig. 4.4. There are one hundred and thirty-six $^{244}\text{Cm}_2\text{O}_3$ radioisotope capsules which radiate their heat to the 69 emitter heat pipes. Shown in one sector of the illustration of the heat source in Fig. 4.4 is the configuration at launch with auxiliary cooling heat pipes inserted between the capsules and emitter heat pipes. In the launch configuration the isotopic heat is transferred to the auxiliary cooling heat pipes by a combination of radiation and conduction through the helium gas which blankets the heat source.

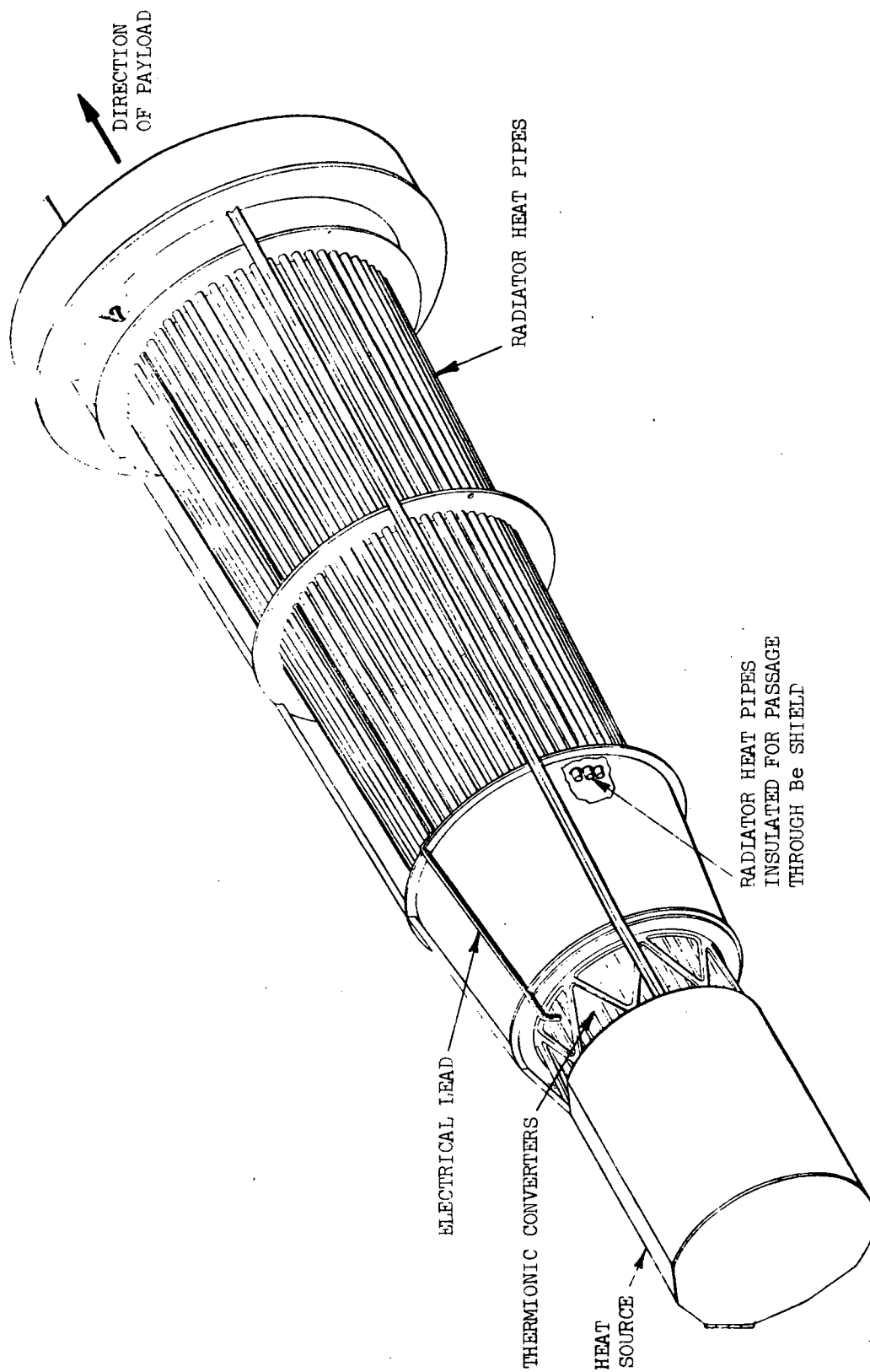


Fig. 4.3. Flight configuration

The heat source is assembled within the array of auxiliary cooling heat pipes in the safety equipment. The inner grid plate is placed over the heat pipes in the safety equipment, and the capsules are inserted into the grid plate as far as their retainer rings. After all of the capsules have been inserted, the outer grid plate is placed over the capsules and attached to the inner grid plate by screws which are located around some of the holes through which the emitter heat pipes pass (the emitter heat pipes are not present at this time).

The outer grid plate has attached to it a shroud which surrounds the array of capsules and heat pipes. The shroud and the outer grid plate are covered with multi-foil thermal insulation (Refs. 2,3). The characteristics of the thermal insulation are given in Table 4.1. The corner between the cylindrical and flat sections of insulation is made by interleaving tabs from the cylindrical section with sheets from the flat section. This method of assembly has been shown by recent experiments to minimize heat leakage from the corners (Ref. 4).

TABLE 4.1
THERMAL INSULATION DATA

| | |
|-------------------------------|--------------------------|
| Type | Multi-Foil |
| Foil material | Tungsten |
| Foil thickness | 0.0013 cm |
| Particle material | ThO ₂ |
| Most common particle sizes | 15-25 μ |
| Maximum particle size | $\sim 50 \mu$ |
| Average oxide layer thickness | 8.3 μ |
| Average oxide coating density | 0.055 mg/cm ² |

As shown in Fig 4.4, the outer grid plate is attached to structural members. The structure consists of W-25% Re studs 0.42 cm in diameter penetrating the thermal insulation which are connected to trusses. This structure supports the heat source during launch and spaces the heat source from the beryllium neutron shield in the flight configuration. Three stainless steel

rods are attached at 120° spacings to the end of the support structure which rests against the neutron shield. These rods pass over the outside edge of the neutron shield and are attached to the base plate of the converter assembly in the flight configuration. They hold the heat source against the beryllium neutron shield during electrically propelled flight.

When the safety equipment is jettisoned, the auxiliary cooling heat pipes are removed from one end of the heat source. To reduce heat leakage from this end of the heat source, an insulated door, shown in Fig 4.5, is used. The door is designed to swing shut and latch remotely. Multi-foil insulation is attached to the outside of the door. The joint between the insulation on the door and the insulation on the shroud is a tapered corner, which has been shown to allow minimum heat leakage of joints which can be made without pre-assembly (Ref. 2). The door is in three sections joined by hinges, to permit it to fit in a small space between the outside of the heat source and the inner wall of the safety equipment. The inner wall of the safety equipment is shown in phantom in Fig. 4.5. The insulation is continuous across the entire door.

4.1.2. Radioisotope Capsule

The design of the isotope capsule is shown in Fig. 4.6. The capsule is fabricated entirely of tungsten-25% rhenium alloy. This alloy has been selected because of its refractory nature, its relatively good fabricability, and its compatibility with Cm_2O_3 (Ref. 5). The capsule is fabricated by electron beam welding a bottom assembly and a retainer ring to a length of tubing. The final closure after fuel is inserted is made by TIG welding a cap into the end of the capsule. The bottom assembly consists of a foil rupture disk backed up by a porous plug. The porous plug prevents loss of fuel after the rupture disk has been ruptured by helium pressure.

The capsule was sized to allow adequate volume for helium accumulation prior to launch. It is fueled with 137 gm (325 W) of $^{244}\text{Cm}_2\text{O}_3$. It can be sealed more than 150 days before launch without excessive helium pressure buildup. When a capsule is heated to 1700°K at 150 days after sealing, the

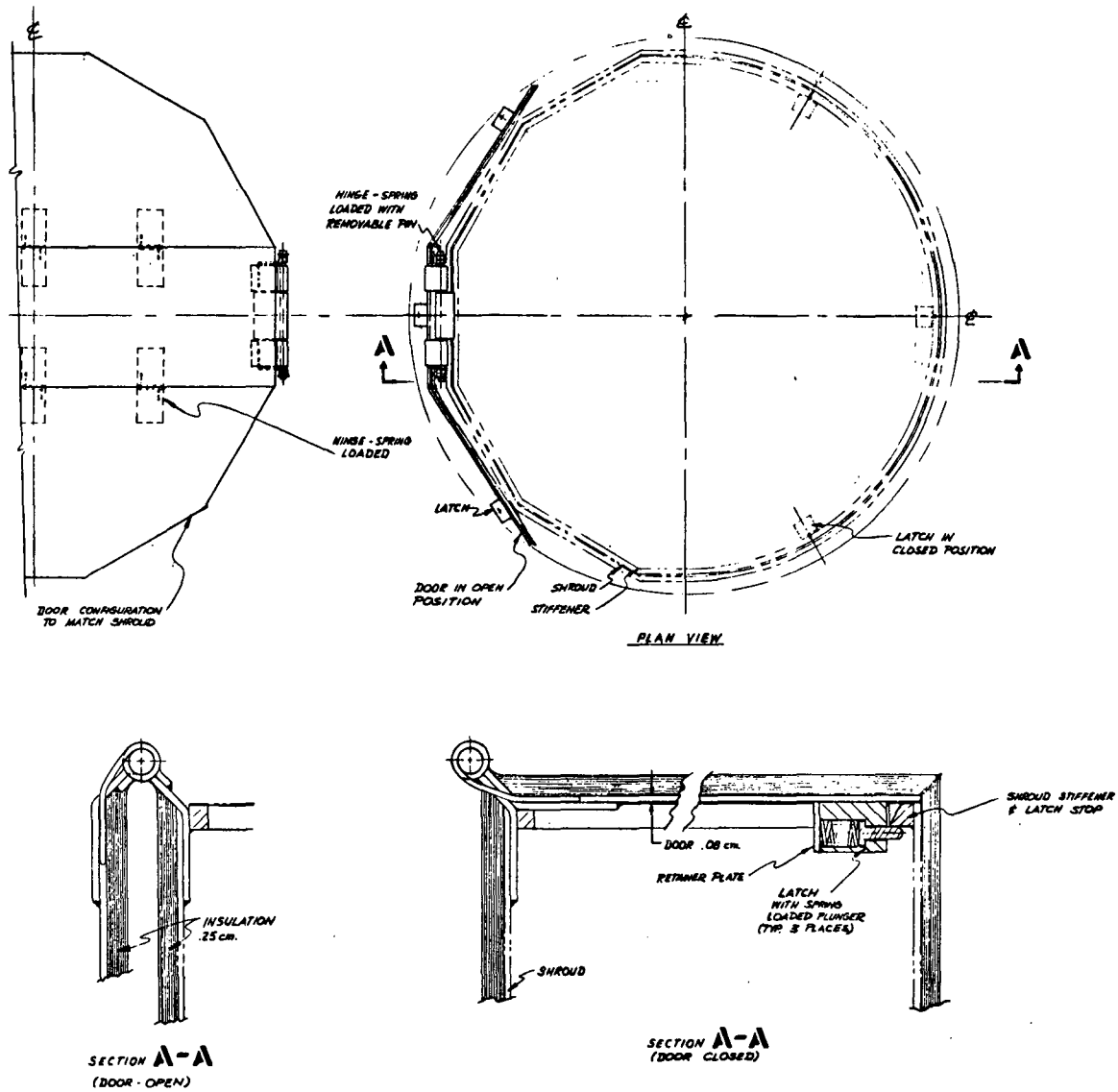


Fig. 4.5. Heat source door

stress in the walls will build up to $1.5 \times 10^8 \text{ N/m}^2$ (27,000 psi), which is only 60% of the yield strength of tungsten-25% rhenium at 1700°K. This indicates that the capsule can be sealed 150 days before launch without helium pressure causing damage.

4.1.3. Converter Assembly

The converter assembly consists of 69 thermionic converters, each attached to an emitter heat pipe to transfer heat to the thermionic emitter, a collector heat pipe to remove heat from the thermionic collector, and a radiator heat pipe to reject the waste heat to space. The converter modules are interconnected in a series-parallel network by electrical leads. Also included in the converter assembly are electrical transmission lines, a neutron radiation shield, and structure including an extendible boom.

4.1.4. Emitter Heat Pipe

The emitter heat pipe carries heat from the isotope heat source to the thermionic converter. Components of the heat pipe are illustrated in Fig. 4.7 where it is shown as the emitter of the thermionic converter. The parameters and dimensions are summarized in Table 4.2. The tungsten heat pipe is fabricated by chemical vapor deposition. The tungsten end cap is EB welded after filling the heat pipe with lithium working fluid. The porous tube, which separates the liquid and vapor, is fabricated of several layers of tungsten wire mesh, diffusion bonded together in the manner developed by Kemme (Ref. 6). In the evaporator region of the heat pipe, which is inserted inside the heat source, the surface is grooved to increase the thermal absorptivity as described in Section 5.1.1.

The condenser end of the heat pipe, which forms the emitter of the thermionic converter, is covered by a 10 mil layer of tungsten deposited by hydrogen reduction of tungsten hexachloride. The chloride-deposited tungsten is oriented with the {110} crystal planes on the surface. This produces a vacuum work function of 4.8 to 5 volts for the tungsten emitter and results in high thermionic power density and conversion efficiency (Ref. 7). A

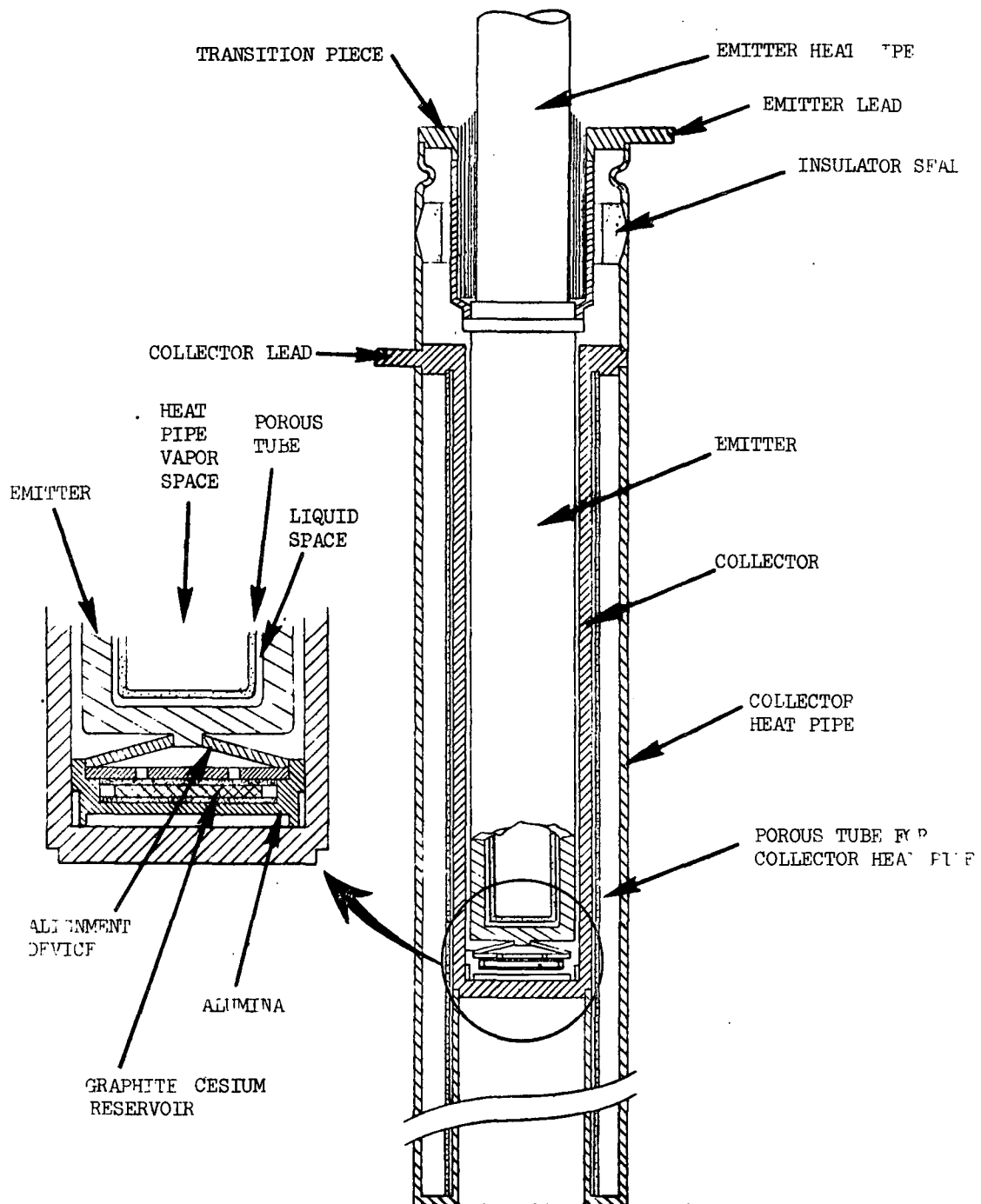


Fig. 4.7. Thermionic converter

TABLE 4.2
PARAMETERS OF EMITTER HEAT PIPES

| | |
|--|-----------------------|
| I.D. porous tube | 0.57 cm |
| O.D. porous tube | 0.60 cm |
| I.D. heat pipe wall | 0.673 cm |
| O.D. heat pipe | 0.85 cm |
| Width of annulus | 0.037 cm |
| Thermal limits of heat pipe | |
| Based upon liquid annulus | 1500 watts |
| Based upon vapor flow region | 3000 watts |
| Groove geometry | |
| 30° included angle | |
| Groove width | 0.038 cm (0.015 in.) |
| Groove fillet | 0.013 cm (0.005 in.) |
| Groove depth in heat pipe wall | 0.376 cm (0.0148 in.) |
| Tungsten emissivity @ 1900°K | 0.24 |
| Effective emissivity of tungsten walls grooved with above dimensions | 0.55 |

tungsten emitter stem, which is a portion of the thermionic converter (see Section 4.1.5) is joined to the emitter heat pipe by an electron-beam weld.

4.1.5. Thermionic Converters

The thermionic converter is illustrated in Fig. 4.7, and the dimensions and operating parameters are given in Table 4.3. The thermionic emitter is formed by vapor deposition of a layer of tungsten with preferred crystal

TABLE 4.3
CONVERTER PARAMETERS

| | |
|--|-------|
| Emitter Diameter, cm | 0.98 |
| Emitter Length, cm | 5.0 |
| Emitter Wall Thickness, cm | 0.127 |
| Interelectrode Spacing, cm | 0.02 |
| Collector Thickness, cm | 0.127 |
| Collector Heat Pipe Wall Thickness, cm | 0.064 |
| Emitter Temperature, °K | 1900 |

orientation $\{110\}$ on the end of the emitter heat pipe. It is connected to a tungsten emitter stem which serves as a heat choke and an electrical connector from the emitter. The emitter stem is diffusion bonded to a heavy tantalum transition piece to which the positive electrical lead is connected. The transition piece is welded onto the upper niobium skirt of the insulator seal. The lower skirt of the seal is welded to the top of the niobium collector. The series electrical lead is integral with the collector. It is connected to the emitter lead of the next converter in series as described in Section 4.1.8.

Heat is removed from the collector by the annular collector heat pipe. This heat pipe transfers heat from the collector to the long radiator heat pipe, whose end is brazed in the socket below the converter. Cesium pressure in the converter is maintained by the graphite sorption reservoir in the recess in the insulator below the emitter.

4.1.6. Space Radiator

The heat rejected from each collector is radiated to space from a heat pipe which is brazed into a socket in the collector heat pipe. The radiator heat pipes are assembled to form a cone-shaped radiator. These pipes are mounted on, but electrically insulated from, a set of rings as shown in Fig. 4.1. Parameters describing these radiator heat pipes are listed in Table 4.4.

TABLE 4.4
PARAMETERS FOR SPACE RADIATOR

| | |
|--|-----------|
| Number of pipes | 69 |
| Heat load per pipe (Beginning of life) | 555 watts |
| Operating temperature | 1000°K |
| Heat pipe fluid | Potassium |
| Pipe o.d. | 1.15 cm |
| Pipe i.d. | 1.04 cm |
| Porous tube o.d. | 1.00 cm |
| Porous tube i.d. | 0.97 cm |
| Heat Transfer capacity at 1000°K (Ref. 8) | 940 watts |
| Overall length | 141 cm |
| Heated length | 3.75 cm |
| Required radiator length | 111 cm |
| Clearance between pipes at diameter of end of shield (33.8 cm) | 0.388 cm |
| Total mass of 69 pipes | 8.3 kg |

4.1.7. Neutron Shield

The neutron shield is included in the flight configuration to protect sensitive electronic equipment from radiation damage. It is fabricated of beryllium metal by powder metallurgy processes. Its shape is a conical frustrum with a cone angle of 2.9°, a height of 24 cm, and base diameters of 29.1 and 31.6 cm. The radiator heat pipes are angled to the periphery of the shield and then continue aft to the space radiator.

4.1.8. Electrical Connections

The 69 thermionic converters are arranged in a series-parallel network with 23 in series and 3 in parallel as shown in Fig. 4.8. The electrical network allows a buildup in the voltage to a terminal output of 15 volts by connection of 23 cells in series. The parallel cross connections in the network minimize the effects of the failure of an individual thermionic converter.

Should the cesium vapor leak out of an individual thermionic converter or an emitter heat pipe fail, the converter will no longer be able to conduct high currents. In the event of this "open-circuit" failure, current in the network is carried by those converters in parallel with the open-circuit converter. The parallel cells will continue to generate power although there will be some loss of output due to the higher current density. A number of analytical studies (Refs. 9-11) have demonstrated the effectiveness of this series-parallel network connection scheme in maintaining high electrical output and high voltage output in spite of cell failures.

The series electrical connection is via the emitter stem and the lead which is integral with the collector of the thermionic converter. These are illustrated in Fig. 4.8. The electrical connection is initially a mechanical one, with a diffusion bond formed at the operating temperature of the joint. The tantalum emitter lead of one converter is attached to the niobium collector lead of the next converter by molybdenum screws. When the thermionic converters are heated to their normal operating conditions, differential expansion between the molybdenum screw and the tantalum and niobium lead materials tightens the joint. Diffusion bonding of the leads is activated by a thin foil of nickel placed between the tantalum and niobium surfaces. This method of bonding is similar to that which has been used successfully in the testing of a four-cell cluster of electrically heated converters connected in a series-parallel network (Ref. 12). Parallel cross connectors of niobium are attached over the emitter leads by the same process.

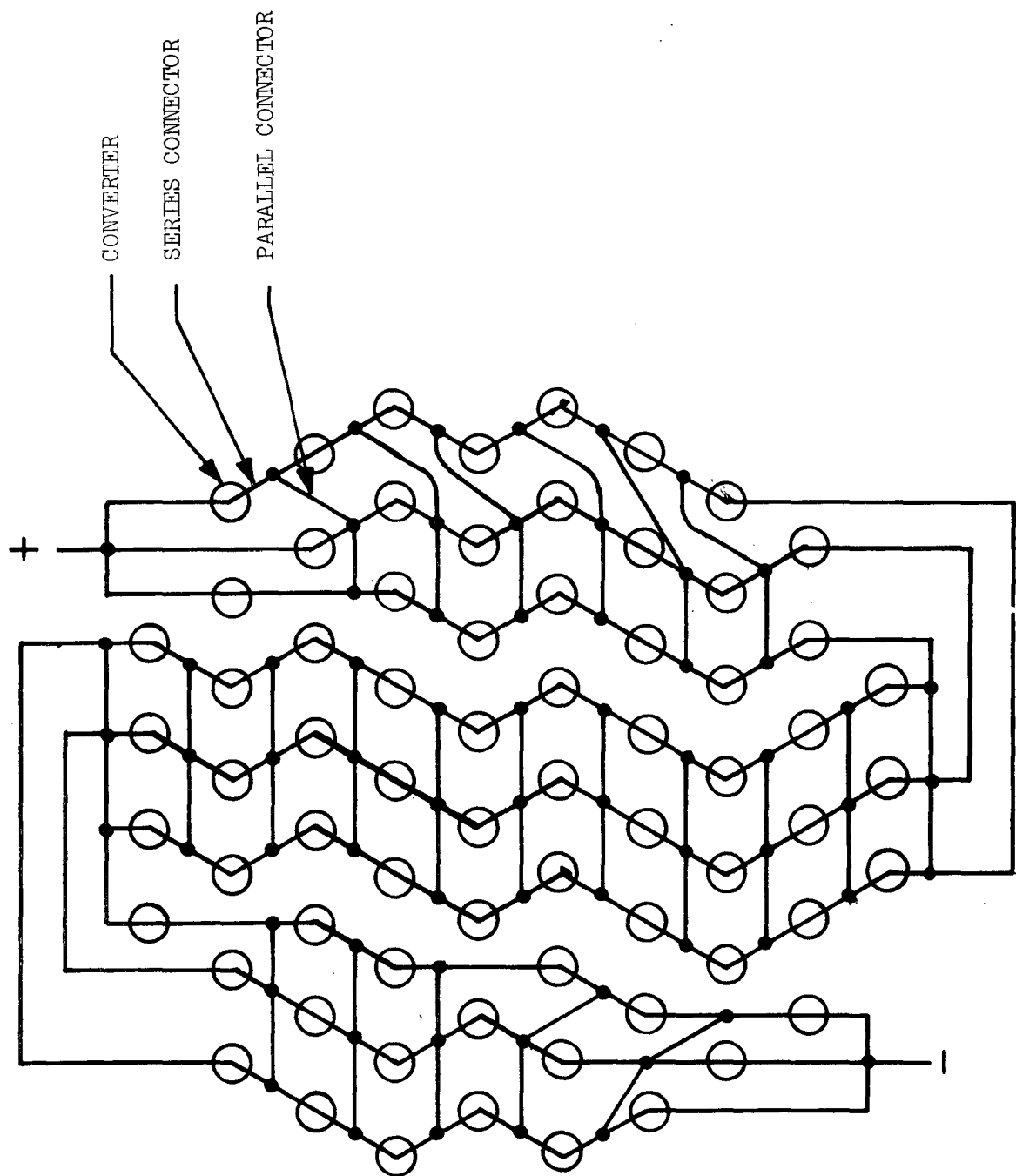


Fig. 4.8. Electrical Network

4.1.9. Transmission Lines and Boom

The electrical transmission lines carry current between the electrical network of thermionic converters and the power conditioning equipment which is located adjacent to the payload. The transmission lines are flexible multi-strand aluminum wire. The lines are sized to radiate the ohmic heating of 200 W (100 W per line) to space at an average temperature of 373°K. The transmission lines are on the outside of the neutron shield and radiator heat pipes and are insulated from these high temperature components. They pass through ceramic-to-metal seals in the base plate of the power source. The sections of the transmission lines between the base plate and the power conditioning equipment are coiled between these two components in the launch configuration, and are extended when the boom is extended.

The retractable boom which separates the power source from the power conditioning equipment and payload is a preformed foil which is rolled on a drum in the launch configuration. When extended it forms a hollow tube 1.27 cm in diameter by 0.025 cm wall thickness. It is 7.4 m long and provides a total separation distance between the heat source and the power conditioning equipment of 8.6 m.

4.1.10. Power Conditioning

Power conditioning requirements were analyzed to provide an estimate of the mass and efficiency of the system. A modular design approach was used in which an independent power processing module handled the power requirements of each thruster.

The system selected consists of 8 modules and thruster units, 7 operating and one standby at the start of the mission and 3 standby, or failed, and 5 operating at the end of the mission. The main power conditioning circuit in each module is the beam power supply which processes about 800 watts to 1500 volts. The analysis evaluated the beam power supply, and it is assumed that the resulting mass and efficiency is typical of the entire power processing requirement.

Two inverter circuits were evaluated, both using silicon power transistors. A design using a "push-pull" circuit with a single primary transformer

resulted in slightly lower mass but also a lower efficiency. The basic circuit chosen for the reference design (Fig. 4.9) uses a center tap transformer requiring two primary windings which allows passing the input current through a single switching branch minimizing the transistor losses.

Time ratio control (pulse width modulation) is assumed for source voltage control over a small range to handle BOL to EOL variation or changes in the thermionic performance.

A summary of power conditioning parameters is given in Table 4.5. The mass includes all components, wires, heat sinks and radiating panel, and base drive circuitry.

TABLE 4.5
POWER CONDITIONING PARAMETERS

| | |
|---|---------------------------|
| Transistor | Westinghouse 1441-0410 Si |
| Transistor case temperature | 100°C |
| Transistor power dissipation derating factor* | ~ 20 |
| Inverter frequency | 12 kHz |
| Inverter loss | 60 watts |
| Transformer loss | 17 watts |
| Module Efficiency | 89% |
| Module mass | 3.3 kg |
| Specific mass | 4.1 kg/kW |

*. Factor of reduction below maximum rated power dissipation.

4.2. SAFETY EQUIPMENT

The safety equipment is illustrated in Fig. 4.1. It provides for auxiliary cooling of the radioisotope heat source before and during launch and following a possible launch abort. The safety equipment also provides secondary containment for the radioisotope fuel and seals the heat source and converter assembly in a protective helium gas environment. Another important function of the safety equipment is to provide neutron shielding to reduce radiation levels around the radioisotope power source thereby

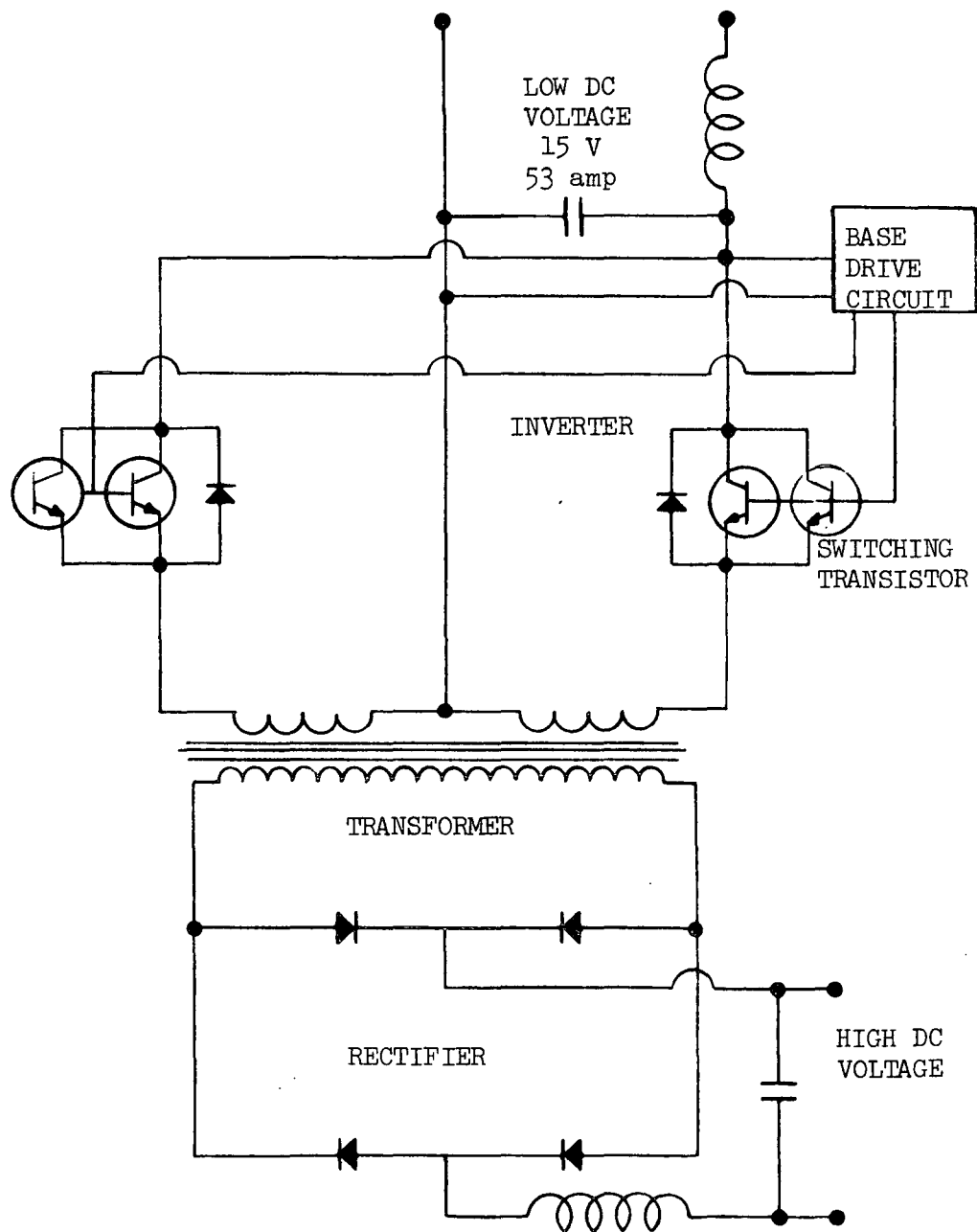


Fig. 4.9. Basic power conditioning module circuit

reducing hazards to people in the event of impact on land after a launch abort. A large portion of the safety equipment is designed to protect the secondary containment, auxiliary cooling system, and neutron radiation shielding from damage due to possible launch abort conditions. A blast shield and a fire shield protect against an explosion or fire on the launch pad. An aerodynamic flare stabilizes the orientation in the event of reentry and Pyrocarb ablative material protects exposed surfaces from reentry heating. Crushable honeycomb is included to absorb the energy of impact on land.

4.2.1. Auxiliary Cooling System

The auxiliary cooling system consists of 408 auxiliary heat pipes and a circulating helium system. The heated ends of the auxiliary heat pipes are inserted between the radioisotope capsules in the heat source as illustrated in Fig. 4.4. Heat is transferred from the capsule to the heat pipes by a combination of radiation and conduction through the helium gas.

The parameters of the potassium-filled auxiliary heat pipes are given in Table 4.6. As shown here, they contain a noncondensable gas which tends to accumulate in the cooled end of the heat pipe and varies the length of the heat pipe with temperature and power. The noncondensable gas smooths thermal transients during startup of the heat pipe and during the transition between heat rejection to the circulating helium coolant and heat rejection to space or the surroundings via the auxiliary radiator.

During prelaunch operations, helium is circulated through the chamber above the heat source with a flow rate of $4.32(10)^5 \text{ cm}^3/\text{sec}$ ($284 \text{ lb}_m/\text{hr}$) and a temperature rise of 278°K (500°F). At the time of launch, the helium inlet and outlet pipes are disconnected.

4.2.2. Neutron Shielding

The neutron shielding which is a part of the safety equipment is in two sections. A cylindrical shell of lithium hydride surrounds the sides

TABLE 4.6

AUXILIARY HEAT PIPE PARAMETERS

| | |
|--|----------|
| No. of pipes | 414 |
| Tube wall material | SS 316 |
| o.d. tube | 0.73 cm |
| i.d. tube wall | 0.71 cm |
| o.d. porous tube | 0.63 cm |
| i.d. porous tube | 0.60 cm |
| Heated radiator length at 900°K | 103.5 cm |
| Length of noncondensable gas at 900°K | 39.5 cm |
| Operating temperature with cooling by helium | 760°K |
| Total mass of 408 pipes | 32.5 kg |

of the heat source and a curved disc of lithium hydride covers one end of the heat source. The other end is covered by the beryllium neutron shield which is a part of the converter assembly. The sections of lithium hydride shielding are configured and arranged to provide a minimum of 10 cm of lithium hydride or equivalent.

Data in Ref. 13 indicates that 10 cm of lithium hydride can reduce the fast neutron dose by a factor of about 3.5. The 10 cm thickness of lithium hydride around the source reduces the dose at 1 m from the center of the source to 15.5 rem/hour.

In the abort mode, the lithium hydride will reach a maximum temperature of 1200°K. At this temperature the vaporization and dissociation pressure of hydrogen is 1.5 atmospheres. The LiH containment tank is designed to withstand this internal pressure at 1200°K, and the stainless steel is compatible with hydrogen and LiH, thus, no loss of LiH is expected.

4.2.3. Secondary Containment Vessel

The secondary containment vessel is made up of the heated ends of the auxiliary heat pipes, the tube sheet across the top of the heat source into which the heat pipes are brazed, the inside wall of the lithium hydride container, the conical structure around the flight radiator, and the base plate of the converter assembly (which is part of the flight configuration). This base plate is sealed to the remainder of the secondary containment vessel (which is part of the safety equipment) by a peripheral seal. This joint is separated during jettison of the safety equipment by a retraction of the three separation pins.

The portion of the secondary containment vessel which is part of the safety equipment is backed up by an outer vessel. This vessel is penetrated by the helium lines which have self sealing, quick disconnect fittings. Because of these penetrations, the outer vessel does not qualify as a containment vessel. It does provide a significant safety margin, however, on secondary containment of the radioisotope.

4.2.4. Reentry Shield and Aerodynamic Flare

The hemispherical nose, the cylindrical section, and the aerodynamic flare are protected from aerodynamic heating by a layer of Zirconia felt insulation covered by Pyro-carb 406. The thickness of these layers varies depending on location. The heating rates and protection system thickness are described in Sections 5.3 and 6.3.

The aerodynamic flare reduces the ballistic coefficient of the power supply and safety equipment thereby reducing aerodynamic heating rates and temperatures during reentry (See Sections 5.3 and 6.3.) and reducing the velocity on impact. The aerodynamic flare also causes the center of pressure of the reentering power source to be far aft of its center of mass. This causes the power source to align its axis with the air flow direction at high altitudes before aerodynamic heating rates become significant. The oriented reentry prevents severe heating of the cylindrical side walls.

4.2.5. Impact Energy Absorber

Energy absorbing material is provided to protect the system from damage in the event of impact upon land after a failure in the launch sequence. The energy absorbing material in the nose region of the safety package is 73.4 cm of crushable aluminum honeycomb. Characteristics of this material are discussed in Section 6.4.1. The honeycomb is designed to absorb the energy of impact at a terminal velocity of 45 m/sec (147 ft/sec) with a maximum rate of deceleration of 200 g's. The structural components in the system have been designed to withstand this deceleration rate with no damage being inflicted on the auxiliary cooling system.

4.2.6. Structural Components and Blast Shield

The structural components of the radioisotope electric propulsion system have been designed to withstand shock and vibration environment of the launch by the Titan 3D/Centaur combination and for possible impact upon land after a launch abort. The configuration of the structural components is shown in Fig. 4.1.

The structural material of the components has been selected as SS-316 which results in a total structural weight of 128 kg (283 lb). It would be possible to reduce this weight by a factor of 2 with the selective use of beryllium, titanium, and aluminum; however, since this structure is associated with the jettisonable safety package, a weight penalty has been accepted to gain simplicity of fabrication. A summary of the key components of the structure, their nominal thicknesses and approximate weights is given in Table 4.7.

TABLE 4.7
STRUCTURAL COMPONENTS
(All material - SS 316)

| Component | Thickness | Mass |
|--|-----------------------|---------------------|
| Outer Shell | 0.152 cm (0.06 in.) | 30.7 kg (67.6 lb) |
| Upper support cone | 0.3175 cm (0.125 in.) | 3.6 kg (8 lb) |
| Lower support cone | 0.223 cm (0.08 in.) | 12.3 kg (27 lb) |
| Insulated rings | 0.127 cm (0.05 in.) | 1.6 kg (3.5 lb) |
| Heat pipe support rings | 0.127 cm (0.05 in.) | 2.7 kg (6 lb) |
| Keyed rings | 0.3175 cm (0.125 in.) | 8.6 kg (19 lb) |
| Latches | | 2.7 kg (6 lb) |
| Trusses between shield and heat source | 0.254 cm (0.1 in.) | 2.3 kg (5 lb) |
| Fixtures at payload interface | 0.254 cm (0.1 in.) | 1.1 kg (2.5 lb) |
| LiH containment tanks | 0.152 cm (0.06 in.) | 56.4 kg (124 lb) |
| Hardware and bonding material | | 6.4 kg (14 lb) |
| | TOTAL | 128.4 kg (282.6 lb) |

The base of both the flight system and the safety package are protected by a blast shield from shrapnel and overpressure during a booster explosion. The blast shield thickness determination is discussed in Section 6.2.

4.2.7. Launch Pad Fire Protection System

A solid propellant launch pad fire protection shield is located around the auxiliary radiator heat pipes, as shown in Fig. 4.1. The shield consists of an outer layer of zirconia felt 0.31 cm (0.120inch) thick and an inner layer of lithium hydride 1.9 cm (0.75-inch) thick (Section 6.1.2.). It is designed to limit the maximum temperature of the radiator heat pipes to 1200°K (1700°F) when exposed to 2600°K (4250°F) fire for ten minutes, and when lying on the surface of the earth and transferring the 44.2 Kw (th) of internal heat to the atmosphere. The zirconia is surrounded by a Pryocarb layer for reentry protection which does not significantly influence the launch pad fire protection.

The purpose of the Zirconia insulation is to lower the heat input to the LiH heat storage material outside the heat pipes. Thicknesses of each material were selected considering both optimum mass and temperature drop. The allowable temperature drop across the shield is 300°K, which represents the difference between the equilibrium surface temperature of the radiator in air (900°K) and the allowable temperature of the heat pipes (1200°K). The overall mass of the ZrO_2 /LiH fire shield and stainless steel structure is 67.5 kg. In comparison, a launch escape system to remove the RTPS from the fire would have a mass of 290 kg, lower reliability and greater design impact on the launch vehicle.

4.3. OPERATING SEQUENCE

The procedures for assembly and disassembly of the radioisotope thermionic power supply and the sequence of operations during a normal launch and possible launch aborts are described in the following sections. All of the operations described are performed on the launch configuration power supply shown in Fig. 4.1, or on portions of this power supply.

4.3.1. Final Assembly of the Launch Configuration

The loading of the isotope capsules and the final assembly of the generator in the launch configuration is performed in a helium-filled glove

box environment. The safety equipment is placed in the glove box with the axis horizontal. Helium lines are attached at the quick disconnect couplings and cooled helium is circulated through the chamber in the safety equipment. The radioisotope capsules and all other parts of the power supply are placed in the glove box.

The inner grid plate (See Fig. 4.4) is inserted into the safety equipment and aligned with the pins on the ends of several of the auxiliary heat pipes. After all of the capsules have been loaded, the outer grid plate with the attached insulated shroud and insulated door is placed over the capsules and attached to the inner grid plate. The converter assembly is then inserted in the safety equipment to within 1 cm of full insertion. At this point, the rods from the heat source support structure are attached to the base plate of the converter assembly. This temporarily withdraws the heat source from the auxiliary cooling system by 1 cm. When the rods have been connected, the converter assembly with the heat source is inserted fully in the safety equipment and the separation pins are inserted to close the peripheral seal. The seal is checked for leak-tightness prior to opening the glove box to remove the assembled generator. All of these operations are performed semi-remotely from behind water or polyethylene shielding using long handled tools.

4.3.2. Assembly and Disassembly for Testing

The generator is assembled in the launch configuration in the same manner as described in Section 4.3.1. It is sealed with helium inside during transfer from the fueling facility to the test chamber. The test chamber is evacuated prior to opening the sealed launch configuration. The base seal is opened remotely, releasing the helium gas contained inside. The flight configuration is then removed from the safety equipment. After it is completely removed, the heat source door is released and swings shut. At this point, temperatures rise to the operating conditions and the test begins.

At the conclusion of the test, the vacuum chamber is back-filled with purified helium gas. The heat source door is removed by pulling out the hinge pin. The radioisotope power source is then inserted into the safety

equipment to within 1 cm of full insertion. The rods attaching the heat source to the base plate of the converter assembly are disconnected and attached to the safety equipment. The converter assembly is then inserted fully into the safety equipment and the separation pins are engaged. The assembled generator is leak checked prior to removal from the vacuum chamber for transportation to the fueling and defueling facility.

The defueling operation is performed by reversing the procedures followed in final assembly. The converter assembly is first removed from the safety equipment and heat source. The outer grid plate and shroud are then removed from the heat source, and the isotope capsules are removed one by one.

4.3.3. Launch and Flight

The power source is assembled in the launch configuration as described in Section 4.3.1 after being pretested as described in Section 4.3.2. In transportation to the launch site, the power source is mounted in a shipping container which incorporates neutron shielding and a helium circulation and cooling system. It is mated to the payload and the Centaur with auxiliary shielding maintained in place around the power source. Shortly before launching, after the site has been cleared of personnel, the auxiliary shielding is removed. The helium lines are disconnected remotely a few seconds prior to launch.

Following burnout of the Centaur, the attainment of a hyperbolic trajectory is verified from tracking data. The mechanism for separation of the safety equipment is armed and actuated by ground command. After successful jettison of the safety equipment is verified, the heat source door is released and swung shut by the spring and the boom is deployed. The payload and propulsion system are separated from the Centaur and the electric thrusters are started up.

4.4 SYSTEM MASS AND POWER SUMMARY

Figure 4.10 illustrates the overall dimensions of the launch system and the major components of the radioisotope thermionic power supply at the reference design power level.

A summary of the masses of the major components of the system is given in Table 4.8. From this table it is seen that the total mass at launch is 723.8 kg while the mass of the extended mission flight system is 148.5 kg. The estimated uncertainty in the safety system mass of 90 kg is primarily due to difference between the final system mass and that used for the aerodynamic heating analysis. This mass difference will result in a higher ballistic coefficient and an increase in aerodynamic heating, unless the flare diameter is also increased (Section 6.3.1.2). An increase in flare diameter between 244 cm and 305 cm would compensate for this difference with an attendant increase in structure and graphite mass of up to 90 kg. Since the safety system is ejected early in the heliocentric phase of the mission, this mass uncertainty should not have a significant effect on payload mass.

A summary of the electrical power output from the system at beginning-of-life (BOL) and end-of-life (EOL), after 36,000 hours, is shown in Table 4.9.

TABLE 4.9
ELECTRICAL PERFORMANCE PARAMETERS

| | <u>BOL</u> | <u>EOL</u> |
|--------------------------------|------------|------------|
| Number of operating converters | 69 | 59 |
| Net output (kWe) | 5.93 | 5.0 |
| Overall efficiency (%) | 13.4 | 13.2 |
| Total thermal power (kWt) | 44.2 | 37.77 |
| Voltage to P.C. (volts) | 15.2 | 14.9 |

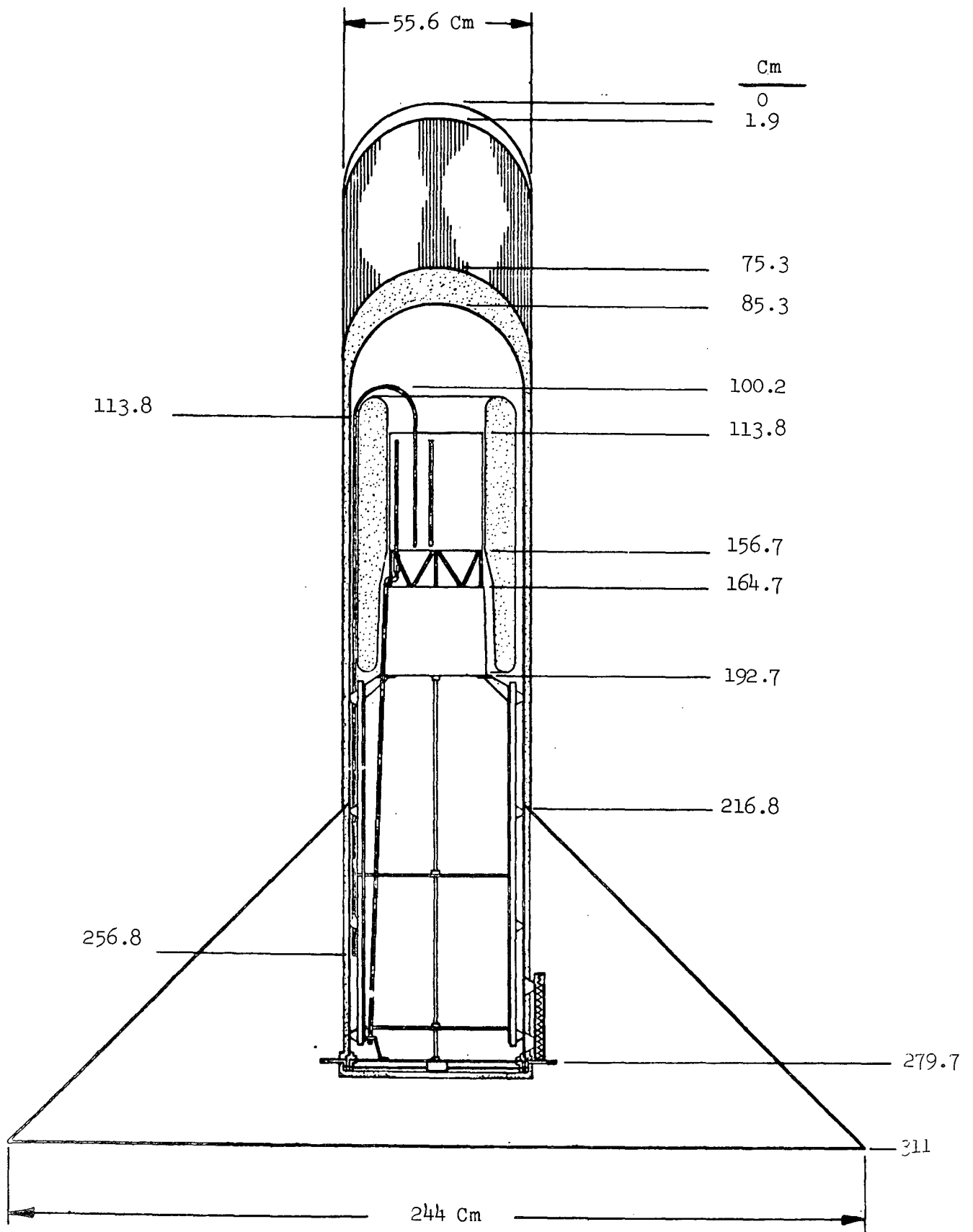


Fig. 4.10. Overall dimensions of launch configuration

TABLE 4.8
SYSTEM COMPONENT MASSES

A. Extended Mission System

| | |
|--------------------------------------|---------------|
| Curium isotope capsules | 29.2 kg |
| Emitter heat pipes | 9.0 kg |
| Thermionic diode components | 6.4 kg |
| Space radiator heat pipes | 6.3 kg |
| Structure for space radiator | 3.2 kg |
| Beryllium shield | 24.1 kg |
| Heat source structure and insulation | 15.5 kg |
| Transmission lines and boom | 18.9 kg |
| Power conditioning | 30.0 kg |
| Blast shield | <u>5.9 kg</u> |
| Flight System Total | 148.5 kg |

B. Disposable Safety System

| | |
|----------------------------------|---------------------|
| Graphite and insulation on nose | 11.3 kg |
| Graphite on cylindrical body | 17.0 kg |
| Graphite and insulation on flare | 123.7 kg |
| Aluminum honeycomb | 25.1 kg |
| Zirconia/LiH fire shield | 67.5 kg |
| Aerodynamic flare structure | 35.7 kg |
| LiH shielding | 78.6 kg |
| Auxiliary heat pipes | 32.5 kg |
| Launch and impact structure | 128.4 kg |
| Jettison mechanisms (EST) | 12.8 kg |
| Helium baffle | 2.3 kg |
| Titanium blast shield | 25.8 kg |
| Electronic recovery aids | <u>14.6 kg</u> |
| Safety System Total* | <u>575.3 kg</u> |
| TOTAL LAUNCH MASS | <u>723.8 kg</u> |

*Mass of the safety system is uncertain by approximately 90 kg due to design tolerances in the aerodynamic flare diameter and graphite thickness (Vol. II, Sections 4.4 and 6.3.3.2.).

5. AEROSPACE NUCLEAR SAFETY

5.1. SAFETY CRITERIA

The aerospace nuclear safety philosophy currently employed by the USAEC is complete containment of the radioisotope fuel during all normal and accident environments. Specifically, the major safety criteria considered in this study were:

- Containment during a launch pad abort of a Titan IIID/Centaur vehicle, including survival during a 10-minute 2600°K solid propellant fire environment
- Safety System protection during an ascent abort and resulting explosion shrapnel
- Fuel and Safety System protection for worst-case atmospheric reentry trajectories
- Fuel structural and thermal protection during terminal velocity impact onto land
- Radiation shielding to minimize exposure of operating personnel and persons in the vicinity of an aborted system.

All of these design criteria were met using passive and redundant components, which are listed in Table 5.1.

As noted in Ref. 1, these criteria were established considering that the mission profile calls for direct insertion of the radioisotope power supply into a heliocentric orbit with no requirement for reentry and retrieval, except in the case of launch aborts. No suitable guidelines could be found concerning acceptable radiation exposure to persons in the vicinity of an impact on land. However, it has been estimated that recovery could be

TABLE 5.1

RIPS SAFETY PACKAGE SUBSYSTEMS

-
1. Passive orientated reentry aeroshell with spherical nose and aerodynamic flare
 2. Pyro-Carb ablator with zirconia felt insulation backing for reentry protection
 3. Auxiliary heat pipe radiator and LiH neutron shield
 4. Auxiliary radiator solid propellant fire protection shield
 5. Honeycomb terminal velocity impact energy absorber
 6. Launch pad helium circulation cooling chamber
 7. Blast shield for fragment protection
 8. Location aids for land and water impact
-

accomplished in 12 hours, as discussed in Section 5.6, which would reduce the maximum exposure to persons within 3 meters to less than 25 rem - the maximum whole body dose for reactor siting studies.

5.2. LAUNCH PAD EXPLOSION AND FIRE

Launch abort environments for the RTPS were modeled after those presently employed for Space Nuclear Systems, such as the TRANSIT and Pioneer RTG's and the Isotope Brayton System (Refs. 14-16). Tables 5.2 and 5.3 present typical composite launch phase abort environments for the TRANSIT and MHW (Multi-Hundred Watt) RTGs. These two models are relatively consistent for peak static overpressures resulting from explosion of the upper stage and for shrapnel velocities. However, fragment sizes vary considerably primarily due to the much smaller sized payload and upper stage for TRANSIT. The solid propellant fire environment is also comparable for the two models, although the 10 minute duration for the Titan IIIC is believed to be more representative of a Titan IIID vehicle. A specific abort accident environment for the Titan IIID vehicle, or for the Viking Mission, presently does not exist.

5.2.1. Launch Pad Thermal Environment

Thermal environments for a Titan III launch pad fire are summarized in Table 5.4. Heat input from the liquid propellants was determined by numerically integrating the curve in Fig. 5.1, which assumes the Sandia accident model and the Titan III propellant mass. Two solid propellant fire models are given, and apply for the safety system falling close to or in contact with segments of burning propellants. These models are based on recent nuclear systems accident studies.

Heat input values in Table 5.4 assume a view factor of 0.9 for radiant heat input to the active radiator surface. To illustrate the magnitude of the fire heat input, these values are ratioed by the heat source power generation over the predicted fire duration.

TABLE 5.2

SAFETY DESIGN STANDARDS FOR THE TRANSIT HEAT SOURCE

Launch

| Applicable Safety Criteria | Potential Environment | | | Design Requirement |
|---|------------------------------------|---------------------------------------|---|---|
| | Type | Parameter | Extent | |
| 5. The heat source shall contain the fuel during launch phase aborts of the Scout vehicle and for 1 week thereafter so that recovery can be effected. | A. Overpressure | (1) Peak static pressure | 950 psi | Maximum capsule dynamic stress shall not exceed the yield stress. |
| | | (2) Initial heat source temperature | Equilibrium, in air under shroud, without cooling | |
| | | (3) Configuration | Heat source in converter | |
| | B. Shrapnel | (1) Velocity | In the range 200 to 1500 ft/sec | Maximum penetration depth shall not exceed 80% of primary containment member thickness. |
| | | (2) Material | Aluminum or titanium | |
| | | (3) Size | Up to 3.5 pounds | |
| | | (4) Configuration | Heat source in converter | |
| | C. Heat source in launch site area | (1) Medium | Granite | Impact Velocity shall not exceed 326 ft/sec. |
| | | (2) Drop height | 1100 ft | |
| | | (3) Configuration | Heat source, or heat source in converter | |
| | | (4) Temperature | Equilibrium in air under shroud | |
| | | (5) Angle | Any | |
| | D. Fire (burning propellant) | (1) Flame temperature | Maximum of 4500°F ($\epsilon_a = 0.2$) | Maximum strength member corrosion shall not exceed 80% of total thickness. |
| | | (2) Duration | Approximately 5 minutes | |
| | | (3) Effective distance to heat source | 0 ft | |
| | | (4) Configuration | Heat source, capsule | |
| | E. Thermal | (1) Temperature | Equilibrium in air | Maximum liner temperature shall not exceed 2000°F. |
| | | (2) Duration | >1 week | |
| | | (3) Configuration | Heat source, capsule on surface of earth | |

TABLE 5.2 (continued)
Ascent

| Applicable Safety Criteria | Potential Environment | | | Design Requirement |
|---|---|--|--|--|
| | Type | Parameter | Extent | |
| 6. Fuel Containment shall be assured during normal ascent of the Scout vehicle. There shall be no degradation in any component which will affect heat source integrity in subsequent operational and abort environments. Also, fuel containment shall be assured during ascent aborts, i.e., failure to achieve any orbit, and throughout the subsequent reentry and impact environments specified below. | A. Boost (normal) | (1) Vibration (2) Acceleration (3) Spin and despin (4) Depressurization | Qualification levels | Heat source resonant frequency shall be above or below the critical boost vibration frequencies. Heat source component tolerances shall be selected to avoid coating abrasion. |
| | B. Thermal | (1) Temperature (2) Duration (3) Configuration | Ascent history temperature 15 minutes Heat source in converter | Maximum liner temperature shall not exceed 2000°F. |
| | C. Abort overpressure | (1) Peak static pressure (2) Initial heat source temperature (3) Configuration | <950 psi Space operating temperature Heat source in converter | Maximum capsule dynamic stress shall not exceed the yield stress. |
| | D. Abort shrapnel | (1) Velocity (2) Material (3) Size (4) Configuration | Heat source in converter In the range of 200 to 1500 ft/sec Same as pad abort Same as pad abort Heat source in converter | Maximum penetration depth shall not exceed 80% of primary containment member thickness. |
| E. Firestream | (1) Stagnation temperature (2) Duration (3) Configuration | 5400°F <60 seconds Heat source, heat source in converter | Maximum clad temperature shall not exceed 3100°F. | |
| | F. Corrosion | (1) Reactants (2) Duration (3) Configuration | Combustion products solid propellant/air Several minutes Heat source, heat source in converter | Maximum corrosion depth shall not exceed 5% of heat shield thickness or 5% of strength member thickness. |
| G. Improper shroud separation | (1) Temperature (2) Duration (3) Configuration | Space equilibrium 10 minutes Heat source in converter, converter inside shroud | Maximum clad temperature shall not exceed 3100°F. | |

TABLE 5.3

SUMMARY OF COMPOSITE ABORT ENVIRONMENTS FOR THE MHW HEAT SOURCE

| <u>Situation Component</u> | <u>Dominant Mission or Vehicle</u> | <u>Environment Definition</u> | | | | | | | | | | | | | | | | | | | | | | | | |
|--|--|---|--------------|-------------|-------------|---------|---------|---------|----------|---------|---------|----------|----------|----------|--------------|-------------|-------------|---------|-----------|--------|----------|----------|----------|------|-----|-----|
| Ground Handling Fire Impact | All Missions | 1475 °F, $\epsilon = 0.9$, 30 min. 30 foot drop, unyielding surface | | | | | | | | | | | | | | | | | | | | | | | | |
| Launch Pad Accident Liquid Fire Fireball Liftoff Afterfire Solid Fire Temp. Duration Blast Overpressure Static Stagnation Reflected Impulse Duration Velocity Yield Fragments Sheet Size Velocity Components Weight Velocity Chemical Liquid Fire Atmosphere Duration Solid Fire Atmosphere Duration Impact-velocity | Saturn V Titan IIIC Saturn V Saturn V Saturn V Titan IIIC | 12 seconds 1 hour, 1875 °F, $\epsilon = 0.9$ 4250 °F 10 minutes <table> <tr> <td><u>S-IVB</u></td><td><u>S-II</u></td><td><u>S-IC</u></td></tr> <tr> <td>840 psi</td><td>280 psi</td><td>205 psi</td></tr> <tr> <td>2700 psi</td><td>780 psi</td><td>550 psi</td></tr> <tr> <td>6800 psi</td><td>1900 psi</td><td>1350 psi</td></tr> <tr> <td>8.2 psi-sec.</td><td>5.5 psi-sec</td><td>7.5 psi-sec</td></tr> <tr> <td>39 msec</td><td>19.5 msec</td><td>7 msec</td></tr> <tr> <td>7750 fps</td><td>4800 fps</td><td>4200 fps</td></tr> <tr> <td>20 %</td><td>20%</td><td>20%</td></tr> </table> 1 in ² to 210 ft ² 300 fps to 3500 fps 1 lb to 200 lb 100 fps to 300 fps H ₂ O, NH ₃ , CO ₂ , CO, NO, NO ₂ , HNO ₃ 1-hr. Al ₂ O ₃ , AlCl ₃ , Cl ₂ , CO, CO ₂ , H ₂ , HCl, H ₂ O, N ₂ , OH 10 min. 160 fps | <u>S-IVB</u> | <u>S-II</u> | <u>S-IC</u> | 840 psi | 280 psi | 205 psi | 2700 psi | 780 psi | 550 psi | 6800 psi | 1900 psi | 1350 psi | 8.2 psi-sec. | 5.5 psi-sec | 7.5 psi-sec | 39 msec | 19.5 msec | 7 msec | 7750 fps | 4800 fps | 4200 fps | 20 % | 20% | 20% |
| <u>S-IVB</u> | <u>S-II</u> | <u>S-IC</u> | | | | | | | | | | | | | | | | | | | | | | | | |
| 840 psi | 280 psi | 205 psi | | | | | | | | | | | | | | | | | | | | | | | | |
| 2700 psi | 780 psi | 550 psi | | | | | | | | | | | | | | | | | | | | | | | | |
| 6800 psi | 1900 psi | 1350 psi | | | | | | | | | | | | | | | | | | | | | | | | |
| 8.2 psi-sec. | 5.5 psi-sec | 7.5 psi-sec | | | | | | | | | | | | | | | | | | | | | | | | |
| 39 msec | 19.5 msec | 7 msec | | | | | | | | | | | | | | | | | | | | | | | | |
| 7750 fps | 4800 fps | 4200 fps | | | | | | | | | | | | | | | | | | | | | | | | |
| 20 % | 20% | 20% | | | | | | | | | | | | | | | | | | | | | | | | |
| Ascent-to-Orbit Aborts Firestream-duration Explosion Fragments | Saturn V | 25 sec. ≤ Pad accident ~ Pad accident | | | | | | | | | | | | | | | | | | | | | | | | |
| Post Abort Re-entry Ballistic Velocity Angle HS Configuration Orbit Decay Velocity Angle HS Configuration Elliptical Orbit Velocity Angle HS Configuration | All Missions Earth orbit Missions or those using parking orbit Lunar Mission | < 25,570 fps Variable Full heat source 25,570 fps 0° Full heat source ≤ 36,675 fps ~ 0 - 90° Full heat source | | | | | | | | | | | | | | | | | | | | | | | | |
| Earth Impact Velocity Surfaces HS Configuration | All Missions | 200 - 400 fps (depends on $\frac{W}{C_{DA}}$) water, soils, concrete, granite full heat source (ablated) | | | | | | | | | | | | | | | | | | | | | | | | |
| Post Impact Reactants Fire Burial | All Missions | soils, water (saline and fresh) 1475 °F, (hours) undergrowth, trees | | | | | | | | | | | | | | | | | | | | | | | | |

TABLE 5.4
RADIANT HEAT INPUT TO SAFETY SYSTEM FROM LAUNCH PAD FIRE

| SOURCE | TEMPERATURE | DURATION | HEAT INPUT TO SYSTEM | HEAT INPUT/ HEAT GENERATION |
|------------------------------------|--------------------------------|-------------|-----------------------------|--------------------------------|
| Liquid Propellants | 5000°F-4000°F (3000-2500°K) | 4.8 seconds | 2.3(10) ⁷ joules | 92 |
| Solid Propellants ⁽¹⁾ | 4250°F (2616°K) | 10 minutes | 2.3(10) ⁹ joules | 74 |
| Solid Propellant ⁽²⁾ | 3000°F (1922°K) | 30 minutes | 2.0(10) ⁹ joules | 21 |
| After Fire (Liquid Propellants) | 1850°F (1283°K) | 30 minutes | 4.0(10) ⁸ joules | 4.3 |

(1) Titan IIIC fire model presented by GE

(2) Solid fire temperature used by AVCO for Isotope Brayton

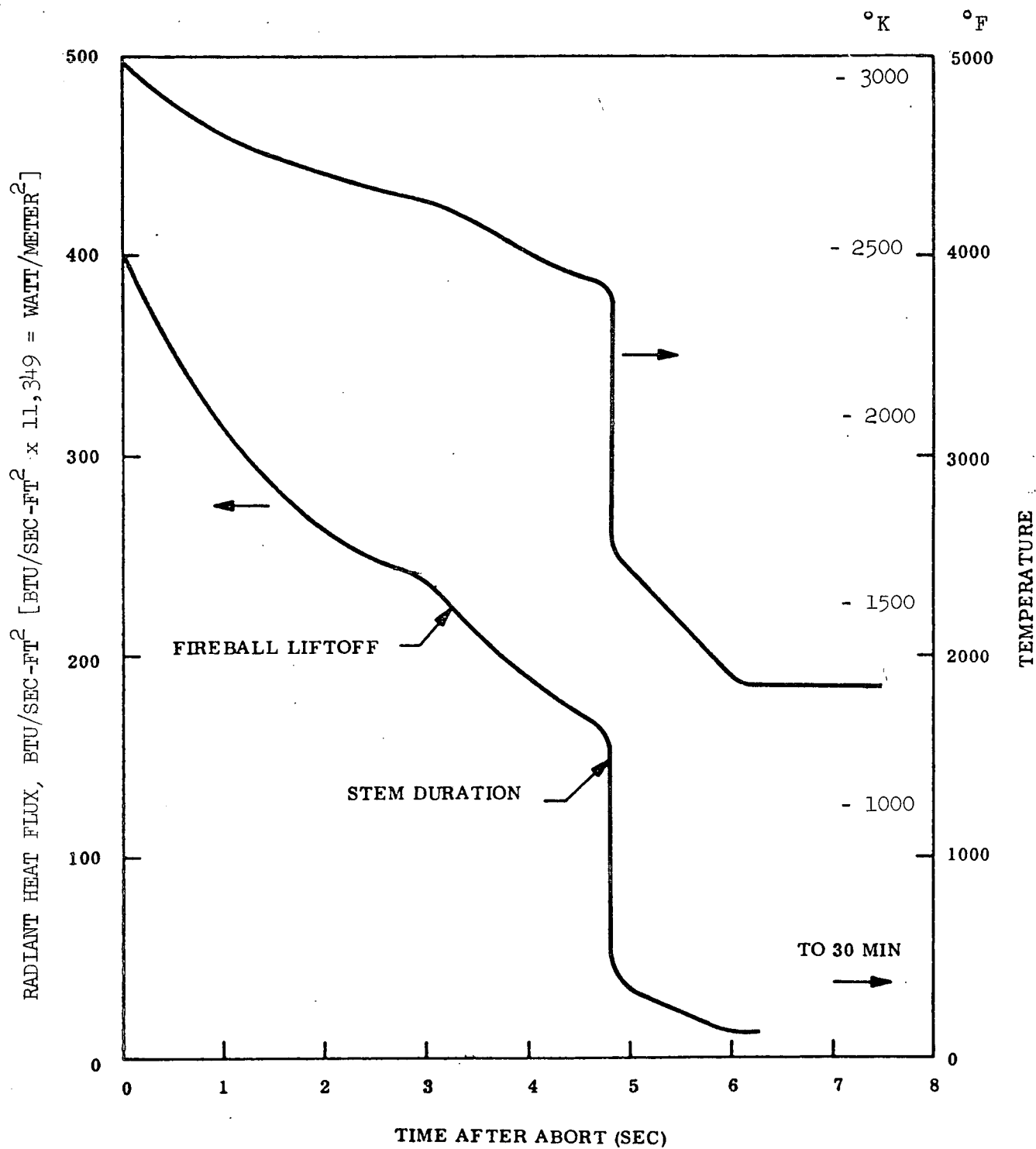


Fig. 5.1. Liquid propellant fireball radiant heat flux and temperature for a Titan III launch abort

For the present study the worst-case thermal environment, in terms of total heat input, was assumed for the heat shield design - 2600°K for 10 minutes. Concepts considered to protect the safety package in this environment included:

1. High C_p heat shield materials
2. Insulation blankets
3. Thermal switch materials
4. Concentric radiation shields
5. Composite insulation/heat storage shields.

The latter approach was the only method found acceptable from both a thermal protection and total mass standpoint. Each of these concepts will be discussed in Section 6.1.

5.2.2. Fragment Environment

Experimental fragment velocity distributions are shown in Figs. 5.2 and 5.3 which were extracted from Ref.17. The quantity of propellant for these cases is comparable to the Centaur Stage. Consequently, this data is believed to be applicable to predicting fragment velocities for the present study.

Table 5.5 shows the fragment environment postulated for the Pioneer Mission, which employs a Centaur upper stage. These components and velocities represent potential projectiles for design of a fragment shield.

Because of the great uncertainty in designing a fragment shield and the potentially astronomical mass penalty associated with one, the approach taken for the RTPS was to use existing shield technology based on empirical

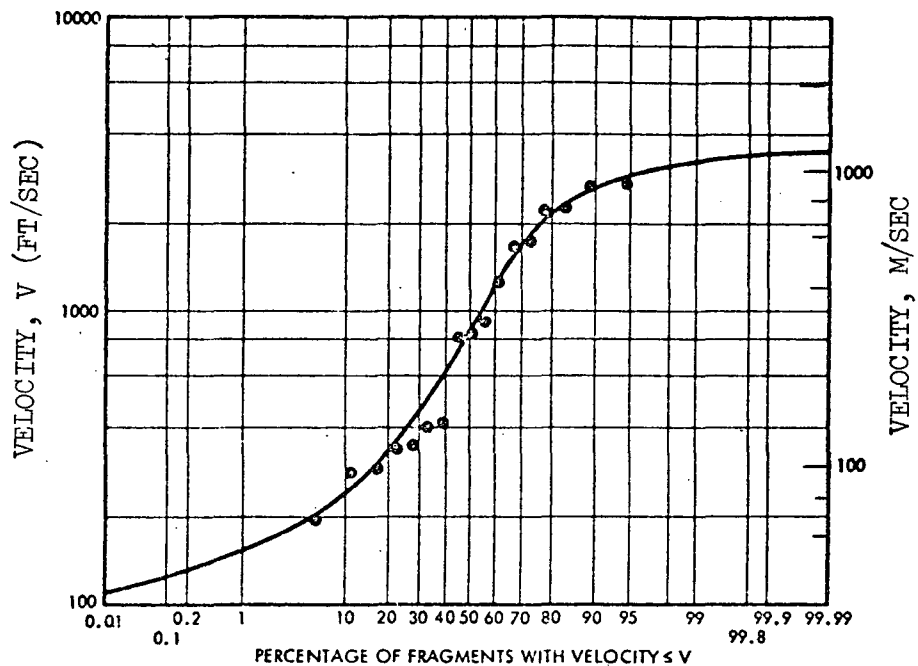


Fig. 5.2. Upward Fragment Velocities from 25,000-Pound Project PYRO Experiments (10 feet from top dome)

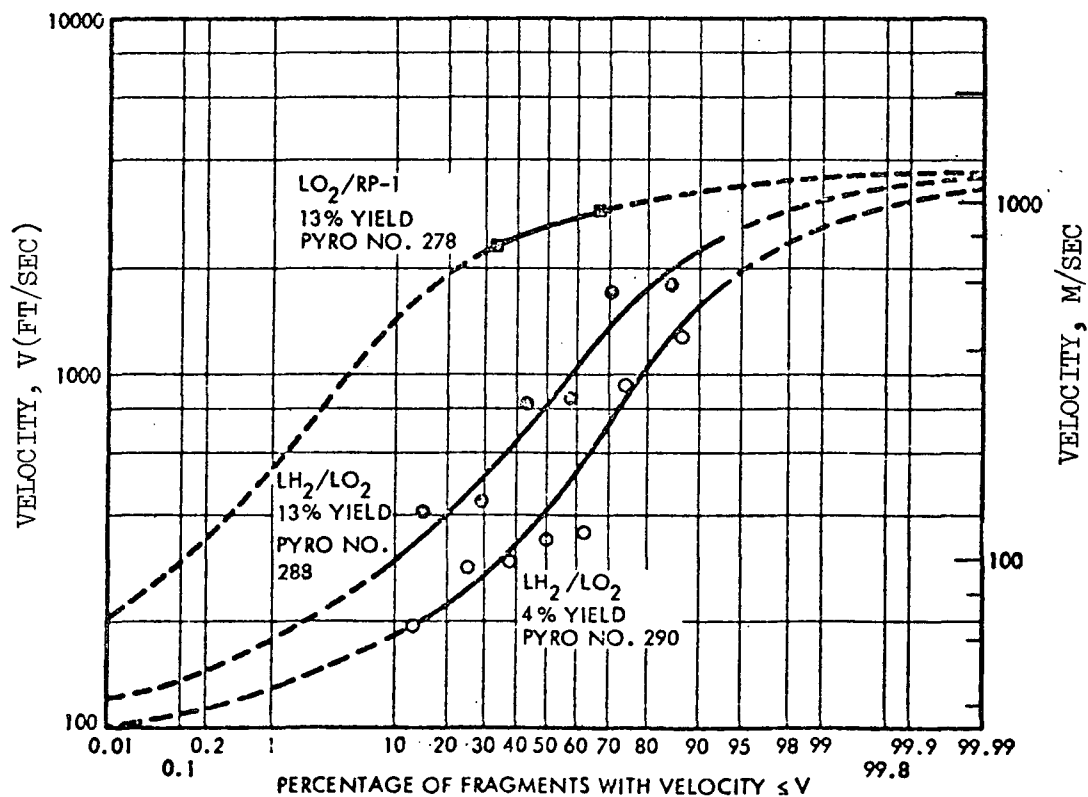


Fig. 5.3. Upward Fragment Velocities from 25,000-Pound Project PYRO Experiments (10 feet from top dome)

TABLE 5.5
FRAGMENT ENVIRONMENTS

| Explosive Source | Fragment Source | Material | Weight | Speed ⁽¹⁾ |
|------------------|------------------------|---------------------------|-----------------------------------|----------------------------------|
| TE 364-4 | Motor casing | Titanium | 1.2 lb ⁽²⁾ (.54 kg) | 1560 f/sec (edge) (475 m/sec) |
| | " | " | | 2550 f/sec (side) (770 m/sec) |
| Centaur | Centaur tank skin | Stainless Steel | 0.6 lb ⁽²⁾ (.27 kg) | 3600 f/sec 1100 m/sec |
| Centaur | Telemetry installation | Aluminum and magnesium | 38.5 lb (17.5 kg) | 410 f/sec (125 m/sec) |
| Centaur | Tank hemispheres | Stainless Steel | 2.1 lb (.95 kg) | 339 f/sec (103 m/sec) |

(1) Blockage and atmospheric drag not considered

(2) For fragment with one square foot area

results. Assuming that the RTPS is mounted with the flare base towards the launch vehicle, the 25 cm beryllium shield will provide adequate protection for the fuel capsules. The primary purpose of a blast shield is to protect the aerodynamic flare and auxiliary radiator from damage. Since the flare structure will adequately shield the radiator, due to its composite stainless steel/insulation/graphite construction, the main concern is excessive damage to the flare. Consequently, the approach taken has been to place a thin titanium fragment shield at the aft end of the system to attenuate high energy fragments and provide partial protection to the flare. Alternate blast shield concepts are discussed in Section 6.2.

5.2.3. Overpressures

The overpressure environment for the Titan IIID/Centaur was predicted using data presented in the TRANSIT Safety Analysis Report (Ref. 14). The method used requires the equivalent TNT yield and a computed reduced distance scaling parameter λ , where

$$\lambda = D/W^{1/3}(\text{ft}/\text{lb}^{1/3})$$

D = distance from the blast center

W = equivalent propellant yield.

Curves in the TRANSIT Safety Report give λ vs overpressure based on test data and TNT models developed by Brode, Kingery and Kinney (Ref. 14). For a worst-case condition, a maximum probable yield for the hypergolic propellants (Stages I and II) is on the order of 5%, while 20% can be taken as a maximum for the LOX/LH propellant in the Centaur Stage (Ref. 18). The expected peak static overpressures at the radioisotope heat source for the reference design are tabulated below.

| Stage | Distance from Explosion Center to Heat Source | | Propellant Weight (lb) | λ (ft/lb ^{1/3}) | (psi) | (n/m ²) |
|-----------|---|-----|------------------------------|--------------------------------------|-------|-----------------------|
| | (ft) | (m) | | | | |
| Stage I | 115 | 35 | 413,000 | 4.19 | 65 | 4.5(10) ⁵ |
| Stage III | 68 | 21 | 70,700 | 4.46 | 54 | 3.7(10) ⁵ |
| Centaur | 50 | 15 | 30,100 | 2.75 | 150 | 10.3(10) ⁵ |

These overpressures are believed to be extremely conservative because of the high yields assumed and neglect of intermediate mass attenuation. Experimental overpressure from aborts of the Saturn S-IVB and Atlas/Centaur at 15 meters were 50 psi and 20 psi respectively.

The overpressure environment for the Pioneer mission was 530 psi with a peak pressure impulse of 1060 psi-ms. These values were based on the Centaur vehicle and a separation distance of 38.5 m and thus scaled to somewhat higher pressures than those above.

The fire shield and outer structure is designed to withstand these predicted launch pad overpressures. Lower pressures will be experienced during a high altitude abort, although no estimate has been made of the expected magnitude. However, it is expected that the fragment environment effects will be considerably more severe than overpressure effects.

5.3. REENTRY AND AEROTHERMODYNAMICS

5.3.1. Abort Environments

Reentry of the radioisotope thermionic power system (RTPS) occurs only in the event of failure of the launch vehicle to place the payload in an escape trajectory. Thus, all possible abort conditions had to be considered. The most likely abort cases cause the RTPS to reenter as a free body.

The most severe reentry cases are: (1) steep reentry (-90° flight path angle) at escape velocity which resulted in the highest heating rates and external surface temperatures, and (2) orbital decay reentry with its attendant long heating pulse which resulted in the highest internal structural temperatures.

5.3.2. Safety Requirements

There are two safety requirements which must be met during reentry. First, protection will be provided so that, under the worst possible reentry

conditions, the radioisotopic fuel is not released. Second, protection will be provided for the safety system so that it is still operable at impact.

5.3.3. Design Criteria

An aerodynamically oriented reentry configuration is necessary to cause the vehicle to impact on the energy absorbing nose. An oriented configuration also minimizes reentry protection requirements since the most severe heating is generally localized over the small nose region.

Oriented reentry was provided by a flare located just aft of the active radiator area. In addition to providing aerodynamic stability, the flare also reduces the ballistic coefficient and, thus, reduces reentry heating. Therefore, the flare was sized to provide the maximum drag for the minimum weight.

5.3.4. Reentry Heating

Transient aerodynamic heating (and radiative heating at the stagnation point) was calculated for four locations on the reentry vehicle for escape velocity reentry varying in flight path angle from -10 to -90 degrees and for orbital decay reentry. The worst aerodynamic heating occurs during the -90° reentry on the flare due to turbulent flow conditions and results in a maximum heat flux of $2.8(10)^7 \text{ W/m}^2$. The worst total heating occurs during orbital decay reentry at the stagnation point and results in a total heat load of 6200 B/ft^2 . Radiative heating from the shock layer to the stagnation point is only important at reentry angles greater than -50°.

5.3.5. Thermal Protection System

A carbon/graphite fibrous composite, Pyro-Carb 406, was selected for the ablative heat shield. This is the same material used on the SNAP 27 fuel capsule which also had to survive reentry at escape velocity. It affords excellent ablation characteristics common to graphitic materials and yet has a relatively low thermal conductivity in the radial direction.

Ablation calculations were done for the stagnation point to establish the necessary thickness of Pyro-Carb. The worst ablation occurs during re-entry at -10° at escape velocity due to the relatively long heat pulse and high surface temperatures. Total recession under these conditions is 3.64 cm.

A layer of zirconia felt backs up the Pyro-Carb 406 and insulates the underlying structure on the nose and flare, and structure-safety system on the cylindrical body. Thermal conductivity of the felt was allowed to vary with temperature and ambient pressure. The resulting structural temperatures are sufficiently low to allow use of stainless steel.

5.4. IMPACT ON WATER

The most likely abort impact mode is immersion in sea water. Provisions have been incorporated in the design of the RIPS for water flotation and recovery. In the event that the system sinks or is in the water for extended durations, sea water and electrolytic corrosion of the capsules must be considered. However, tungsten has excellent sea water corrosion resistance, with less than 8 microns per year surface recession rate expected.

Because of the small diameter of the curium capsules, they are capable of withstanding large external pressures; hence, there is little chance of rupture or buckling due to water submergence. Thermal shock of the capsules is also a consideration; however, the temperature of the capsules will probably be less than 800°K upon impact due to aerodynamic cooling of the auxiliary radiator prior to impact. Additionally, the RIPS structure is sufficiently sealed to prevent rapid sinking and cooling.

In the event that the curium fuel is exposed to sea water, as a worst-case assumption, dissolution of the fuel would occur but at an extremely slow rate as shown by the following data.

Cm_2O_3 : Solubility and leach rates of $^{244}\text{Cm}_2\text{O}_3$

Ref: ORNL 4663 (Quarterly Report, Dec. 31, 1970)

| Time | Cumulative fraction of Curium dissolved | |
|---------------------------------------|---|---|
| | 1.4 gm pellet | 0.1 gm powder (noncharacterized i.e., mesh size) |
| 116 hr distilled H_2O | 2.6×10^{-5} | 1.5×10^{-3} |
| 116 hr sea H_2O | 2.3×10^{-6} | 8.4×10^{-5} |

5.5. LAND IMPACT

The safety package is designed to survive terminal velocity impact onto a hard unyielding surface by a combination of energy absorption honeycomb and structural support of the heat source within the safety package. Various energy absorption and aerodynamic drag augmentation systems were considered and are discussed in Section 6.4. Parachutes and ballutes were omitted in favor of a passive flare retardation device. Calculated terminal velocity for the 244 cm diameter flare is 45 m/sec.

Computations were performed for soil burial and it was determined that unless the system impacts into a moist or highly plastic soil, earth penetration depth will not cause burial.

Because of the good dynamic and static stability characteristics of the aerodynamic flare, land impact should occur nose-on at 45 m/sec. The honeycomb energy absorption system (Section 6.4) is designed to absorb 100% of the kinetic energy occurring from these conditions. Although impact at high angles of attack cannot be precluded, it was determined that rotation of the system due to wind and gust velocities of 9 m/sec will be less than 1° .

Temperatures of the RTPS on the ground will be $\sim 900^\circ\text{K}$, assuming radiative heat transfer only. In case half the auxiliary radiator is buried due to sand coverage or damage to the radiator, the radiator temperature will rise to 1160°K which will result in melting of the LiH shield.

5.6. LOCATION AND RECOVERY AIDS

Recovery aids are incorporated in the safety package for locating the RTPS following an accidental abort impact onto land or water. In addition to trajectory and tracking data on the spacecraft, a number of techniques and devices will be employed to aid in rapid location of the power supply. These include: (1) radio beacons such as the SARAH system (Search and Rescue and Homing), (2) radar chaff and reflective coatings on the flare base and blast shield, (3) sound fixing and ranging (SOFAR) devices, (4) sea water dye markers, (5) flashing lights, and (6) underwater pingers, and (7) flotation devices.

Dr. Stulken, NASA Landing and Recovery Operations, estimates that with a reliable beacon, and possibly using IR sensing devices, a search team of four aircraft could locate an aborted system within 24 hours. Actual recovery could be accomplished by a parachute team such as the U. S. Air Force's ARRS (Aerospace Rescue and Recovery System). The search and recovery team for an Apollo launch abort (Ref. 19) consists of three aircraft which can locate the command module within three hours, presuming the impact corridor is known to within 100 miles from launch and trajectory data.

For land impact, the preferred approach is to use a radio beacon in conjunction with IR sensing equipment (such as the Firescan System used by the U. S. Forest Service) for location. Special shock mounting provisions will be required and use of special antennas, such as streaming antennas will be required since vehicle orientation on the ground cannot be assured.

Flotation devices are required for water impact recovery, since the RTPS System will not float in its present configuration. For submersion depths greater than 60 meters immediate recovery would be more difficult and would require use of sonar and special deep-sea vehicles. Goodyear ballutes are commonly used for recovery operations, such as retrieval of the cassette cameras on launch vehicles, and their weight, storage requirements, and reliability are known.

Table 5.6 summarizes the location aids considered for the Radioisotope Brayton IRV System and compares masses with those obtained from U. S. Air Force programs. The electronic recovery aids used on the TRANSIT Spacecraft for ocean recovery include a 1 kg underwater acoustic beacon, Model N15A217A, manufactured by Dukane Corporation. This system may also be adequate for the RTPS and results in a much lower mass penalty than the Air Force electronic aids.

TABLE 5.6
LOCATION AND RECOVERY AID DESIGN CHARACTERISTICS

| Component | Mass (kg) | Volume (cc) | Limiting Storage Temperature |
|------------------------------------|---------------------|------------------------|------------------------------|
| Radio beacon | 0.6 | 246 | > 100°C |
| Flashing light | 0.3 | 164 | > 100°C |
| Dye marker | 0.9 | 262 | > 100°C |
| Battery & cables (NiCad type) | 6.3 | 3360 | 80 - 100°C |
| Flotation bag (A.F.) | 6.5 | | |
| Electronic recovery aids (A.F.) | <u>22.1</u> 36.7 | (Optional requirement) | |

6. SAFETY DESIGN ANALYSES

Safety design analyses in support of portions of the safety system which were revised during this study are reported in this section. These include the launch pad fire protection system, blast shielding, reentry and impact protection, and radiation shielding. Design analyses in support of other portions of the system, which have not changed significantly during this study, are contained in Ref. 1 .

6.1. LAUNCH PAD FIRE ANALYSIS

An alternative to the launch escape rocket system of the Phase I reference design (Ref. 1) is a modified safety package which can survive a launch pad abort environment. The thermal environment represents the greatest hazard to the survival of the fuel containment system. To aid in the design and analysis of thermal protection concepts, a simplified thermal model was developed for evaluating the transient response of the system when exposed to the worst-case solid propellant fire environment of 2600°K for 10 minutes. The following sections discuss the model and the design technique used to satisfy the requirement and alternative concepts considered.

6.1.1. Transient Thermal Analysis Model

The TAC2D code (Ref. 20) developed by Gulf General Atomic was used for the launch pad thermal analysis. This code calculates steady-state and transient temperatures in two-dimensional problems by the finite difference method. The configuration of the body to be analyzed is described in the rectangular, cylindrical or circular (polar) coordinate system by orthogonal lines of constant coordinate called grid lines. The grid lines specify an array of nodal elements. Nodal points are defined as lying midway between the bounding grid lines of these elements. A finite difference equation is

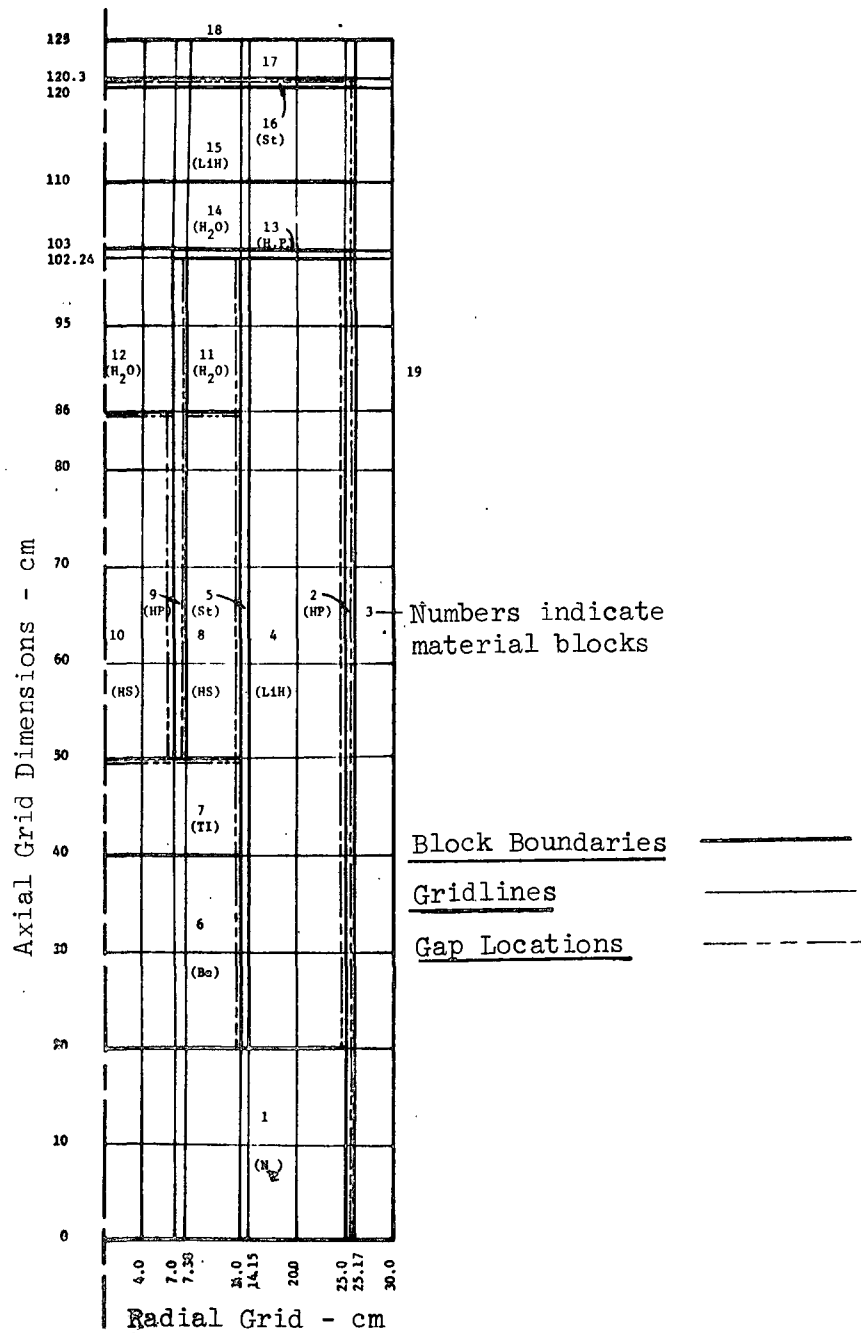


Fig. 6.1 Thermal model geometry for the radioisotope propulsion systems reference design

formulated for each nodal point in terms of its capacitance, heat generation and heat flow paths to neighboring nodal points.

Figure 6.1 shows the model geometry in cylindrical coordinates for the reference design radioisotope system. Each of the major components has been approximated by a rectangular cross-sectional segment defined by the heavier boundary lines. The aerodynamic flare and honeycomb nose material have been neglected for simplicity because they should not have a significant effect on the launch pad thermal response. The block nodes outside the heat pipes were varied according to the specific fire shield design being analyzed.

Table 6.1 gives a detailed summary of the materials, block dimensions and physical properties. For the heat pipes, the thermal conductivity was approximated assuming a 10°C ΔT drop between the average heat source and radiator temperatures. Thermal k and specific heat values for the heat source and thermionic cells were estimated by ratioing properties of the various materials by their volume fraction and assuming a homogeneous distribution of material in the block. Water coolant was used initially and later changed to helium when it was determined that helium could provide adequate heat removal prior to launch. Helium cooling has the advantage of minimizing thermal gradients and thermal cycling of the auxiliary heat pipes.

6.1.2. LiH/Zirconia Heat Storage - Insulator Fire Shield

Protection of the RTPS Safety System from a launch abort fire could be provided simply by wrapping an insulator such as Min-k or zirconia, around the outside of the system. However, unless active devices are employed to remove the insulation immediately after launch, or after a fire, the auxiliary heat pipes could not reject the internal heat without exceeding design operating limits.

Based on thermal analyses of various fire shield designs, it was concluded that a configuration which judiciously utilized a heat storage material and an insulator would result in fire shield design with acceptable mass and overall thermal conductance. Because of its favorable heat capacity, melting point, and neutron shielding properties lithium hydride was selected as the heat storage material. The LiH fire shield surrounds the auxiliary radiator and is in turn surrounded with a layer of high temperature insulation, such

TABLE 6.1
LAUNCH PAD ABORT TRANSIENT THERMAL ANALYSIS MODEL PARAMETERS

| BLOCK | COMPONENT | MATERIAL | NODE GEOMETRY [†] | | | | CONDUCTIVITY (Btu/hr ft °F)* | VOLUMETRIC SPECIFIC HEAT ⁺⁺⁺ (Btu/Ft ³ °F) |
|--------|-----------------------------|---|----------------------------|--------------------------|----------------|-----------------------------|---------------------------------------|---|
| | | | OUTSIDE RADIUS (cm) | INSIDE RADIUS (cm) | HEIGHT (cm) | VOLUME (m ³) | | |
| 1 | Radiator Void | Nitrogen | 25.0 | 0 | 20.0 | .0393 | $3.7(10)^{-3} + 2.1(10)^{-5} DR^{**}$ | 0.30 |
| 2 | Aux. Radiator Heat Pipes | Stainless Steel | 25.17 | 25.0 | 102.24 | .00274 | $1.12(10)^6$ | 157.6 |
| 3, 17 | External Environment | Thermal Dummy | 25.17 | | 125.0 | -- | Fire Environment | 10^6 |
| 4 | Safety Shield | LiH | 25.0 | 14.15 | 82.24 | .1097 | $5.27 - 1.84(10)^{-3} DR^{**}$ | $26.7 + .036 DR^{+++}$ |
| 5 | Internal Structure | Stainless Steel | 14.0 | 14.15 | 20.49 | .00027 | 12.0 | 58.7 |
| 6 | Neutron Shield | Beryllium | 14.0 | 0 | 20.0 | .0123 | 35.0 | 8.8 |
| 7 | Thermionic Cells | Tungsten + S.S. + Void | 14.0 | 0 | 10.0 | .00616 | 9.8 (est.) | 25.5 (est.) |
| 8 | †† Heat Source | WRe + Cm ₂ O ₃ + S.S. + Void | 14.0 | 7.38 | 36.0 | .0160 | 26.3 (est.) | 10.8 (est.) |
| 9 | Aux. Radiator Heat Pipe | Stainless Steel | 7.38 | 7.0 | 20.49 | .00035 | $1.12(10)^6$ | 58.7 |
| 10 | †† Heat Source | Same as Node 8 | 7.0 | 0 | 36.0 | .00554 | 26.3 | 10.8 |
| 11 | Water Coolant | Water & Vapor | 14.0 | 7.38 | 16.24 | .00722 | $0.35(+)DR^{***}$ $+ 0.013(+)DR$ | $1.0(+)DR^{**}$ $+ 0.44(+)DR$ |
| 12 | Water Coolant | Water & Vapor | 7.0 | 0 | 17.0 | .00262 | Same 11 | Same 11 |
| 13 | Aux. Radiator Heat Pipe | Stainless Steel | 25.17 | 7.0 | 0.76 | .0014 | $1.12(10)^6$ | 58.7 |
| 14 | Water Coolant | Water & Vapor | 25.17 | 0 | 7.0 | .0139 | Same 11 | Same 11 |
| 15 | Top Safety Shield | LiH | 25.17 | 0 | 10.0 | .0199 | Same 4 | Same 4 |
| 16 | Top Structure | Stainless Steel | 25.17 | 0 | 0.31 | .00062 | 12.0 | 58.7 |
| 18, 19 | External Coolant | Fire Environment | 30 | 0 | 125 | -- | High | High |
| 20, 21 | Internal Coolants | Adiabatic Boundaries | 30 | 0 | 125 | -- | Low | Low |

† Boundary dimensions for cylindrical coordinate model.

* Engineering units used in TAC2D (Thermal Analysis Code using the finite difference method).

** DR is the node temperature in °R.

†† Volumetric heating rate = $2.224(10)^5$ Btu/hr ft³

*** (+)DR = $(1 - DR/1540)$ and (+)DR1 = $DR/1540$

+++ C_p given for 0 to 1727°R. At 1727°R, the heat of fusion of 1120 Btu/lb is applied and above 1727°R C_p = 93 Btu/ft³ °F

NOTE: British units used for consistency with computer program for thermal analysis - 1 Btu/hr ft³ °F = 1.73 W/m³ °K; 1 Btu/ft³ °F = 6.71 x 10⁴ J/m³ °K; 1°R = 5/9 °K

as zirconia felt, which lowers the heat flux into the LiH from a fire. The mass of LiH required depends on its heat capacity (sensible heat plus latent heat) and the thickness of insulation for a specified fire environment. From the best available data on LiH, the sensible heat was taken at 1600 Btu/lb (3.7×10^6 J/kg), and the latent heat at 1200 Btu/lb (2.8×10^6 J/kg).

Figure 6.2 shows tradeoff curves of LiH and insulation mass with LiH thickness for various values of thermal insulation conductivity. These curves assume that the LiH absorbs all of the fire heat conducted through the insulation by changing from a solid at ambient temperature to a liquid at the boiling point for LiH of 1267°F (960°K). Increasing the LiH thickness diminishes the thickness of insulation required according to the relationship (for a ten minute 2600°K fire):

$$t_{\text{LiH}} = 0.594 k_{\text{insul}} / t_{\text{insul}}$$

where t = thickness in inches, and

k = insulation conductivity in Btu/hr ft°F.

It can be observed from the lower curves in Fig. 6.2 that there is a minimum shield mass for a specific insulation conductivity and LiH thickness. However, to eliminate the requirement of having to remove the shield immediately after the fire, the conductivity of the fire shield should be high enough in the equilibrium case (i.e., radiation of the internal heat to ambient conditions) to limit the operating temperature of the auxiliary heat pipes to approximately 1200°K (Section 6.1.4). Consequently, since the equilibrium radiator temperature is ~900°K, the allowable ΔT across the insulation is ~300°C. To illustrate how the fire shields meet this criteria, the upper curves in Fig. 6.2 give the variation in ΔT across the fire shield for different LiH conductivities. These curves show that for the conditions assumed (i.e., all the fire heat to be absorbed by the LiH) the desired equilibrium ΔT can be achieved only by increasing the LiH conductivity. However, as discussed below, this shield design can meet the desired design conditions when the thermal capacitance of the entire system is considered.

The transient thermal response of the heat pipes during and following a launch pad fire was evaluated for various insulation thicknesses, using the

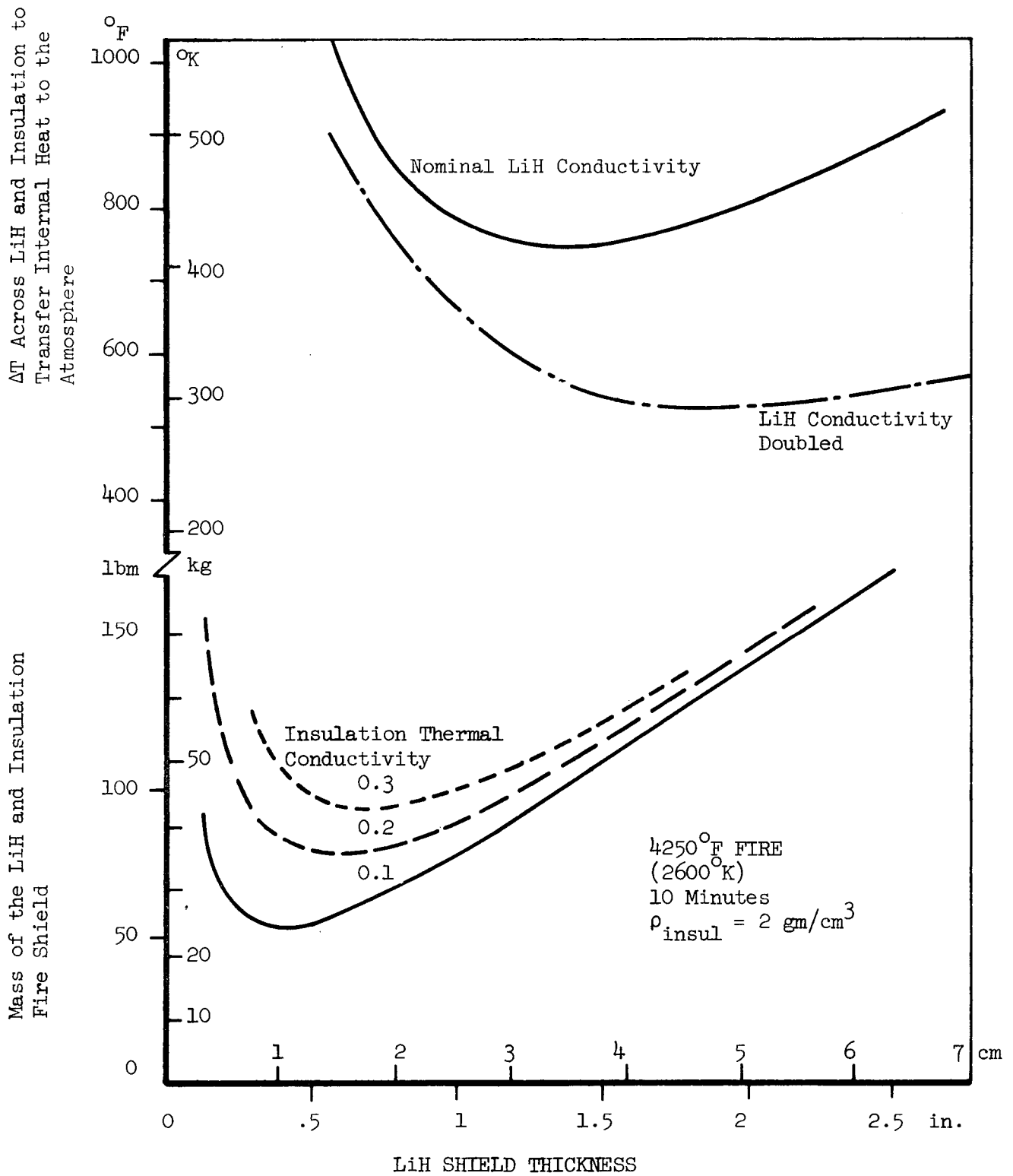


Fig. 6.2 Tradeoff of Fire Shield mass and equilibrium ΔT with LiH shield thickness

detailed thermal model developed for the system. Results of these analyses are summarized in Table 6.2; and temperatures for insulation thicknesses of 0.12 and 0.048-inch are plotted in Figures 6.3 and 6.4. The table results for the detailed thermal model show that the heat pipe temperature will be below 1200°K for insulation thickness to 0.048-inch, and that the equilibrium temperature at 10^5 seconds (28 hours) for 0.12-inch insulation, is below 1200°K.* However, Fig. 6.4 shows that for the thinner insulation section the peak temperature occurs at about 700 seconds and exceeds 1250°K. The table also shows that using N_2 in place of the water coolant, and modifying the LiH conductivity has little effect on the heat pipe thermal response. Verification of these results was obtained using a simplified lumped thermal model which included a 0.15 cm stainless steel structure around the LiH.

Tables 6.3 and 6.4 present computer printout results of the system temperatures at the end of the launch fire (10 minutes) and after 10,000 seconds (2.7 hr), which represents the length of time that may be required to recover the system after a launch pad abort. The initial conditions for these analyses assumed the fuel at 533°K (500°F) and the system at 311°K (100°F). From Table 6.3, it can be observed that most of the temperature drop between the fuel and fire occurs across the zirconia insulation, and that the heat pipe temperature is in a safe operating region and closely follows that of the LiH surrounding the heat pipes, which is 1.9 cm thick. The heat capacity of the inner 10 cm thick LiH biological shield is sufficiently large so that its temperature does not exceed the melting point of LiH (1267°F, 960°K) 2.8 hours after a launch abort fire, as observed in Table 6.4. This table also shows the temperature drop across the fire shield to transfer the internal heat to the atmosphere, assuming radiation and convection to 140°F (330°K) air. Other temperatures of interest include those of the stainless steel tanks which contain the LiH radiation shield. These were also found to be in a safe operating region except for the nose surface temperatures (line 16, Table 6.3), which would also be below 1200°K if the reentry protection insulation were taken into account in the thermal model.

* Actual equilibrium temperatures are below those shown in Table 6.2 due to the lower heat input (44.2 kW) compared to that used for this analysis (51.75 kW).

TABLE 6.2
SUMMARY OF TRANSIENT HEAT PIPE TEMPERATURES DURING
A LAUNCH PAD FIRE OF 2600 K FOR 10 MINUTES

| Insulation Thickness | Maximum Heat Pipe Temperature in Degree K and (°F) | | | | |
|--|--|----------------|---------------|---------------|----------------------------|
| | 600 | 1000 | 3500 | 10,000 | 35,000 100,000 |
| | (Time in Seconds) | | | | |
| 0.238" (0.6 cm) | 879 (1122) | 914 (1186) | 852 (1073) | 988 (1319) | |
| 0.120" (0.3 cm) | 935 (1223) | 950 (1250) | 872 (1110) | 966 (1278) | |
| 0.120" (0.3 cm) (Revised LiH Properties)* | 926 (1206) | 957 (1262) | 896 (1152) | 989 (1321) | 1122 1238 (1559) (1769) |
| 0.048" (0.12 cm) | 1190 (1682) | 1122 (1560) | 936 (1225) | 967 (1281) | 1039 1127 (1411) (1569) |
| 0.048" (0.12 cm) (N ₂ in place of water) | 1198 (1697) | 1134 (1582) | 934 (1330) | 985 (1313) | |

* The LiH/Thermal Conductivity was revised from a constantly decreasing value with temperature, as shown in Table 6.1, to one that leveled off to a value of 2 Btu/hr ft °F above 1760°R.

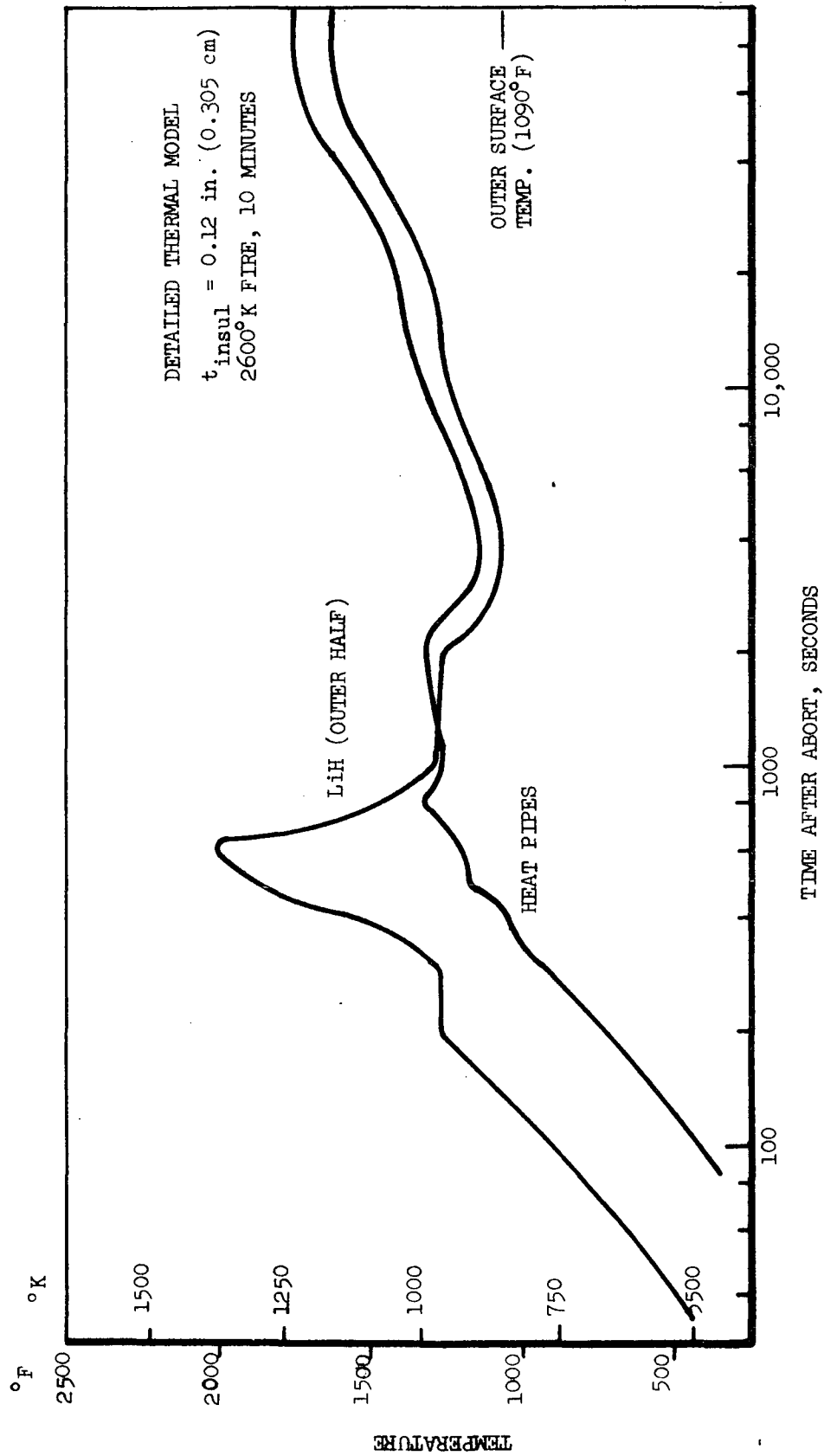


Fig. 6.3. Transient temperature profiles of RTPS components during a launch pad fire

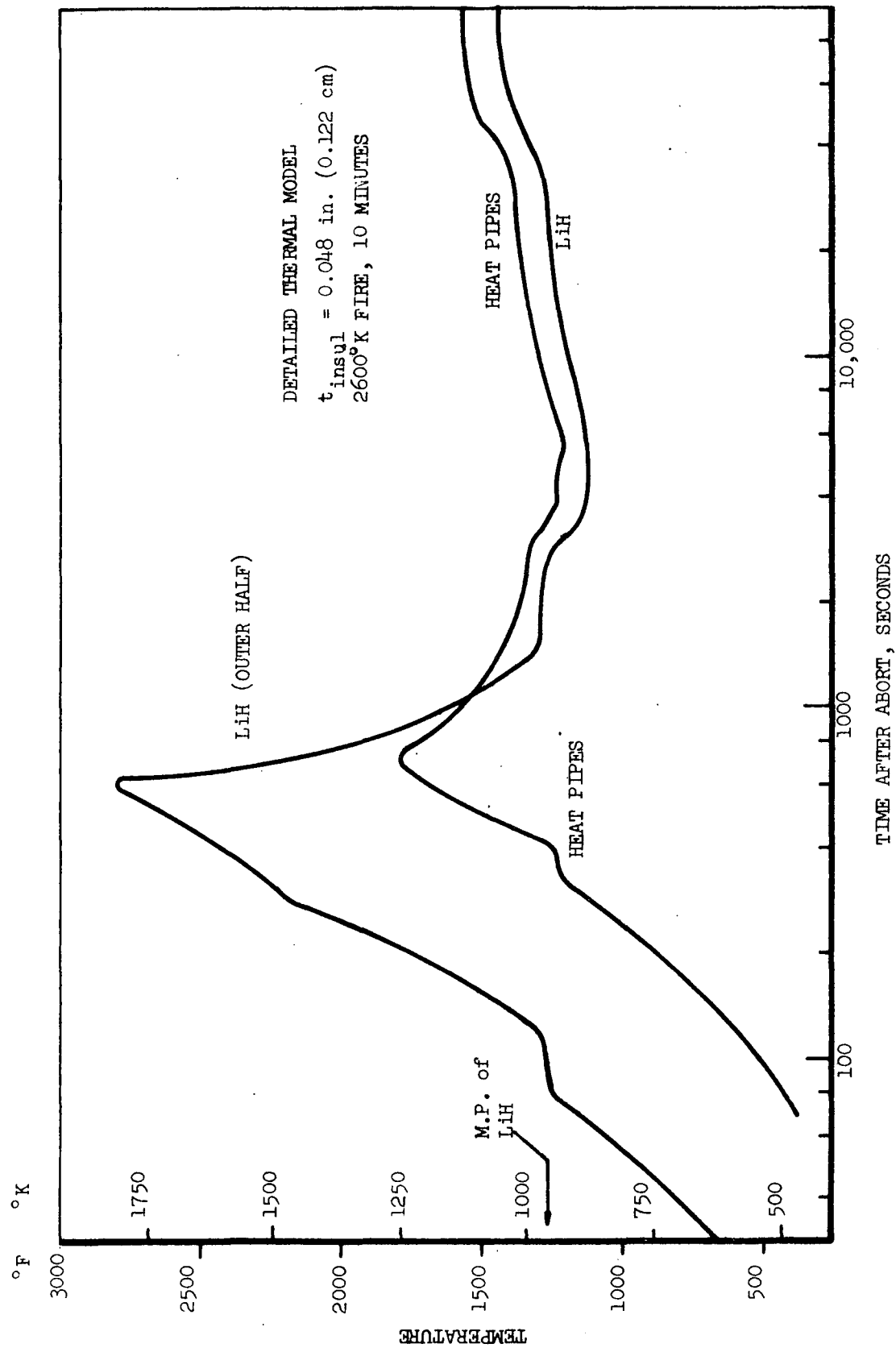


Fig. 6.4. Transient temperature profiles of RPS components during a launch pad fire

TABLE 6.3

RTPS SYSTEM TEMPERATURES FROM TRANSIENT THERMAL ANALYSIS COMPUTER PRINT OUT
(0.12" INSULATION, 2600°K, 10 MINUTE FIRE)

THE CURRENT TIME IS .1667 HOURS = 10.0000 MINUTES = 600.00000 SECONDS

TEMPERATURES (F)

THE RADIAL (I) DIRECTION IS HORIZONTAL
THE AXIAL (J) DIRECTION IS VERTICAL

| | 1 | 2 | 3 | 4 | 5 | 6 | 7 | 8 | 9 | 10 | 11 | 12 | 13 |
|----|---|------|------|------|------|------|------|------|------|------|------|------|------|
| 1 | 0 | 0 | 0 | 0 | 0 | 0 | 0 | 0 | 0 | 0 | 0 | 0 | 0 |
| 2 | 0 | 690 | 722 | 747 | 787 | 885 | 943 | 1117 | 1199 | 1289 | 2009 | 3301 | 4250 |
| 3 | 0 | 391 | 418 | 442 | 479 | 589 | 658 | 952 | 1199 | 1289 | 2009 | 3301 | 4250 |
| 4 | 0 | 128 | 128 | 128 | 128 | 119 | 121 | 241 | 1199 | 1289 | 2009 | 3301 | 4250 |
| 5 | 0 | 141 | 141 | 141 | 140 | 121 | 121 | 240 | 1198 | 1289 | 2009 | 3301 | 4250 |
| 6 | 0 | 213 | 208 | 205 | 205 | 149 | 138 | 244 | 1198 | 1289 | 2009 | 3301 | 4250 |
| 7 | 0 | 1327 | 1257 | 1206 | 1241 | 1088 | 387 | 282 | 1198 | 1288 | 2008 | 3301 | 4250 |
| 8 | 0 | 1346 | 1265 | 1206 | 1272 | 1120 | 402 | 285 | 1198 | 1288 | 2008 | 3301 | 4250 |
| 9 | 0 | 1346 | 1265 | 1206 | 1274 | 1122 | 402 | 285 | 1198 | 1290 | 2010 | 3302 | 4250 |
| 10 | 0 | 1340 | 1262 | 1205 | 1259 | 1100 | 380 | 280 | 1198 | 1290 | 2010 | 3302 | 4250 |
| 11 | 0 | 124 | 213 | 1204 | 144 | 173 | 159 | 257 | 1198 | 1290 | 2010 | 3302 | 4250 |
| 12 | 0 | 106 | 213 | 1203 | 149 | 350 | 349 | 433 | 1198 | 1289 | 2012 | 3302 | 4250 |
| 13 | 0 | 107 | 212 | 1201 | 1201 | 1200 | 1200 | 1200 | 1200 | 1476 | 2065 | 3324 | 4250 |
| 14 | 0 | 111 | 114 | 130 | 137 | 137 | 137 | 151 | 783 | 1577 | 2108 | 3342 | 4250 |
| 15 | 0 | 737 | 737 | 737 | 738 | 745 | 750 | 845 | 1219 | 1596 | 2159 | 3364 | 4250 |
| 16 | 0 | 4035 | 4037 | 4039 | 4041 | 4050 | 4056 | 4090 | 4127 | 4097 | 4123 | 4191 | 4250 |
| 17 | 0 | 4110 | 4111 | 4113 | 4115 | 4124 | 4130 | 4158 | 4185 | 4190 | 4199 | 4207 | 4250 |
| 18 | 0 | 4250 | 4250 | 4250 | 4250 | 4250 | 4250 | 4250 | 4250 | 4250 | 4250 | 4250 | 0 |

TABLE 6.4

RTPS SYSTEM TEMPERATURES FROM TRANSIENT THERMAL ANALYSIS COMPUTER PRINT OUT
(0.12" INSULATION, 2600°K, 10 MINUTE FIRE)

THE CURRENT TIME IS 2.7778 HOURS = 166.6667 MINUTES = 10000.00012 SECONDS

TEMPERATURES (F)

THE RADIAL (I) DIRECTION IS HORIZONTAL
THE AXIAL (J) DIRECTION IS VERTICAL

| | 1 | 2 | 3 | 4 | 5 | 6 | 7 | 8 | 9 | 10 | 11 | 12 | 13 |
|------------|---|------|------|------|------|------|------|------|------|------|------|------|-----|
| 1 | 0 | 0 | 0 | 0 | 0 | 0 | 0 | 0 | 0 | 0 | 0 | 0 | 0 |
| 2 N_2 | 0 | 1205 | 1210 | 1213 | 1220 | 1236 | 1248 | 1284 | 1302 | 1238 | 1148 | 1006 | 140 |
| 3 | 0 | 1151 | 1153 | 1155 | 1158 | 1168 | 1175 | 1250 | 1302 | 1238 | 1148 | 1006 | 140 |
| 4 BE | 0 | 1112 | 1111 | 1110 | 1108 | 1057 | 1019 | 1124 | 1302 | 1239 | 1148 | 1006 | 140 |
| 5 | 0 | 1132 | 1131 | 1130 | 1128 | 1079 | 1039 | 1134 | 1303 | 1239 | 1148 | 1006 | 140 |
| 6 $TiCl_3$ | 0 | 1216 | 1216 | 1219 | 1225 | 1164 | 1110 | 1170 | 1303 | 1239 | 1149 | 1007 | 140 |
| 7 | 0 | 1455 | 1378 | 1321 | 1619 | 1581 | 1274 | 1244 | 1304 | 1240 | 1149 | 1007 | 140 |
| 8 $FUEL$ | 0 | 1461 | 1380 | 1321 | 1643 | 1604 | 1290 | 1257 | 1305 | 1241 | 1150 | 1008 | 140 |
| 9 | 0 | 1460 | 1379 | 1319 | 1646 | 1607 | 1279 | 1256 | 1306 | 1242 | 1150 | 1008 | 140 |
| 10 | 0 | 1455 | 1377 | 1318 | 1644 | 1602 | 1272 | 1242 | 1307 | 1243 | 1151 | 1009 | 140 |
| 11 | 0 | 215 | 327 | 1316 | 354 | 1144 | 1133 | 1195 | 1308 | 1243 | 1151 | 1009 | 140 |
| 12 H_2O | 0 | 183 | 335 | 1314 | 384 | 1188 | 1186 | 1231 | 1309 | 1231 | 1131 | 994 | 140 |
| 13 | 0 | 199 | 334 | 1313 | 1312 | 1311 | 1310 | 1309 | 1309 | 801 | 736 | 682 | 140 |
| 14 | 0 | 213 | 214 | 217 | 218 | 218 | 218 | 219 | 221 | 471 | 470 | 448 | 140 |
| 15 LiH | 0 | 481 | 481 | 480 | 479 | 476 | 474 | 465 | 460 | 433 | 427 | 408 | 140 |
| 16 | 0 | 412 | 411 | 411 | 410 | 409 | 409 | 406 | 405 | 405 | 404 | 396 | 140 |
| 17 | 0 | 410 | 409 | 409 | 409 | 408 | 407 | 405 | 404 | 403 | 403 | 403 | 140 |
| 18 | 0 | 140 | 140 | 140 | 140 | 140 | 140 | 140 | 140 | 140 | 140 | 140 | 0 |

LiH .15"
INSUL. .12"

Based on the transient thermal analysis results, the recommended insulation thickness is 0.12-inch (0.31 cm) which corresponds to an insulation conductance of 2.5 Btu/hr ft °F (in.) or 0.017 watts/cm² °K. Table 6.5 summarizes the design characteristics for the launch abort fire shield based on this insulation conductivity and the LiH thickness for minimum mass. A conductivity of 0.3 Btu/hr ft °F was assumed for zirconia; and although this is a representative value for the foam, it is somewhat greater than supplier data on the felt material. Further optimization of the fire shield would require instrumented thermal tests which would better simulate the insulation thermal response and the effects of interface thermal impedance.

TABLE 6.5

CHARACTERISTICS OF THE REVISED LiH/ZIRCONIA LAUNCH
PAD ABORT FIRE SHIELD (2600°K FIRE, 10 MINUTES)

| | |
|-------------------------------------|---------------------|
| LiH thickness | 1.9 cm (0.75 in.) |
| Stainless steel structure thickness | 0.152 cm (0.06 in.) |
| Zirconia thickness | 0.31 cm (0.12 in.) |
| Shield length | 142 cm (361 in.) |
| LiH density | 0.75 gm/cc |
| Stainless steel density | 8.0 gm/cc |
| Zirconia density | 0.9 gm/cc |
| LiH mass | 32.6 kg |
| Stainless steel mass | 28.4 kg |
| Zirconia mass | 6.5 kg |
| Total shield mass | 67.5 kg |

6.1.3. Alternate Fire Protection Concepts

Various design concepts for protecting the auxiliary radiator and safety package from damage caused by a launch pad fire were considered and analysed. These are discussed briefly in the following subsections.

6.1.3.1. Heat Storage Materials. Protection of the radioisotope safety system with heat storage material represents a brute force method to ensure fire survival, and one that will not result in overheating during a land impact abort situation. However, the masses of the seven different candidate materials were found to be immense when designed for maximum fire temperatures and durations. For illustration, Table 6.6 presents characteristics of candidate heat shield materials which have melting points near or below the heat pipe temperature limit of 1200°K . Some of the lower melting point materials, such as lead and tin, are included only for comparison since their mass is prohibitive. The computed thermal shield parameters are based upon the assumption that all of the fire heat input must be absorbed by a phase change of the heat shield. The results show that the shield mass is high for all the materials relative to the total mass for the reference design of 739.5 kg. LiH gives the lowest mass, followed by aluminum and magnesium. However, because of the low thermal conductivity of LiH, the equilibrium ΔT is excessively large unless techniques are used to shunt heat through the shield.

A lighter weight shield may also be obtained by using the fire heat to vaporize the shield material. Magnesium, for example, has a boiling temperature of 1390°K and a heat of vaporization of $5.31(10)^6$ joules/kg. Thus a shield mass of 377 kg or less could absorb the total fire input energy. Problems are encountered, however, when considering how to contain the molten material and vent the vapor without the liquid material flowing out the vent. The selection of materials is also limited, since most elements have high boiling points.

Another consideration is the effect of shorter postulated fire durations on heat storage shield requirements. Mass is proportioned to fire time, so that a LiH shield of 90 kg and 6.5-cm thickness would provide protection for

TABLE 6.6
CHARACTERISTICS OF HEAT STORAGE MATERIAL TO PROTECT
THE SAFETY SYSTEM RADIATOR FROM A LAUNCH PAD FIRE

| THERMAL SHIELD MATERIALS | MELTING POINT (°K) | LATENT HEAT OF FUSION (Joules/kg) | DENSITY (gm/cm ³) | THERMAL * CONDUCTIVITY (watts/cm °K) | SHIELD PARAMETERS TO ABSORB FIRE HEAT OF 2(10) ⁹ JOULES BY PHASE CHANGE | | |
|--------------------------------|--------------------------|---|----------------------------------|---|---|-----------------------------|---|
| | | | | | Mass (kg) | Volume (m ³) | Thickness** ΔT(Equil) ⁺ (°K) |
| Copper | 1356 | 2.05 (10) ⁵ | 8.96 | 3.5 | 10,000 | 1.12 | 32.7 |
| Lithium Hydride | 960 | 2.6 (10) ⁶⁺⁺ | 0.75 | 0.04 | 770 | 1.03 | 30.8 |
| Aluminum | 933 | 3.98 (10) ⁵ | 2.7 | 2.68 | 5,000 | 1.85 | 46.4 |
| Magnesium | 923 | 3.62 (10) ⁵ | 1.74 | 1.45 | 5,500 | 3.16 | 66.0 |
| Zinc | 692 | 1.13 (10) ⁵ | 7.13 | 1.0 | 1.8(10) ⁴ | 2.48 | 56.4 |
| Lead | 600 | 2.31 (10) ⁴ | 11.34 | 0.32 | 8.7(10) ⁴ | 8.5 | 120.7 |
| Tin | 505 | 5.91 (10) ⁴ | 7.3 | 0.60 | 3.4(10) ⁴ | 4.66 | 84.1 |
| | | | | | | | 196 |

* For temperatures between 700 to 1000°K.

** Thickness of annular section 103 cm long surrounding the 50.3 cm diameter safety system radiator.

⁺ Temperature drop across the thermal storage material to transfer the heat source energy to the atmosphere.

⁺⁺ This is comparable to the heat of vaporization for water.

a one-minute 2600 K fire. The equilibrium temperature drop across the shield, however, is less sensitive to time and would be approximately 460°K, which is excessively high. Corresponding aluminum shield mass would be 586 kg, which is also prohibitively high.

6.1.3.2. Thermal Switch Composite Materials. Thermal switch composites are metal-impregnated porous ceramics capable of switching their thermal conductivity from high values at low temperatures to low values at elevated temperatures, such as encountered during reentry and a launch pad fire. Numerous combinations of composite materials have been tested and developed, including silver-impregnated silica, silver/alumina, silver/zirconia, copper/zirconia, nickel/zirconia and palladium/zirconia (Refs. 21, 22). The mechanism for switching the thermal conductivity of these materials involves the change of a uniform thin metallic coating deposited on the surface of the porous ceramic to discontinuous spherical droplets as the metal melts and de-wets the ceramic surface.

Of the various composites considered, silver/zirconia felt has the most desirable characteristics for a fire thermal protection system. Silver melts at 1234°K (1760°F) and zirconia has been tested to 2800°K. The zirconia-felt has a lower density and conductivity than zirconia-foam, and can be produced to a higher quality material. Thermal conductivity of the composite is proportional to the volume of metal added to the ceramic, where ~ 10% is considered a practical limit. Since the density for silver is 10.5 gm/cc, compared to ~ 0.9 gm/cc to certain types of zirconia-felt, approximately 1 gm/cc of silver could be impregnated into the ceramic. Assuming that the conductivity of the composite is proportional to the volume of silver, a theoretical value of 21 Btu/hr ft°F (0.36 watt/cm°C) could be obtained.

Results of transient thermal response of the system using a thermal switch fire shield are shown in Figure 6.5. The computed temperatures indicate that the outer layer rapidly increases in temperature until the metal melts, thus halting the temperature rise until the heat source internal heat generation begins to take over. For this thickness of material, the

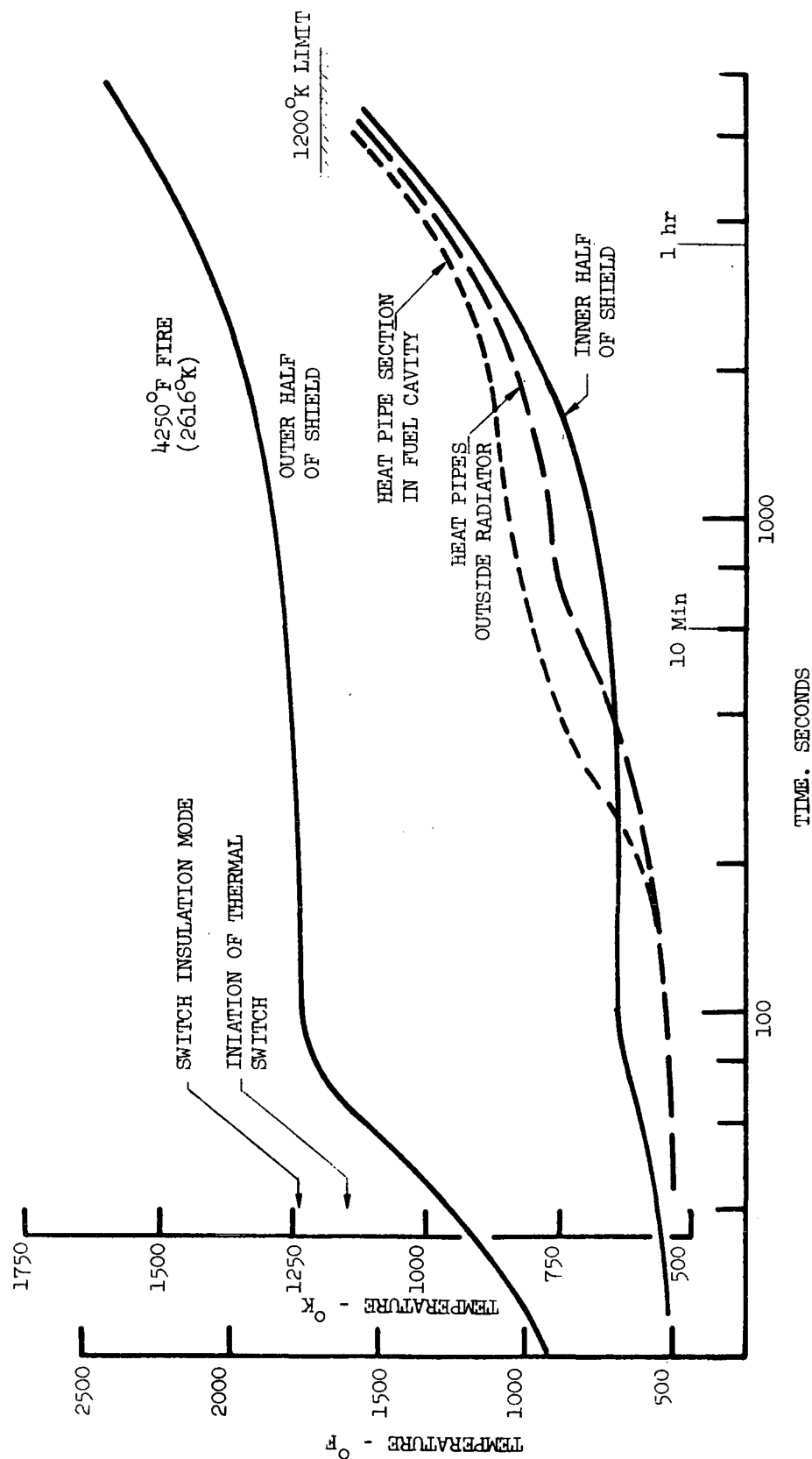


Fig. 6.5. Transient thermal response of auxiliary radiator heat pipes and thermal switching shield in a 2616°K launch pad fire

safety system could withstand a severe solid propellant fire for up to two hours.

Transient thermal cases were repeated for shield thicknesses down to 1.5 cm. These thinner sections were also found to give good fire protection. Characteristics of a preliminary thermal-switch-shield design for fire protection are given in Table 6.7. This shield thickness will provide protection against the most severe solid propellant fire for up to 2 hours. After this time it will be necessary to remove the shield or provide some special means of cooling the system to prevent meltdown. Since active control systems or rapid location of the system after a fire would be required to accomplish this, the concept is considered less desirable than the insulation/heat storage design.

6.1.3.3. Thermal Expansion Radiation Shields. Another potential concept for protecting the safety system during a launch pad fire is to surround the auxiliary radiator with concentric radiation shields. These shields could be sized to provide an interference, low thermal resistance fit during radiation to ambient conditions, and to separate when exposed to a fire due to differential thermal expansion between the cooler inner shields and the hotter outer layers. Such shields would need to have a relatively high coefficient of thermal expansion, low conductivity to minimize contact resistances, low emissivity and high temperature capabilities.

The performance of an ideal radiation shield system can be evaluated considering only radiant heat exchange, where the following expression relates the number of shields and heat transfer:

$$Q_{\text{RAD}} = \sigma (A_F T_F^4 - A_R T_R^4) \left(\frac{F}{n+1} \right)$$

where,

- Q_{RAD} = radiant heat flow through the shields,
- A = areas of the shield next to the fire and radiator,
- F = radiant interchange factor = $\epsilon_s / (2 - \epsilon_s)$ for shields of equal area and emissivity (ϵ_s),
- n = number of radiation shields, and
- σ = Stefan-Boltzmann constant.

TABLE 6.7
PRELIMINARY DESIGN CHARACTERISTICS OF A THERMAL SWITCH
COMPOSITE SHIELD FOR LAUNCH DAY FIRE PROTECTION

| | |
|--|---|
| Material | Silver impregnated Zirconia Felt |
| Switching Temperature | 1234°K (1762°F) |
| Thermal Conductivity before Switching | 0.173 watts/cm°C |
| Thermal Conductivity after Switching | 0.0017 watts/cm°C |
| Reference Thickness | 1.52 cm |
| Shield Volume | 30,000 cm ³ |
| Shield Mass | 56.4 kg |
| Heat Pipe Temperature (2600 K Fire) | 830°K (at t = 1000 Sec) 1160°K (at t = 5000 Sec) |
| Outer half of Heat Shield (2600 K Fire) | 1550°K (at t = 5000 Sec) |
| Temperature drop across the Shield before Switching | 27°K (Radiation to atmosphere) |

In addition to radiant heat, conducted heat through the gas between shields and contact resistance between adjacent shields must also be considered. To evaluate the transient thermal behavior of such shields, the system thermal model was modified to include five stainless steel radiation shields, of 0.15 cm thickness each, around the auxiliary radiator. The shields were thermally coupled by a radiation gap filled with a gas of variable conductivity to simulate different gap thicknesses, contact resistance or gas pressures. Figure 6.6 shows transient temperature profiles for cases which attempt to bracket the probable shield gap, conducted heat flow and emissivity, when exposed to a 3000°F (1900°K) launch pad fire. All cases exceed the allowable heat pipe temperature limit in less than 500 seconds. The corresponding response for a 2600°K fire was much less, exceeding the radiator temperature limit in approximately 140 seconds. These rapid response trends indicate that this shield concept does not provide the necessary thermal protection to assure system survival in a launch pad fire. Furthermore, this shield concept is subject to numerous practical design uncertainties, such as assuring concentricity, integrity after impact, separation of shields, and others.

6.1.4. Auxiliary Radiator Heat Pipes

Protection of the radioisotope heat source during and after a launch pad fire will depend on the ability of the potassium filled auxiliary heat pipes to function. Because of the increase in potassium vapor pressure with temperature, and corresponding decrease in heat pipe strength, it will be necessary to limit the temperature rise. For a conservative approximation, this temperature limit was selected as that which would cause rupture of the heat pipe tubes in 1000 hours. Figure 6.7 shows potassium vapor pressure, heat-pipe hoop stress and 1000-hour rupture stress of various high temperature, oxidation resistant alloys. The tube rupture stress is based on an outside diameter of 0.73 cm and inside diameter of 0.71. Material properties were obtained from Ref. 23 and supplier data brochures.

For the reference design stainless steel radiator heat pipes to survive, they must operate below 1200°K (1700°F). This limit can be raised to 1250°K

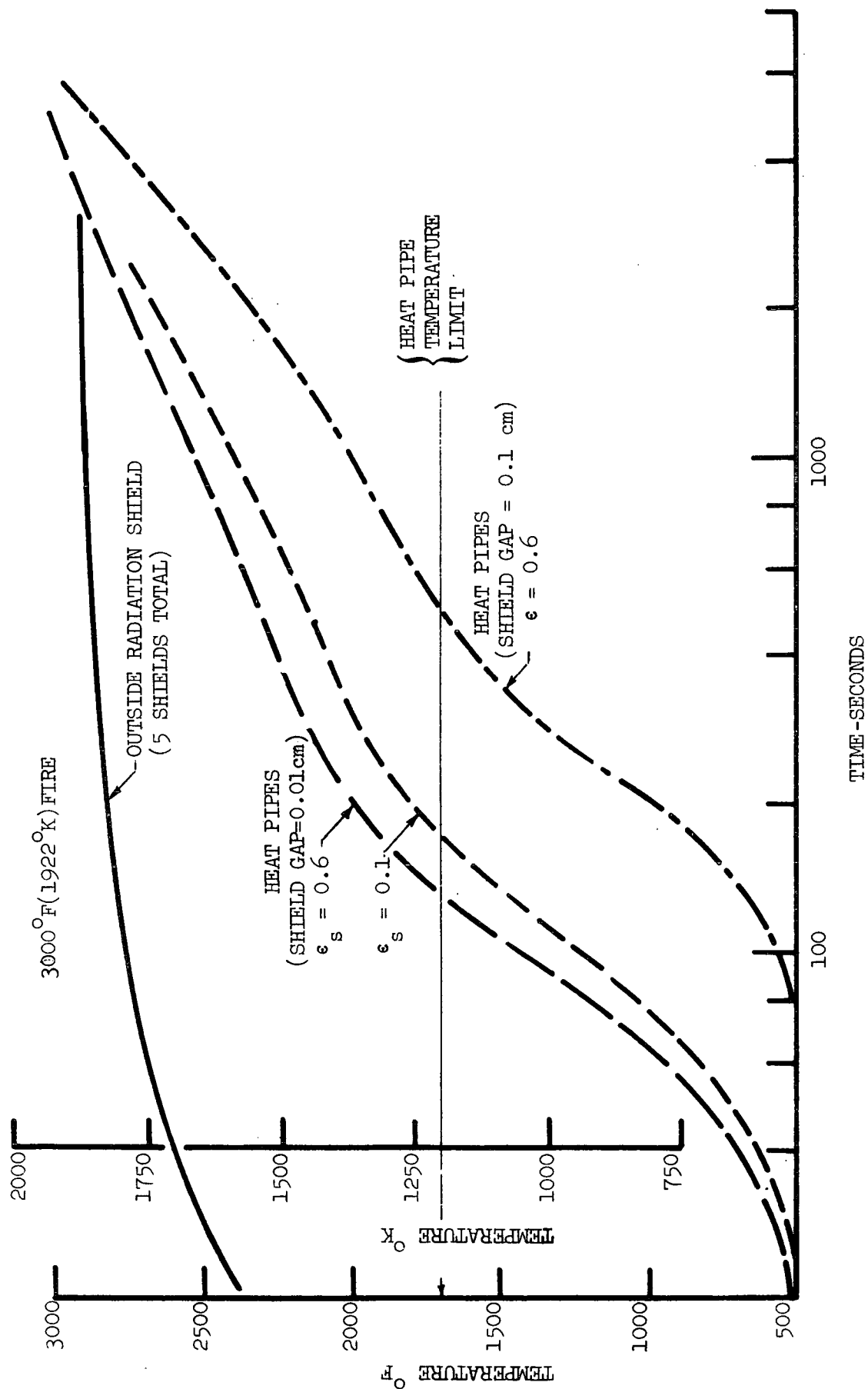


Fig. 6.6. Transient thermal response of the auxiliary radiator heat pipes surrounded by radiation shields and exposed to a launch pad fire

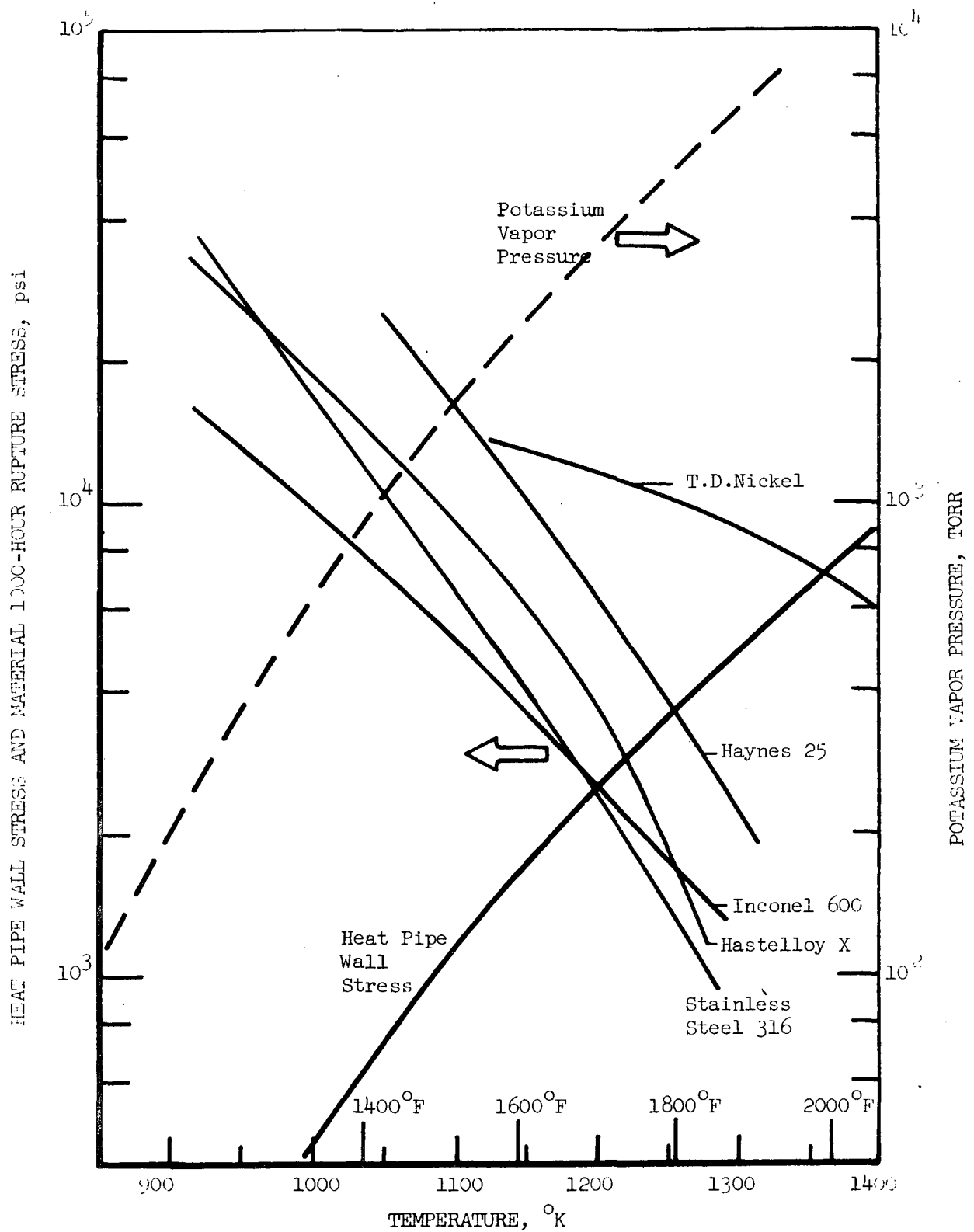


Fig. 6.7. Potassium vapor pressure, auxiliary radiator heat pipe stress and material 1000-hour rupture stress as a function of heat pipe temperature

with Haynes 25 tubes and 1360°K with T.D. nickel. Another alternative for higher temperatures is to increase the heat pipe wall thickness or change the working fluid to sodium. Effects of these alternatives on heat pipe operating temperature are shown in Figure 6.8. The curves show that to achieve a 100°K increase in temperature, the thickness would increase from 0.01 cm to 0.06 cm using K, or to 0.03 cm using Na. Since the present mass of the heat pipes is 10.5 kg, increasing the wall thickness may increase the mass 50 kg. Use of sodium in place of potassium results in only a 40°K improvement. Both of these options represent possible alternatives to the Safety System design capability.

6.2. BLAST SHIELDING

A shield is required to protect the radioisotope heat source auxiliary radiator, aerodynamic flare, and other safety equipment from damage caused by shrapnel and the overpressure environment accompanying a booster explosion. Blast environments from the reference Titan IIID/Centaur vehicle were discussed in Section 5.2. Due to the inadequacy of fragment shield analytical models, the approach generally taken is to test the heat source or shield by impacting it with projectiles which simulate the expected worst-case environment, such as shown in Table 5.5 for Pioneer.

A comparison of blast shield designs was made based on heat source materials and thicknesses which have been subjected to some form of fragment or meteoroidal design analysis testing. Table 6.8 summarizes the various systems and graphically compares the computed mass of a circular shield of 120 cm diameter, which corresponds to the flare diameter of the reference design safety system of Phase I (Ref. 1), and is sufficient for shadow shielding of the auxiliary radiator. Because of its toughness, high strength-to-weight ratio and temperature capabilities, titanium is considered to be an excellent choice for a fragment shield. This material was specifically selected for the Apollo isotope heaters (15 watt units), and successfully withstood some 55 safety tests which included exposure to aluminum tank fragments at 2800 fps. T-111 also seems to be a possible choice based on safety tests on the TRANSIT capsule with 41 gm Ti fragments impacted at 226 mps, a 1.6 kg electronic box impacted at 95 mps and an 0.4 kg igniter at 363 mps.

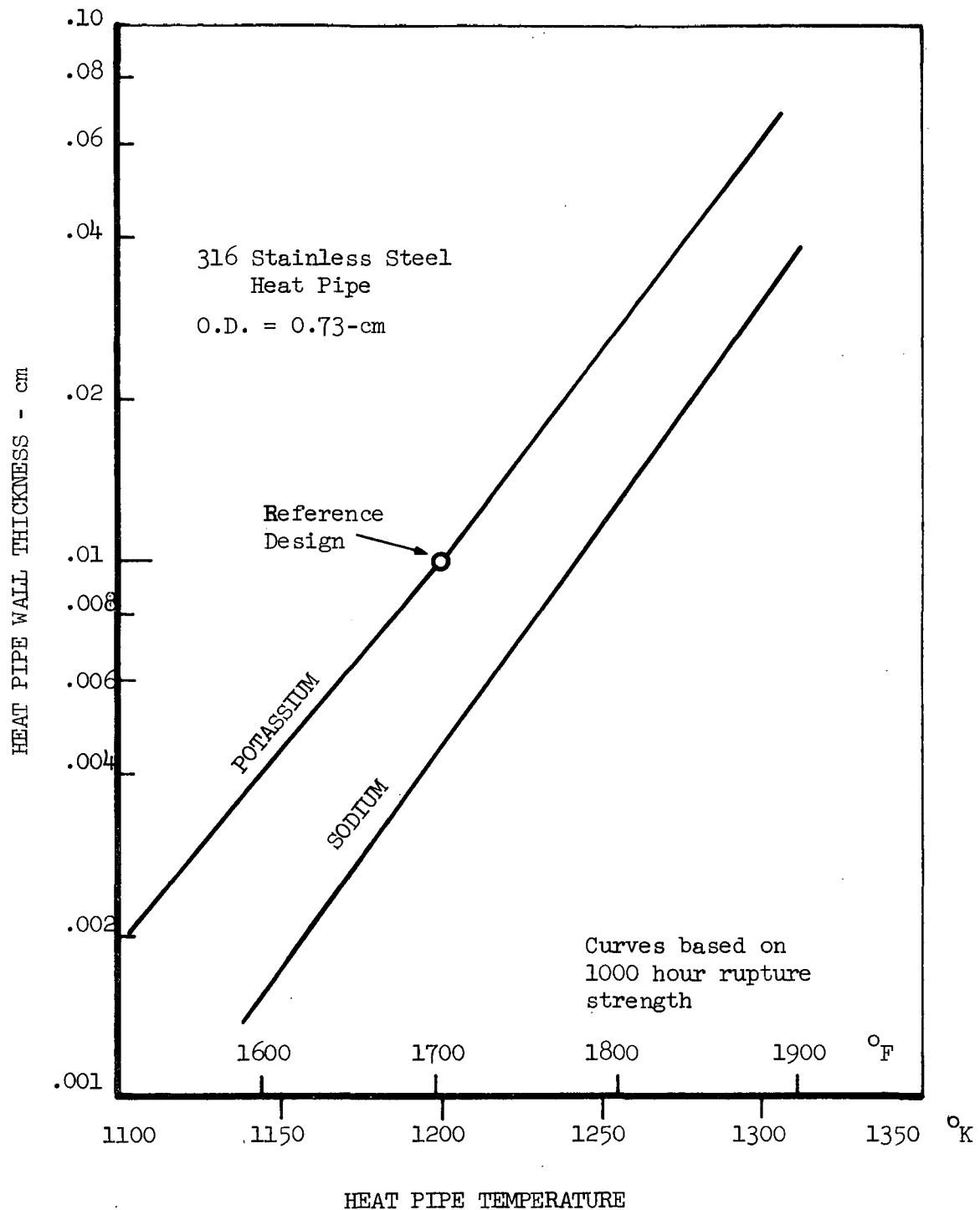
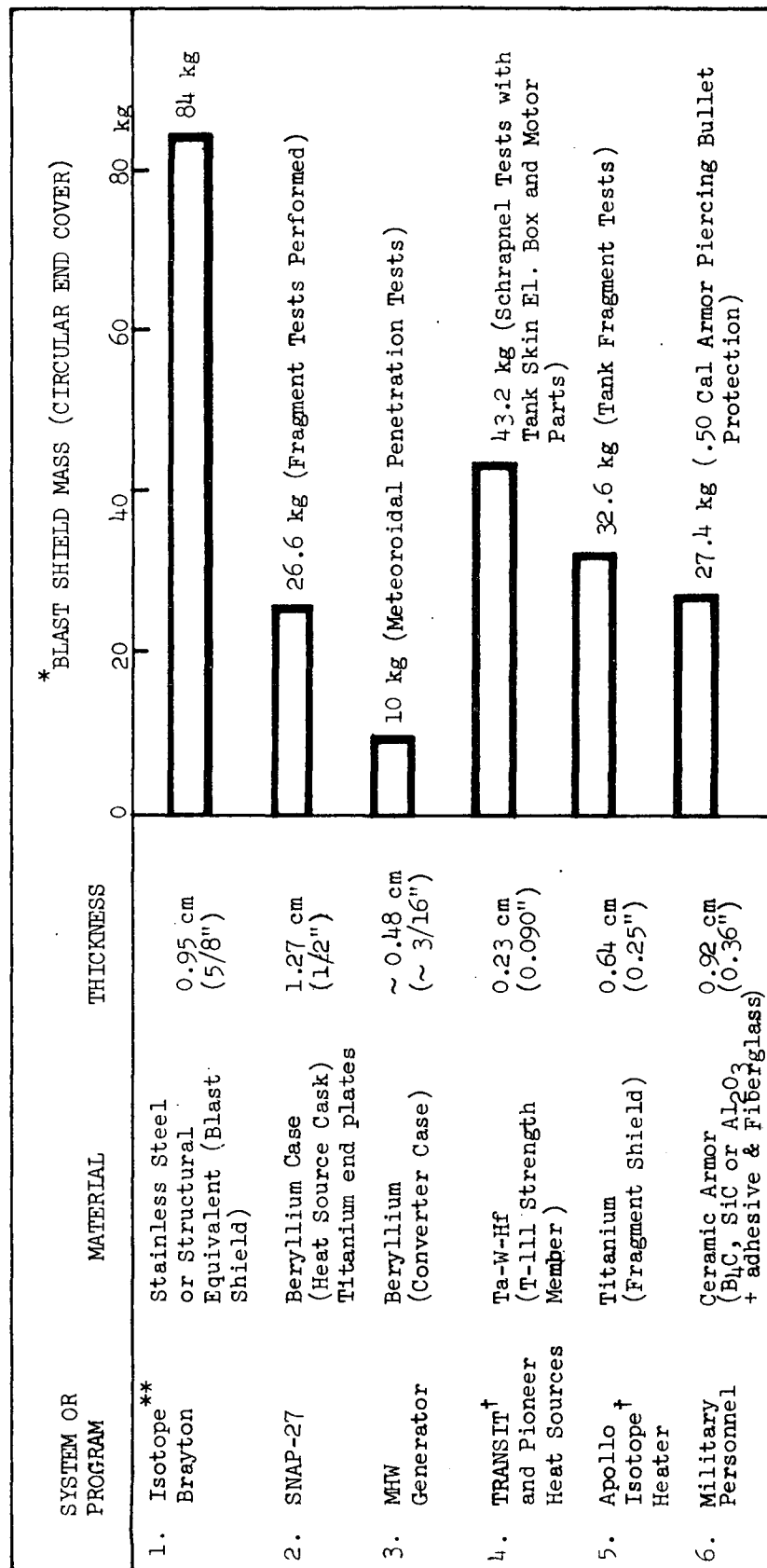


Fig. 6.8. Effect of heat pipe maximum operating temperature on wall thickness for 1000 hour rupture criteria

TABLE 6.8
COMPARISON OF VARIOUS BLAST SHIELD MATERIALS



* Mass based on a circular shield 120 cm in diameter which protects the aerodynamic flare, parachutes, auxiliary radiator and heat source. The mass of a cylindrical shield around the auxiliary radiator would be twice the mass of an end shield.

** Large radioisotope system, shield based on conceptual design considering the capsule, although they are neglected here.

† The TRANSIT and Apollo capsules also had other barriers surrounding the capsule, although they are neglected here.

The selected blast shield design for the radioisotope safety package is a cylindrical disc of titanium 0.64 cm thick which covers the flight system diameter and an annular shield of 0.13 cm which covers the aerodynamic flare. The annular shield will have a mass of 25.8 kg (neglecting structural mechanisms) and is jettisoned with the other safety equipment. The thicker 50.3 cm diameter section in the center has a 5.9 kg mass and will become a permanent part of the flight system.

It is important to note that intervening structure will also provide blast shielding. Hence, the preferred approach in designing for a blast environment is to interpose other mass between the critical components and explosive source. However, in the present case the blast shield mass is not excessive relative to the overall safety system mass of 450 kg, and improves integration flexibility.

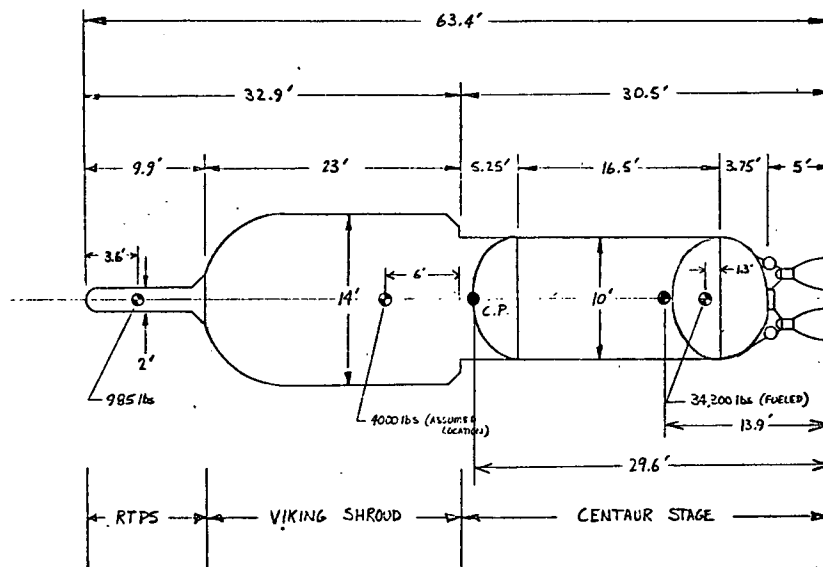
In addition to withstanding fragment impact, the blast shield will also be subjected to an overpressure pulse. This pressure is maximum during a launch pad explosion and decreases at higher altitudes. The computed stress in a solid disc of 60 cm radius subjected to a peak overpressure of 150 psi is sufficient to cause rupture. Consequently, the shield will require structural stiffening to survive the overpressure environment. Stiffening of the shield is also required to withstand the stresses generated by fragment impact.

6.3. REENTRY DESIGN ANALYSIS

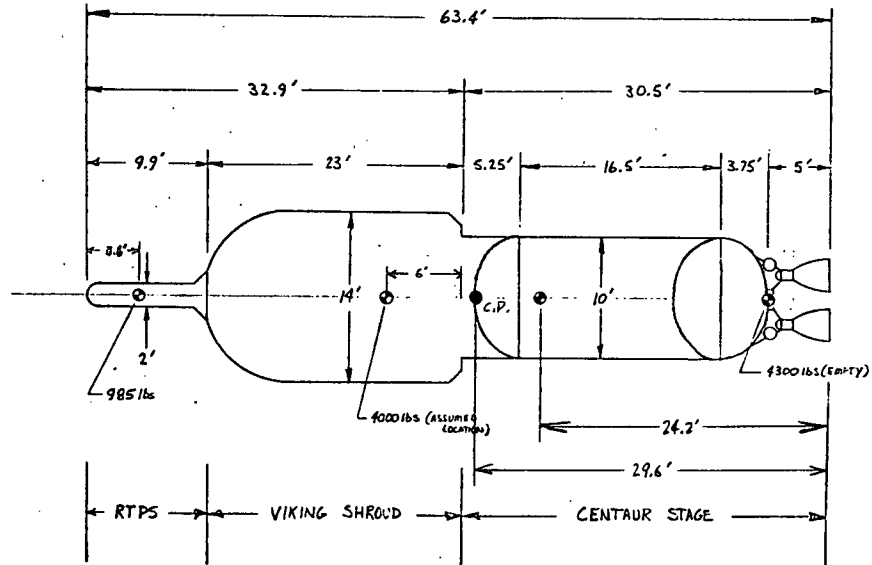
The RTPS is designed to assure intact reentry from all possible abort modes. Protection from reentry heating was established by analyses of vehicle aeroballistics and the resulting aerothermodynamics.

6.3.1. Aeroballistics

6.3.1.1. Abort Configurations. Four likely abort configurations were studied to determine their reentry aeroballistic characteristics. These are shown in Fig. 6.9. The arrangement of the RTPS relative to the payload is typical; the

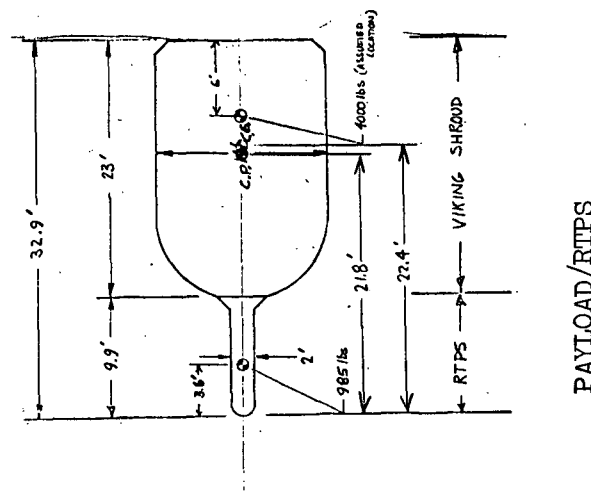


FUELED CENTAUR/PAYLOAD/RTPS



EMPTY CENTAUR/PAYLOAD/RTPS

Fig. 6.9. Probable abort configurations



RTPS

actual case may be somewhat more compact but will not affect the results. Three of these are malfunctions occurring near the time of Centaur ignition when suborbital conditions still exist. In the first case, a failure of the Centaur to initiate its chill-down sequence prior to ignition is assumed, resulting in the radioisotope thermionic power supply (RTPS), payload and fueled Centaur assembly reentering. In the second case, it is assumed that the chill-down sequence occurs on the Centaur; however, ignition does not occur and the propellants are drained leaving the same assembly as Case 1, but much lighter. The assumption in the third case is that separation of the payload from the Centaur occurs prior to Centaur ignition and the assembly of the payload and RTPS reenters. The final case is the RTPS reentering from earth orbit as a freebody.

For each configuration, the center of mass (c.g.) was determined assuming that the payload c.g. is a third of the axial length above the mounting interface. The preferred reentry attitude was determined by recalculating the center of pressure (c.p.) assuming a side-on attitude and Newtonian flow. For this calculation, the payload was approximated as a solid cylinder having a $C_D = 1.2$. Typical electric propulsion payloads have a density of 32 kg/m^3 (2 lb/ft^3) which would fill the available envelope space. The stability in the side-on attitude is shown in Table 6.9 expressed as $X_c/p./X_c.g.$ Both Case 1 and 2 will reenter with the Centaur engines forward. Case 3 will tumble and the RTPS as a freebody would be nose first stable.

The hypersonic ballistic coefficients were calculated for these configurations in their entry attitude based on Newtonian flow. Engine hardware would receive severe heating in Case 1 and 2, however, should remain stable to an altitude well below that of peak heating. Tumbling ballistic coefficient for Case 3 was determined by the integrated average for one revolution.

The range of these possible abort conditions were evaluated to assess the likelihood of occurrence. Both conditions 1 and 2 would be readily observed by the launch crew and a command destruct would be initiated. As a result, the Centaur stage would be stripped away leaving the configuration

TABLE 6.9
POSSIBLE ABORT CONDITIONS

| Configuration | Attitude | Side on X_{cp}/X_{cg} | Ballistic Coefficient | Failure Mode | Comments |
|------------------------------------|---------------------------|----------------------------|--------------------------------------|---|---------------------------------------|
| 1. Fueled Centaur/ payload/RTPS | Centaur engine forward | 2.13 | 415 psf (2028 kg/m ²) | Centaur pre-start sequence not begun | Requires command destruct decision |
| 2. Empty Centaur/ payload/RTPS | Centaur engine forward | 1.22 | 98 (479) | Centaur ignition failure | Requires command destruct decision |
| 3. Payload/RTPS | Tumbling | 1.03 | 21 (103) | Separation failure | Worst sidewall heating |
| 4. RTPS | Nose forward | > 1.20 | * | Normal reentry | Worst nose and flare heating |

* Ballistic coefficient varies with flare diameter with a range from about 10 to 60 psf. (50-300 kg/m²)

of either condition 3 or 4. (This assumes that simultaneous failures in separate systems don't occur; e.g., the command destruct system is functional.)

Condition 3 is less likely than condition 4, normal reentry, yet results in the worst sidewall heating due to the tumbling reentry attitude. For reentry at orbital and escape velocities, heating at high altitudes will cause burnup of the payload and, thus, the configuration 4 would result. Therefore, condition 3 was considered only for pre-orbital abort. Condition 4 was considered for the entire range of reentry possibilities: pre-orbital, orbital and at escape velocity.

The range of heating that can result from these conditions is discussed in Section 6.3.2. The worst case for interior temperatures is the orbital decay while high-angle reentry at escape velocity is worst for heating rates.

6.3.1.2. Aerodynamic Design. Aerodynamic behavior of the RTPS reentry configuration is primarily a function of the flare design, i.e., conic half-angle and base diameter. The smallest and lightest flare is one which has the largest half-angle for the maximum drag. Figure 6.10 gives the variation of hypersonic drag coefficient with flare angle measured on a model having nearly the same L/D as the RTPS. The maximum drag coefficient occurs at about a 45° half-angle which was chosen as the reference design.

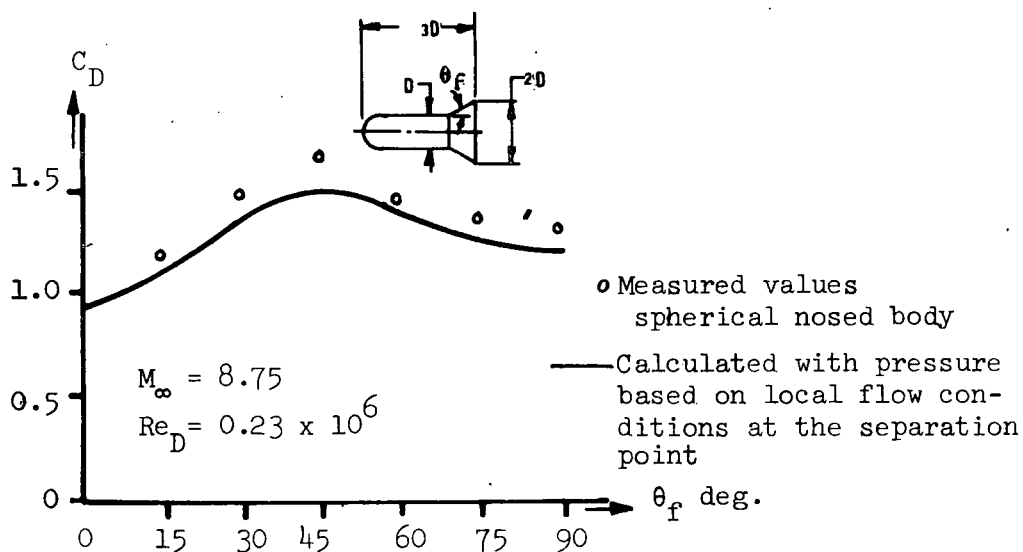


Fig. 6.10. Drag coefficient vs flare angle

The influence of variations in the diameter of the 45° half-angle flare on the RTPS aeroballistics was evaluated. Volume within the payload envelope allows for a substantial increase in the flare diameter above the 122 cm diameter baseline design. Benefits of a larger flare (shown in Fig. 6.11) are to reduce the ballistic coefficient of the configuration. These calculations assumed the unit weight of the flare is 8 kg/m². These results are based on a drag coefficient computed from the following relationship:

$$C_D = \frac{C_{DN} A_N + C_{DF} (\sin\phi) A_F}{A_B}$$

where,

C_{DN} = drag coefficient for the nose, which was taken as that for a sphere (1.0 for hypersonic conditions and 0.47 for subsonic conditions*),

A_N = projected or cross-sectional area of the nose (cylindrical section),

C_{DF} = drag coefficient for the flare, which was taken as that for a flat plate (1.69 for hypersonic conditions and 1.18 for subsonic conditions, Ref. 24) and multiplied by the SIN of the flare angle,

A_F = projected area of the conical flare,

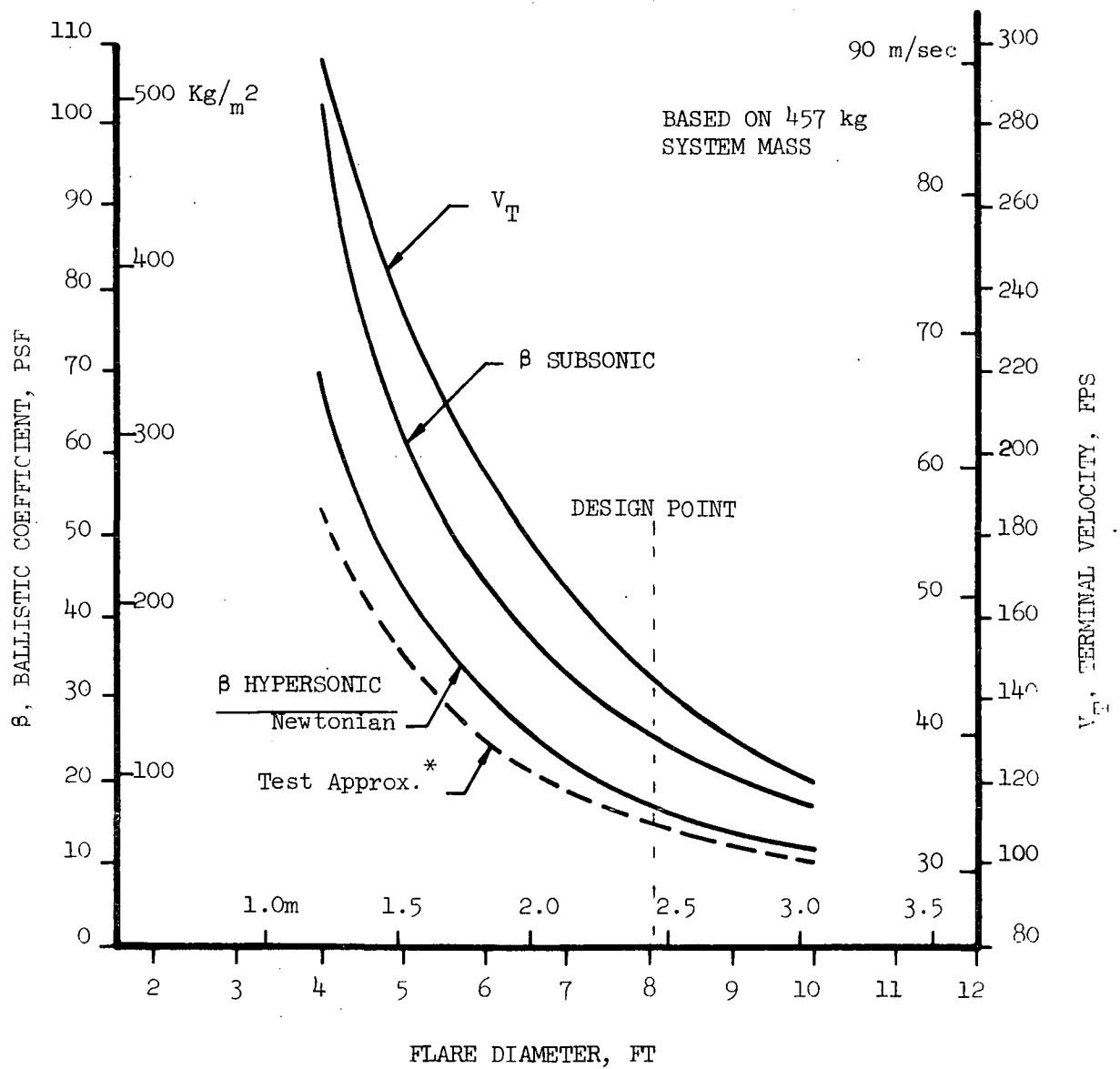
ϕ = flare angle taken as 45° ,

A_B = projected area of the flare base.

The design point diameter shown in Fig. 6.11 was selected since it results in ballistic coefficients below the knee of the curve and does not cause excessive weight.

The LiH radiation shield (discussed in Section 6.5) influences the aeroballistics because of added system mass and an increase in diameter of the cylindrical body. Figure 6.12 shows the effect of a safety system mass and diameter increase on subsonic and hypersonic drag coefficients for the case of constant flare diameter. The figure also shows the combined effect of

* This is approximately 25% lower than experimental results obtained on a similar geometry during Gun Tunnel Tests which were referenced in the last monthly report.



* Extrapolated from test data of similar shape at 4 ft flare (Ref. 15)

Fig. 6.11. Variation of aeroballistic parameters with flare size

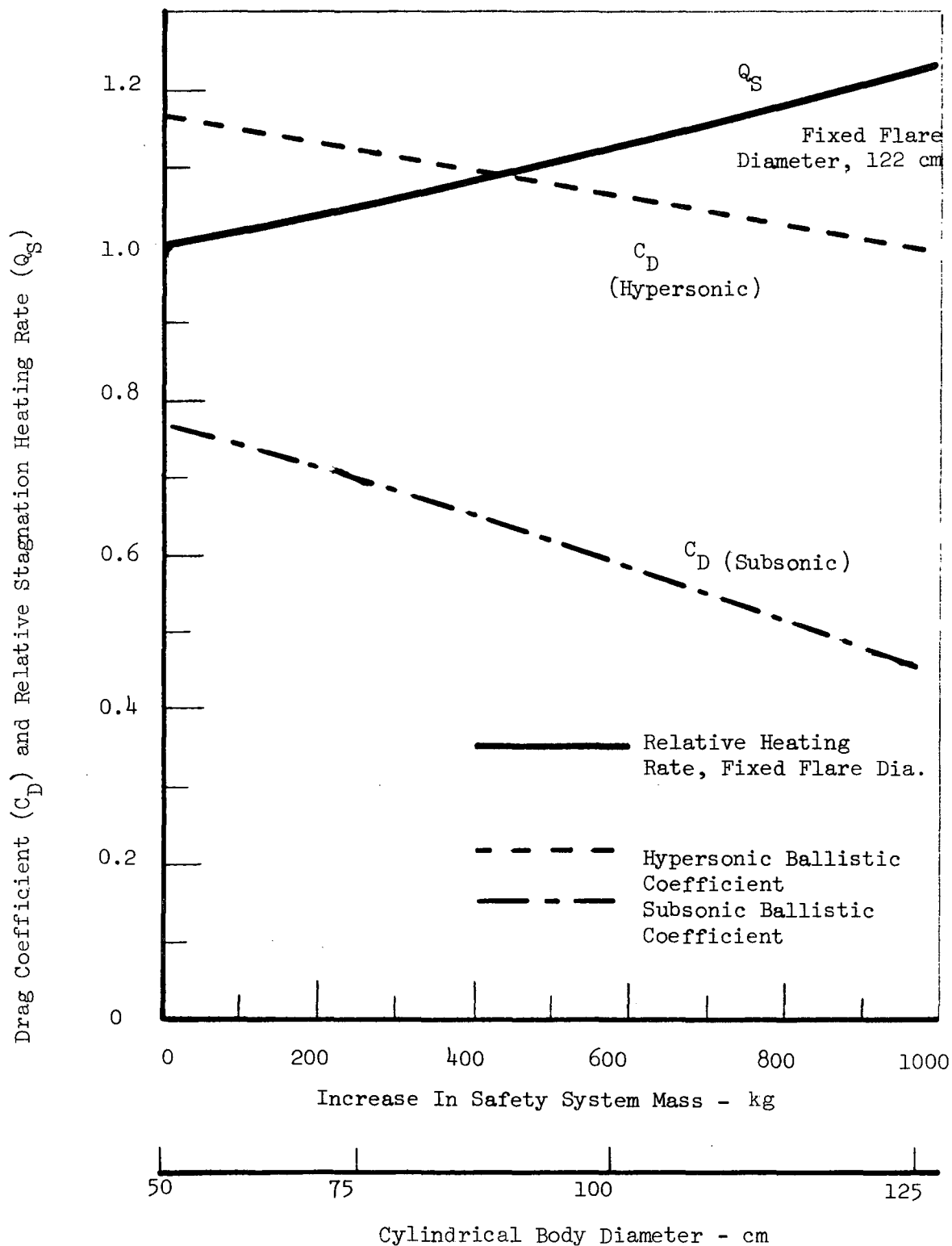


Fig. 6.12. Drag coefficient and heating rate changes with increases in safety system mass and diameter

C_D and ballistic coefficient changes on stagnation point aerodynamic heating during reentry, based on the following proportionality:

$$Q_S \propto \sqrt{\beta/D_N}$$

where Q_S = aerodynamic heating rate

β = hypersonic ballistic coefficient ($W/C_D A$) and

D_N = diameter of the nose (or cylindrical structure).

Since the peak reentry heating varies with the square root of the hypersonic ballistic coefficient, a doubling of the diameter will reduce heating by nearly 50 percent. A similar reduction in the terminal velocity also results since it varies as the square root of the subsonic ballistic coefficient.

6.3.1.3. Reentry Trajectories. Overall dimensions of the reentry vehicle which provides safe, intact protection of the RTPS is shown in Fig. 6.13. The resulting reference design vehicle has a mass of 475 kg and a hypersonic ballistic coefficient of 85.5 kg/m^2 . A range of reentry trajectories were investigated for this design. Reentry trajectories for the reference mission were supplied by the NASA/OART Mission Analysis Division. These were based on a hypersonic drag coefficient of 1.2 and were calculated for a 90° launch azimuth and initial flight path angles from -10° to -90° with an initial velocity of 11 km/sec. Reentry from a low earth orbit was also considered. Figure 6.14 shows the superorbital reentry profiles. This range of trajectories covers all possible abort modes.

A second set of trajectory cases was studied for a reentry vehicle of the same configuration but having a 200 kg mass increase. The resulting hypersonic ballistic coefficient for this heavier vehicle is 122 kg/m^2 ; however, it could be lowered to the original value by increasing the flare diameter to less than 3 meters.

6.3.2. Aerothermodynamics

6.3.2.1. Aerodynamic Heating. Calculations of aerodynamic heating to the sphere-cylinder-flare reentry configuration was accomplished simultaneously

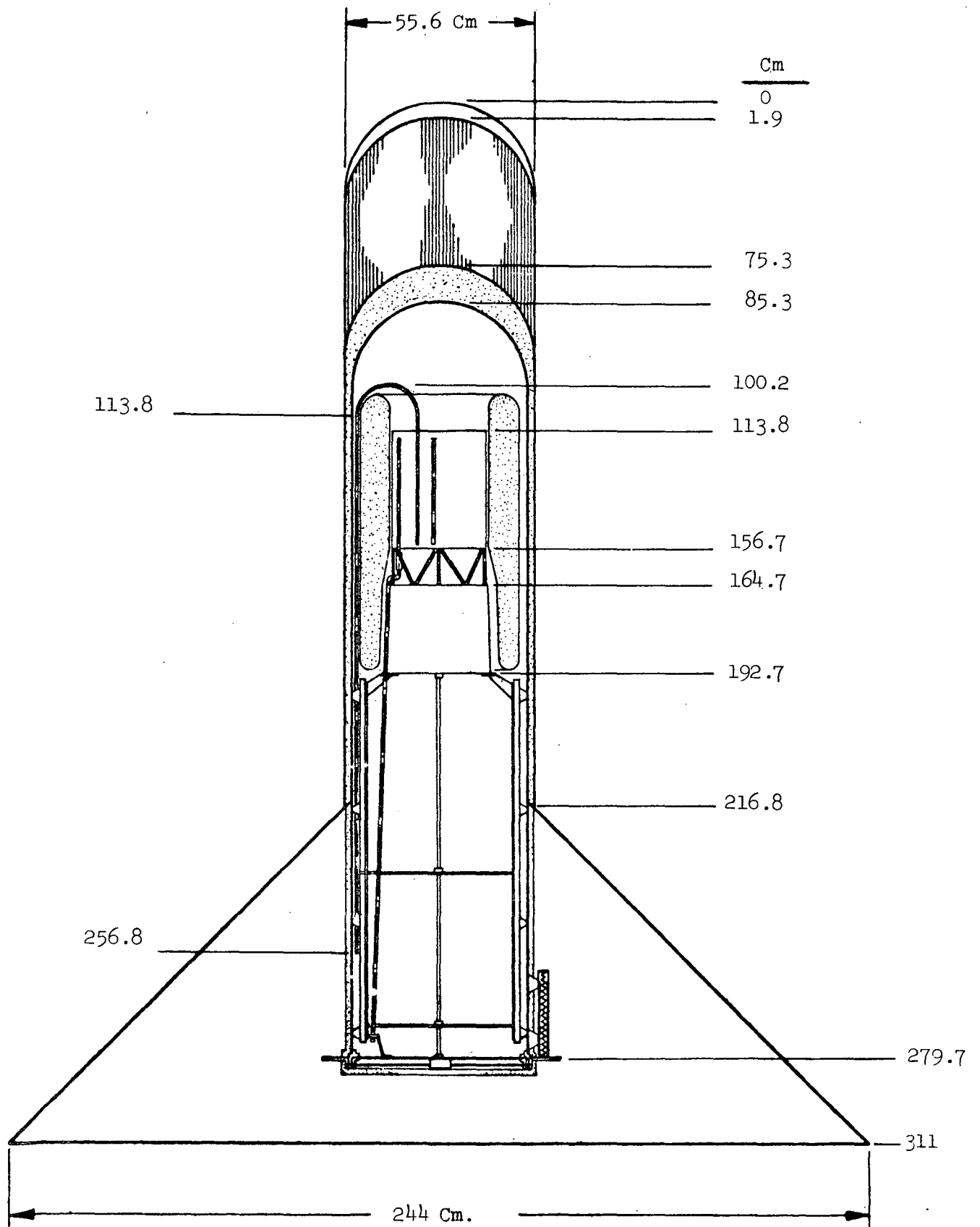


Fig. 6.13. Overall dimensions of reentry vehicle

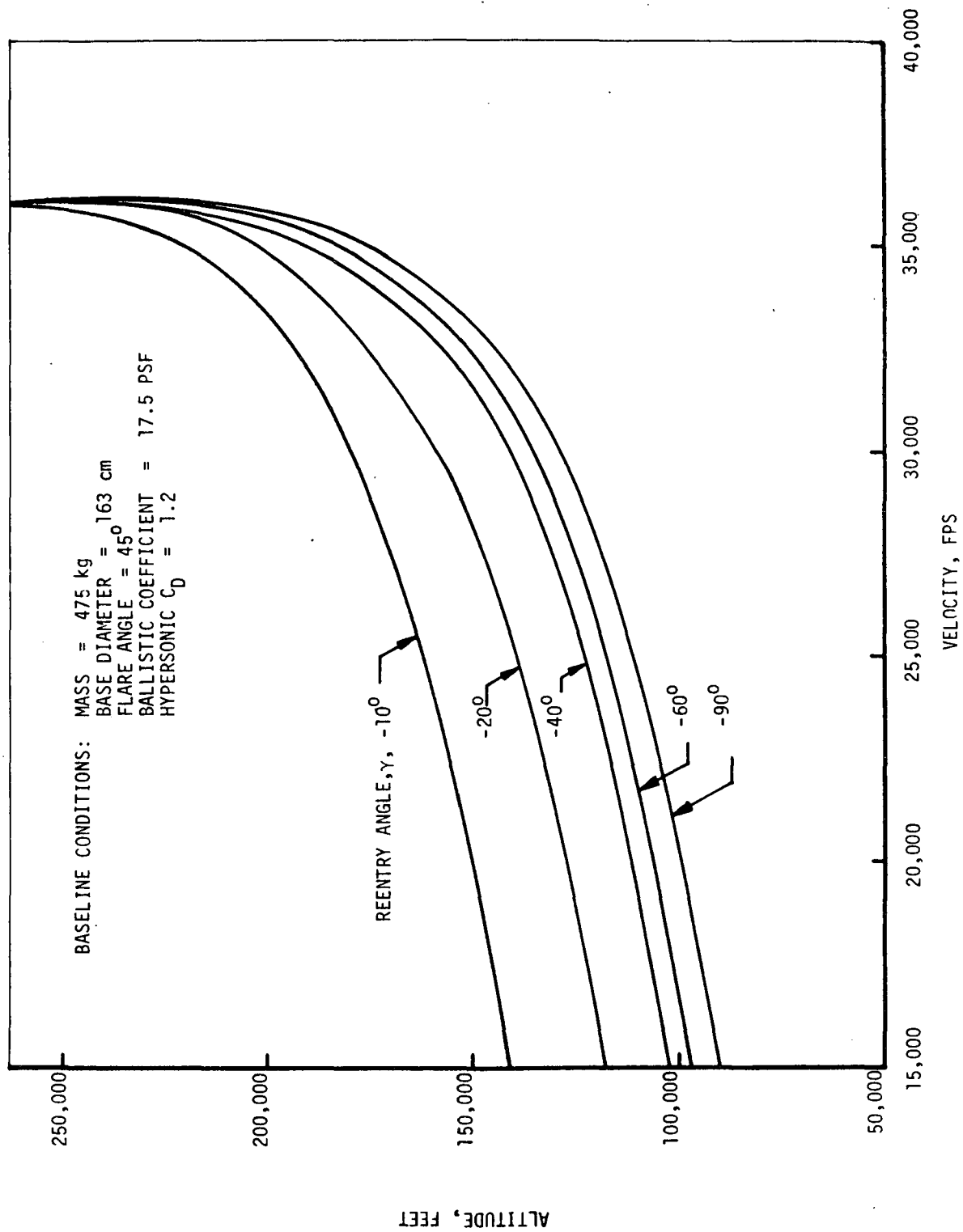


Fig. 6.14. Reentry trajectory profiles

with calculation of structural temperatures using a generalized computer program (Ref. 26). In this program aerodynamic heating is calculated by means of the "reference enthalpy method" of Eckert and others. The reference enthalpy method is generally advantageous in that aerodynamic heating rates can be accurately predicted over a broad range of flight conditions. This holds true for many cases in which high-temperature gaseous dissociation and ionization occur in the boundary layer. By evaluating the properties of air at a "reference enthalpy" defined as

$$EN^* = EN_f + 0.5 (EN_W - EN_f) + 0.22 (EN_r - EN_f)$$

where: EN^* = reference enthalpy
 EN_f = local flow enthalpy
 EN_W = wall enthalpy
 EN_r = recovery enthalpy

it is possible to employ incompressible flow relationships in formulating heat transfer coefficients. Heat transfer is calculated for geometries approximating flat plates, wedges, cones, spheres, or cylinders. All flight velocities can be accommodated for any altitude at which the atmosphere can be considered a continuum.

Heat transfer to the stagnation point of a sphere is calculated by the methods of Refs. 27 and 28 and incorporates a modified Detra-Kemp-Riddell expression:

$$Q_i = 1.9 \times 10^{-6} \left(\frac{p_\infty}{t_\infty d} \right)^{.5} (U_\infty)^{3.15} \left(\frac{EN_t - EN_i}{EN_t - EN_\infty} \right)$$

where: Q_i = heat flux, B/ft²hr
 ρ_∞ = freestream density, lb/ft³
 t_∞ = freestream temperature, °F
 V_∞ = freestream velocity, fps

Heat transfer coefficients for idealized flat plate geometries (flat plate, wedge, and cone) are formulated on the basis of applicable flow field parameters, and properties are evaluated at so-called "reference" conditions, as noted earlier. For laminar flow, the Blasius solution of the boundary-layer momentum equation and the modified Reynolds-analogy are used to obtain the Stanton number. The local heat transfer coefficient is then expressed as

$$h_L = 3.42 \times 10^{-2} \left(\frac{P_f U_f}{\ell} \right)^{0.5} \left(\frac{\rho^* \mu^*}{\rho_b \mu_b} \right)^{0.5}$$

where: h_L = laminar heat transfer coefficient, lb/hr-ft²
 P_f = local flow pressure lb/ft²
 U_f = local flow velocity, fps
 ℓ = Reynolds number length, ft
 $\rho^* \mu^*$ = "Reference" density and viscosity
 $\rho_b \mu_b$ = base value density and viscosity

For turbulent flow, the modified Reynolds-analogy relating the Stanton number to the skin-friction coefficient, and the Blasius local skin friction coefficient are used to develop the heat transfer coefficient for use at Reynolds numbers of less than 10^7 .

$$h_T = 4.83 \times 10^{-3} \frac{(P_f U_f)^{0.8}}{\ell^{0.2}} \left(\frac{\rho^* \mu^*}{\rho_b \mu_b} \right)^{0.8} \left(\frac{\mu^*}{\mu_b} \right)^{-0.6}$$

At Reynolds numbers beyond 10^7 , the Von Karman local skin-friction coefficient is used and results in

$$h_T = 1.88 \times 10^{-3} \frac{(P_f U_f)^{0.8691}}{\ell^{0.1309}} \left(\frac{\rho^* \mu^*}{\rho_b \mu_b} \right)^{0.8691} \left(\frac{\mu^*}{\mu_b} \right)^{-0.7328}$$

The determination of wedge and cone aerodynamic heating assumes a constant Prandtl number of 0.65. An extended relationship of enthalpy to air temperature is incorporated into the program, taking into consideration the effects of dissociation. The program utilizes the U. S. Standard Atmospheric Properties.

Transition from laminar to turbulent flow was based on a local Reynolds Number of 10^6 . For these velocities, transition typically occurs between 250K to 300K feet (100 km) altitude.

Transient aerodynamic heating was calculated for each trajectory at four locations on the vehicle: 1) stagnation point; 2) cylinder at 110 cm; 3) cylinder at 180 cm; and 4) flare at 300 cm. Results of these calculations to a cold wall are shown in Fig. 6.15 for two extremes, the short high heat pulse which occurs during a -90° reentry and the longer heat pulse occurring during a -10° reentry. Table 6.10 gives the maximum heating rates and total heating with the corresponding trajectory times (from 120 km altitude) and altitudes for each of the locations and trajectories of the reference design. Variation of maximum heating with reentry angle is shown in Fig. 6.16.

6.3.2.2. Shock Layer Radiation. Another contribution to heating during reentry is by radiation from the high temperature gas residing in the shock layer. This is generally restricted to the stagnation region since the magnitude falls off rapidly away from the stagnation point. It has been shown that non-equilibrium radiative heating effects are small and equilibrium radiative heating dominates (Fig. 6.17 from Ref. 29). In the velocity range of 28 k fps to 38 k fps the formula is:

$$q_R = 8.16 \times 10^{-5} R_N \left(\frac{\rho_\infty}{\rho_0} \right)^{1.41} \left(\frac{V_\infty}{10^{-4}} \right)^{20}$$

where, ρ_∞ and V_∞ are free stream density and velocity (fps) respectively and R_N is the nose radius (ft).

This assumes an optically thin shock layer and shock layer thickness of $0.045 R_N$ for a hemispherical nose body. These are conservative assumptions

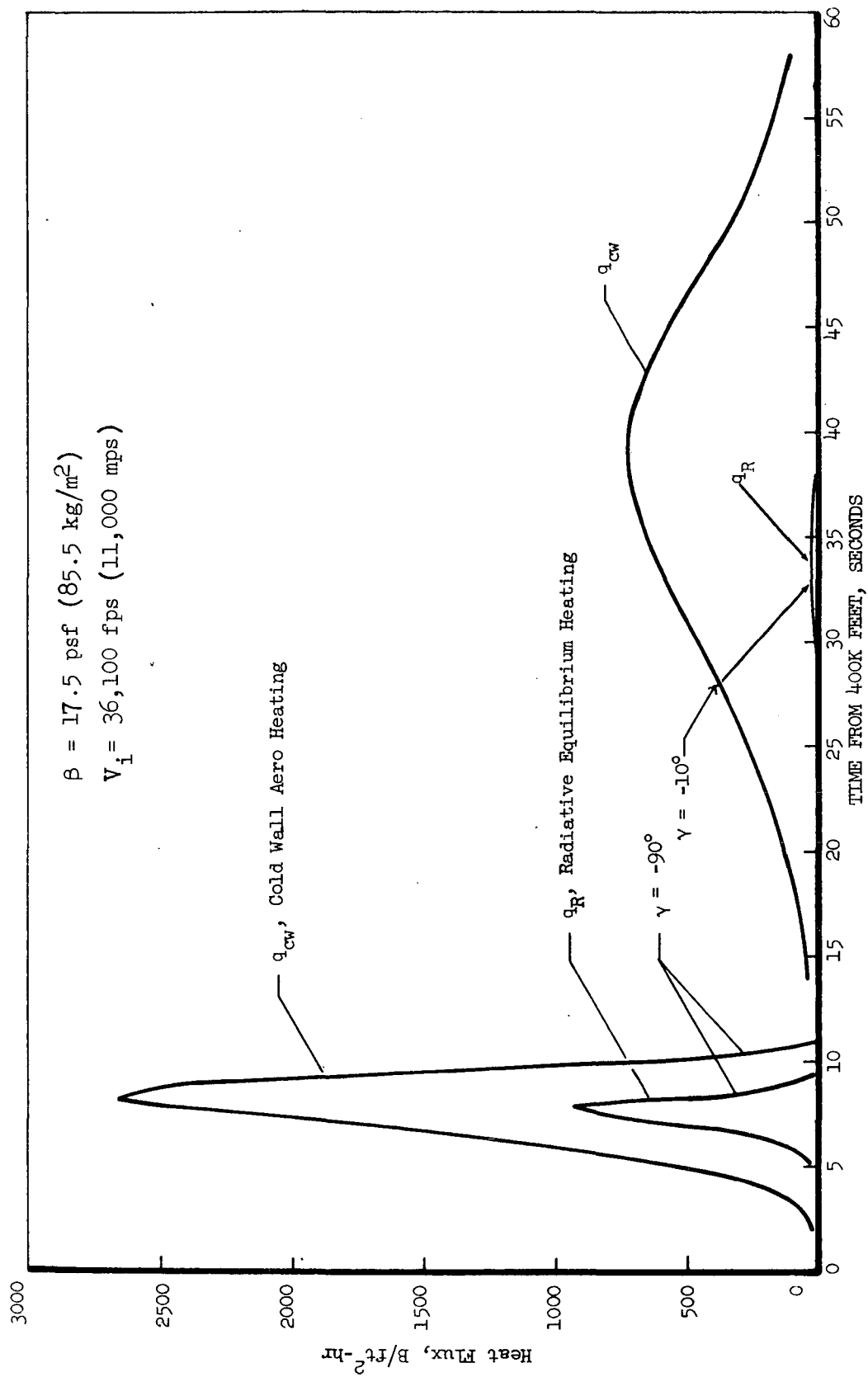


Fig. 6.15. Comparison of reentry heating at stagnation point

TABLE 6.10

MAXIMUM REENTRY HEATING SUMMARY

 $\beta = 17.5 \text{ psf } (85.5 \text{ kg/m}^2)$

| Location | Condition | $\gamma = -90^\circ$ | -60° | -40° | -20° | -10° | 0° |
|--|--|----------------------|-------------|-------------|-------------|-------------|-----------|
| Stag. Point | $q_{\text{Aero, Max, B/ft}^2 \text{ sec}^*}$ | 1,380 | 1,220 | 1,056 | 830 | 574 | 76 |
| | $q_{\text{Rad, Max, B/ft}^2 \text{ sec}}$ | 750 | 656 | 89 | 43 | 15 | 0 |
| | Time, Sec | 7.75 | 8.5 | 11.75 | 20 | 37.25 | 940 |
| | Altitude, Ft. | 131,300 | 141,500 | 136,000 | 163,000 | 192,300 | 219,700 |
| Sidewall @ 110 cm | $Q_{\text{Total, B/ft}^2 \text{ sec}^*}$ | 3,872 | 3,701 | 3,881 | 4,881 | 6,166 | 4,908 |
| | Time, Sec. | 9.5 | 10.25 | 14 | 25 | 49.25 | 964 |
| | Altitude, Ft. | 95,460 | 104,000 | 104,600 | 123,800 | 148,900 | 199,500 |
| | $q_{\text{Aero, Max Time}}$ | 45.8 | 35.7 | 30 | 10.5 | 7 | 1.36 |
| Sidewall @ 180 cm | Altitude | 108,400 | 113,700 | 121,800 | 152,900 | 180,000 | 199,500 |
| | $Q_{\text{Total Time}}$ | 119 | 90 | 101 | 87 | 39 | Cooling |
| | Altitude | 10,75 | 11.25 | 16.25 | 29.5 | 54.5 | |
| | $q_{\text{Aero, Max Time}}$ | 79,810 | 89,580 | 89,150 | 106,300 | 136,900 | |
| Flare @ 300 cm | Altitude | 40.3 | 31.4 | 26.5 | 15 | 5 | 1.0 |
| | $Q_{\text{Total Time}}$ | 8.75 | 9.5 | 12.5 | 22 | 40 | 964 |
| | Altitude | 108,400 | 118,200 | 121,800 | 145,000 | 180,000 | 199,500 |
| | $q_{\text{Aero, Max Time}}$ | 102 | 77 | 85 | 71 | 42 | Cooling |
| Flare @ 300 cm | Altitude | 10,75 | 12 | 16 | 28.75 | 58 | |
| | $Q_{\text{Total Time}}$ | 79,810 | 84,000 | 90,200 | 108,100 | 130,800 | |
| | $q_{\text{Aero, Max Time}}$ | 2,533 | 2,027 | 1,713 | 1,014 | 576 | 10 |
| | Altitude | 8.25 | 9 | 11.5 | 20 | 38.5 | 940 |
| * 1 Btu/ft ² -sec = 1.135(10) ⁴ watts/meter ² 1 Btu/ft ² = 1.135(10) ⁴ joules/meter ² | $Q_{\text{Total Time}}$ | 120,000 | 128,900 | 141,000 | 163,000 | 186,800 | 219,700 |
| | Altitude | 3,842 | 3,483 | 3,718 | 3,919 | 3,893 | 1,092 |
| | $Q_{\text{Total Time}}$ | 9.5 | 10.5 | 14 | 24.5 | 47.5 | 980 |
| | Altitude | 95,460 | 99,230 | 104,600 | 126,900 | 153,700 | 183,600 |

* 1 Btu/ft²-sec = 1.135(10)⁴ watts/meter²1 Btu/ft² = 1.135(10)⁴ joules/meter²

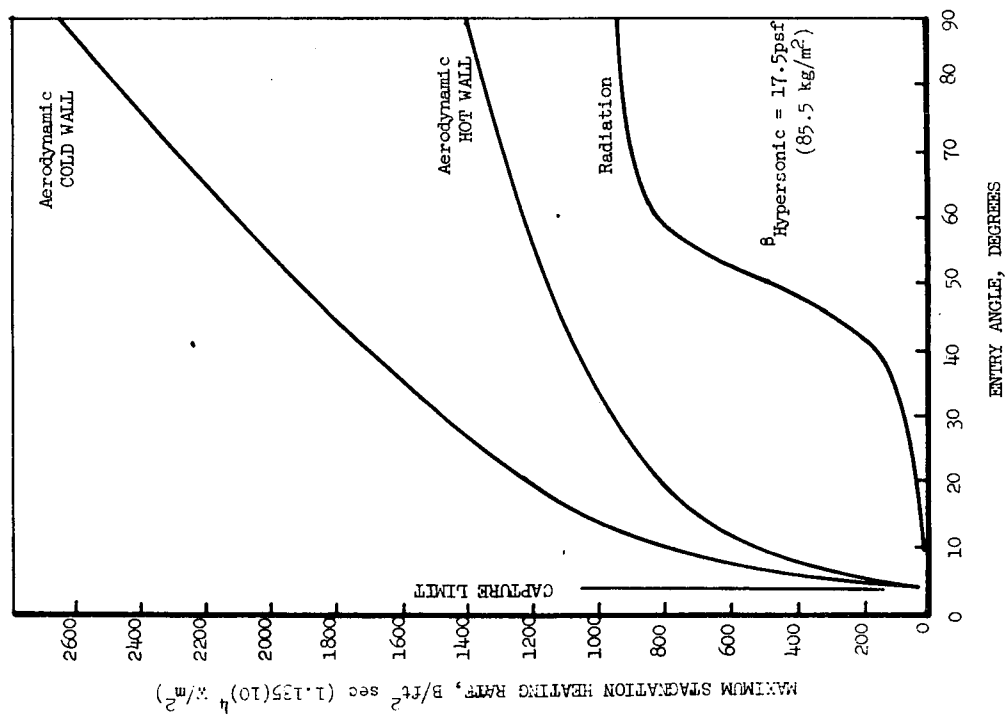


Fig. 6.16. Variation of maximum stagnation heating with entry angle at escape velocity

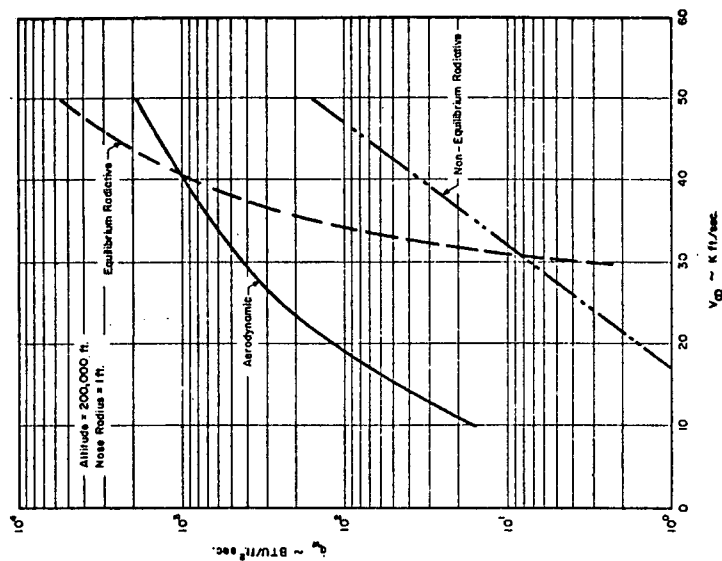


Fig. 6.17. Comparison of magnitude of Aerodynamic and radiative heating for a reentry vehicle at 200,000 feet

since, at extreme reentry velocities, effects due to both energy loss by radiation and self absorption may be significant and are not included. Thus, the radiative heating becomes more severe for steep reentry angles with the attendant high velocity at low altitudes.

Figure 6.15 shows a comparison of heating during reentry for the $\gamma = -90^\circ$ and -10° trajectories. The peak radiative heating is about one-third the cold-wall heat flux for the steep reentry. It is about 3% of the cold wall peak heating for the shallow reentry. Other comparisons are shown in Table 6.10 and Fig. 6.16.

6.3.2.3. Separated Flow Heating. Another region of increased heating on the reentry vehicle is on the flare aft of the body juncture. It has been demonstrated (Ref. 30) that boundary layer separation occurs on wedge angles greater than 30 degrees. This condition is illustrated in Fig. 6.18. The flow reattaches at some point on the flare with a resulting local thinning of the boundary layer and a corresponding increase in aerodynamic heating. Figure 6.19 shows the effect of separated flow on heating. This local heating increases with both Mach number and Reynolds number, and can result in heating factors of up to 3 times that of the unseparated flow.

Separated flow heating is difficult to predict since the reattachment location is transient as a result of flow property dependence. This heating affect was not included in the present study and needs to be defined empirically for a specific configuration. The zone of increased heating should be confined to a rather small region just aft of the body-flare juncture. A localized increase in thermal protection will be necessary in this region. The affect on total vehicle mass should be small.

6.3.3. Thermal Protection System

6.3.3.1. Heat Shield Selection. High reentry heating rates encountered dictate a thermal protection system having minimum ablation yet having the capability of insulating the underlying material. Graphite and carbon-graphite composites afford excellent ablation characteristics.

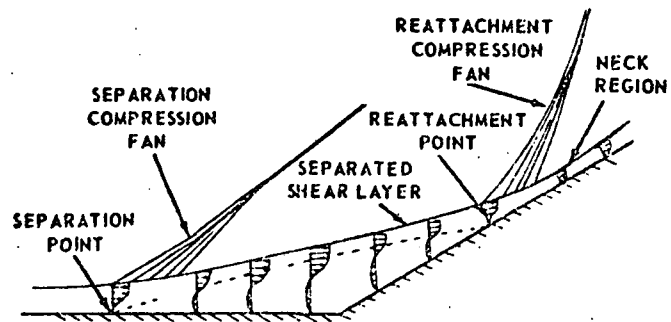


Fig. 6.18. Wedge induced separated flows

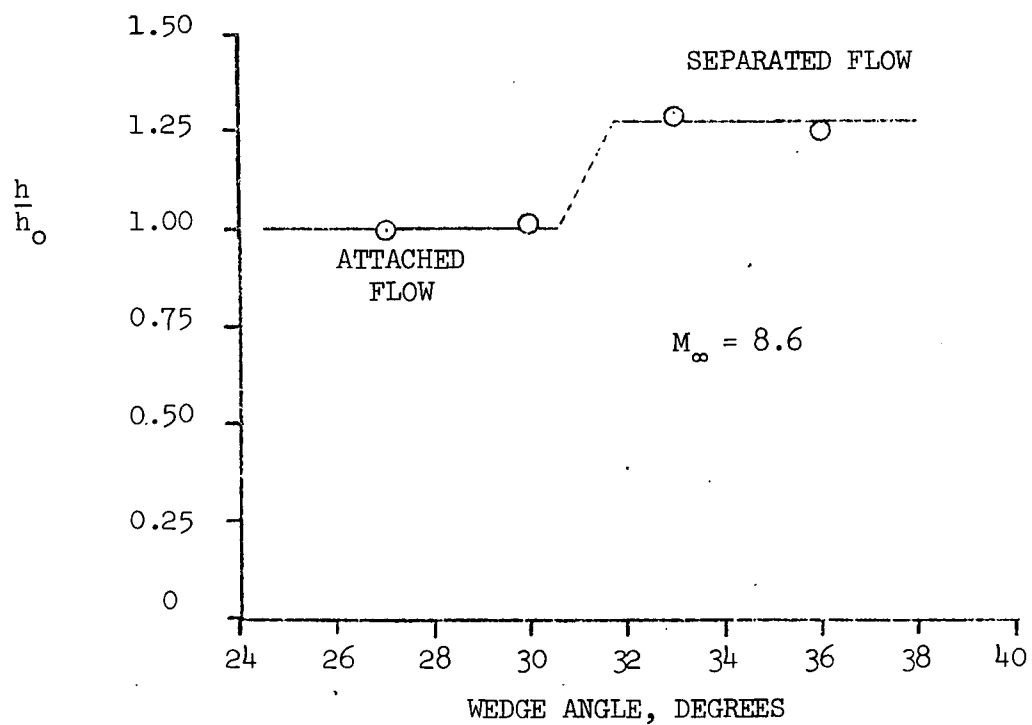


Fig. 6.19. Effect of separated flow on heating

Carbon/Graphite Fibrous Composites. A great deal of effort is being expended in the development of carbon/graphite fibrous composites. This work is being done to obtain higher strength graphitic material, and, hopefully, by the very nature of their construction, minimize catastrophic failures as observed in the past for the bulk, polycrystalline graphites. Table 6.11 summarizes the status and types of construction of several current, carbon/graphite fibrous composites. A comparison of properties available for several of these carbon/graphite composites and those of AXF-5Q and ATJ-S (bulk graphite materials) are presented in Table 6.12.

The overall properties of 2D laminates, such as Pyro-Carb 406 used on the Graphite Lunar Module Fuel Capsule (GLFC), offer significant advantages over the bulk graphites. Depending on direction, the tensile strength of Pyro-Carb 406 is greater than the bulk graphites. A comparison of the thermal expansion shows an advantage of the Pyro-Carb 406 over the bulk graphites at room and slightly elevated temperatures. This advantage persists at 2500-3000°K where the Pyro-Carb 406's thermal expansion is equivalent to ATS-S and about half that of AXF-5Q. Similarly, the thermal conductivity of Pyro Carb 406 in the 1900-3000°K range is about half that of ATS-S and about 20% lower than AXF-5Q.

Bulk Graphites. Bulk, polycrystalline graphites AXF-5Q and ATJ-S were considered for this selection due to the availability of materials with sufficient property data reported in the literature. AXF-5Q and ATJ-S are bulk graphites which have been previously used in reentry shields.

Selection. From the comparison of the properties given in Table 6.12 (from Ref. 31), Pyro-Carb 406 was selected as the ablator due to its extensive development for SNAP-27 and because it has a relatively low thermal conductivity in the radial direction.

Zirconia felt was selected as the high temperature insulating material underlying the Pyro-Carb heat shield. This is the same insulator used to protect the LiH radiation shield/heat pipes from fire effects as discussed in Section 6.1.

TABLE 6.11
Carbon/Graphite Fibrous Composites

| <u>Organization</u> | <u>Type of Construction</u> | <u>Remarks</u> |
|--|--|--|
| AVCO | This is a 3D, orthogonal construction using moderate and high strength materials such as VYB70-1/2, WYB, the Thornels, and the English Morganite fibers. After the block or cylinder sock is made, an impregnant, which can either be phenolic, furfuryl alcohol, coal tar pitch, or chemical vapor deposition (CVD), is used as the binder. Densities of about 1.60-1.70 gm/cc are obtained. | This material system is not fully characterized because a complete production process or the type of fibers that will be employed have not been settled on. Almost all of the data available are room temperature properties. In addition, a cylinder produced by this method may cost several ten-fold that of bulk graphite. |
| Hitco/General Electric | Pyro-Carb 406, produced by Hitco, was used for the Graphite Lunar Module Fuel Capsule (GLFC). The material is composed of "graphitized", square-weave rayon cloth (99.5% carbon) which is impregnated with a phenyl aldehyde and a graphite particle filled resin (USP-39) having a 33% resin and 45 to 50% char yield. This impregnated cloth is layed-up, molded and cured under pressure, and heated in stages to an ultimate temperature of 4000°F for 3 hours. The product is then machined to shape and exposed for 300 hours at 2000°F to an atmosphere containing methane at reduced pressure to impregnate the composite with pyrolytic carbon. | Data were obtained in a test program on specimens obtained from plate material and the tag-end of cylinders. Thus the data may not be considered as design data. In addition, some of the elevated temperature mechanical property data may not be of sufficient accuracy to use for design. The modulus of elasticity data presented are not initial moduli, which most designers used for thermal stress analyses but are termed "Engineering Elastic Moduli". Their slope is significantly less than the initial slope. |
| General Electric | The construction is termed "omniweave" and has interlocking fibers in each of three directions. | A consideration of this material's utility should be its response when loads are applied. The question that must be answered is how the fibers, which are "crimped" due to the interlocking construction, react with relatively low strength binder material as the fibers tend to straighten. |
| McDonnell Douglas/Monsanto | A number of different types of construction have been investigated. The primary candidate has fibers laid up at 90° to each other interlocked by a third fiber woven diagonally and interlocking along the longitudinal axis. | A number of problems have been encountered in producing woven goods (socks) such as frusta and cylinders. Up until a year ago the weaving development had not been completed and difficulties were encountered during impregnation and curing of flat goods to produce a uniform composite. |
| Sandia/Supertemp and Sandia/Fiber Technology | This is a reinforced pyrolytic graphite felt material system. This material is produced by taking a low density (0.1 gm/cc) carbon felt, manufactured by the Carbone Corporation as Grade RVC, and infiltrating this material with pyrolytic carbon to obtain densities ranging from 0.15 to 1.8 gm/cc. The properties obtained are a direct function of the density. | Sandia has generated a considerable amount of data as a function of density and heat treatment temperature. However, the material is still under development and is being evaluated as full-scale hardware. |

TABLE 6.12

COMPARISON OF PROPERTIES OF CARBON/GRAPHITE FIBER COMPOSITES AND BULK GRAPHITE

| Property | Material | | | | |
|--|---|--|---|---|---|
| | AVCO/Thornei 3D Reinforced Graphite ⁽⁶⁾ | Pyro-Carb 406 ⁽⁷⁾ | Super-Temp RPG ⁽⁶⁾ | Poco AXF-5Q ⁽⁸⁾ | ATJ-S ⁽⁸⁾ |
| Density (gm/cc) | 1.60 | 1.44 | 1.75 | 1.80 min. | 1.80 min. |
| Tensile Strength- Room Temperature (10 ³ psi) | X-Y 15.0 - 19.0 Z 7.5 - 10.0 | Axial 12.5 Circumferential 5.0 Radial 0.84 | X-Y 5.0 - 7.0 Z 1.8 - 2.3 | 7.0 | With grain 3.3 Across grain 3.2 |
| Strain to Failure- Room Temperature (10 ⁶ psi) | 0.33 | Circumferential 0.29 | 0.18 | 0.7 | With grain 0.28 Across grain 0.48 |
| Tensile Modulus- Room Temperature (10 ⁶ psi) | X-Y 4.6 - 4.9 Z 2.4 - 2.6 | Axial 2.75 Circumferential 1.75 Radial 0.84 | X-Y 2.7 - 3.2 Z 1.25 - 1.42 | 2.1 | With grain 1.9 Across grain 1.3 |
| Compressive Strength- Room Temperature (10 ³ psi) | X-Y 14.0 - 18.5 Z (n/a) | Axial 14 Circumferential 7.5 Radial 17.1 | X-Y 11.5 - 12.5 Z 40.0 | 19.6 | With grain 7.42 Across grain 8.96 |
| Compressive Modulus- Room Temperature (10 ⁶ psi) | X-Y 4.7 - 5.0 Z 2.5 - 2.8 | Axial 2.75 Circumferential 1.75 Radial 0.56 | X-Y 1.78 - 2.50 Z 2.00 - 2.85 | 1.75 | With grain 1.50 Across grain 1.00 |
| Shear Strength- Room Temperature (10 ³ psi) | 3.2 | 2.3 | 1.5 | -- | -- |
| Poisson's Ratio- Room Temperature | μ_{xy} 0.10 μ_{yz} 0.10 μ_{zx} 0.08 | $\mu_{\theta r}$ 0.24 $\mu_{\theta \theta}$ 0.156 $\mu_{\theta z}$ 0.1 $\mu_{\theta \theta}$ 0.064 $\mu_{\theta r}$ 0.2 $\mu_{\theta z}$ 0.069 | μ_{xy} 0.21 μ_{xz} 0.20 μ_{zx} 0.19 | .39 | $\mu_{\theta \theta}$ 0.12 $\mu_{\theta a}$ 0.06 $\mu_{\theta w}$ 0.14 |
| Coefficient of Thermal Expansion (10 ⁻⁶ in/in-°F) | 0.8 above 600°F | 500°F Axial & Circum 0.23 Radial 0.93 1000°F Axial & Circum 0.75 Radial 1.72 2000°F Axial & Circum 1.04 Radial 2.18 3000°F Axial & Circum 1.64 Radial 2.63 4000°F Axial & Circum 1.96 Radial 2.85 5000°F Axial & Circum 2.23 Radial 3.14 6000°F Axial & Circum 2.36 Radial 3.41 | X-Y 2.0 - 2.7 | 500°F 3.9 1000°F 4.15 2000°F 4.6 3000°F 4.95 4000°F 5.2 5000°F 5.3 | With Grain 1.5 Across Grain 2.30 With Grain 1.55 Across Grain 2.40 With Grain 1.80 Across Grain 2.50 With Grain 2.00 Across Grain 2.75 With Grain 2.40 Across Grain 3.00 With Grain 2.65 Across Grain 3.25 |
| Thermal Conductivity (Btu-ft/hr- ft ² -°F) Room Temperature | X-Y 65 Z 35 | Axial 9.68 Circumferential 7.63 Radial 4.97 | X-Y 2.7 Z 6.1 | 59.6 | With Grain 85.5 Across Grain 68.2 |
| 1000°F | X-Y 38 Z -- | Axial 11.16 Circumferential 8.24 Radial 5.22 | X-Y 3.0 Z 3.0 | 39.7 | With Grain 50.1 Across Grain 40.6 |
| 2000°F | X-Y 22 Z -- | Axial -- Circumferential 9.00 Radial 5.58 | X-Y 5.4 Z 2.5 | 25.0 | With Grain 30.2 Across Grain 27.6 |
| 3000°F | X-Y 18 Z -- | Axial -- Circumferential 9.65 Radial 5.94 | X-Y 4.3 Z 2.2 | 18.1 | With Grain 21.6 Across Grain 21.6 |
| 4000°F | | Axial -- Circumferential 10.44 Radial -- | | 13.8 | With Grain 19.0 Across Grain 19.9 |
| 5000°F | | Axial -- Circumferential 10.98 Radial -- | | 12.1 | With Grain 19.0 Across Grain 19.9 |

* c - Circumferential
r - Radial
z - Axial

6.3.3.2. Structural Temperatures. A computer model of the thermal protection system at 4 locations on the vehicle was established using the program of Ref. 32 to calculate transient structural temperatures during reentry from each of the abort trajectories. The model configuration is shown in Fig. 6.20. Structural support is provided by stainless steel.

Boundary conditions at the outboard surface were aerodynamic heating, radiative heating (at the stagnation point) and radiation to the environment. In all cases the inboard surfaces were considered to be adiabatic. A heat load of 2.7 kW/ft^2 introduced at the heat pipe zone was also included. Each material layer is divided into segments, as shown in Fig. 6.20, for an accurate conduction analysis. Temperatures are calculated for each vehicle location based on an instantaneous, heat balance at the outboard surface, while accounting for the radiative heat rejection at the surface and the inboard conduction to underlying layers. The thermophysical properties of specific heat and thermal conductivity were allowed to vary with local segment temperature. In addition, the thermal conductivity of the zirconia felt was allowed to vary with ambient pressure. The computer program utilizes the Crank-Nicholson numerical approximation to pure conduction, and a modified form of this approximation in cases subject to boundary conditions. This approach results in an implicit forward-backward time difference calculation of heat balance, through a matrix solution of a simultaneous equation set.

Maximum reentry temperatures calculated for each vehicle location and for each trajectory are given in Table 6.13. Comparative transient temperatures are plotted in Fig. 6.21. The most severe heating of the stainless steel structure generally occurs during orbital decay reentry for which the long heat pulse allows significant inboard heat conduction. The highest external temperatures occur during the steep reentry. Tumbling heating corresponding to Case 3, Section 6.3.1.1, for a separation failure case was not calculated but should closely correspond to side wall temperatures for the -90° reentry case.

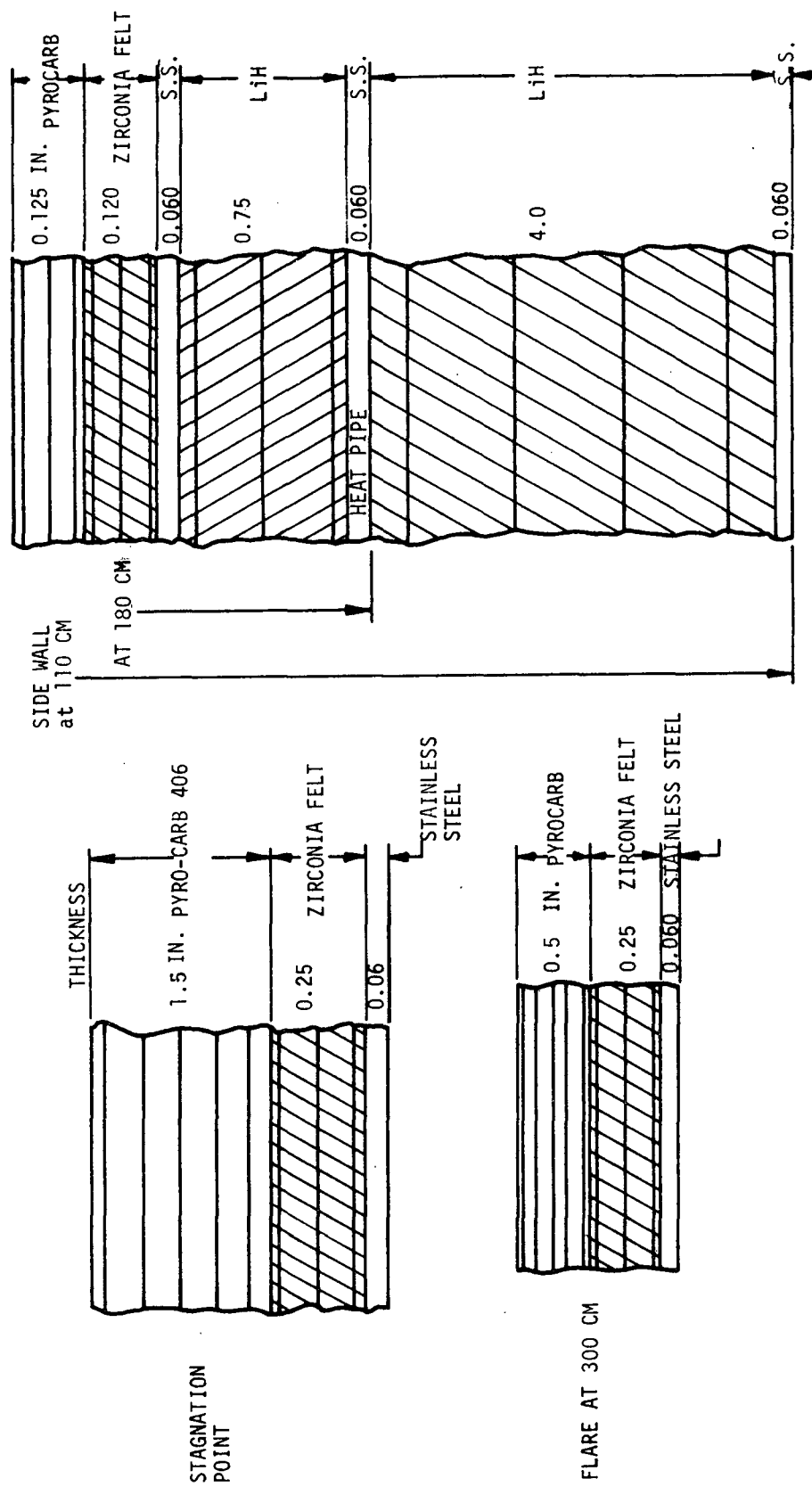


Fig. 6.20. Thermal protection system computer model

TABLE 6.13

MAXIMUM REENTRY TEMPERATURES

Ballistic Coefficient, $\beta = 17.5$ psf
(85.5 kg/m²)

| <u>Location</u> | Reentry Angle, $\gamma = -90^\circ$ | (Temperatures in °K) | | | | |
|---------------------|-------------------------------------|----------------------|------|------|------|------|
| | | -60° | -40° | -20° | -10° | 0° |
| Stag. Pt: | Outer Pyro-Carb | 4070°K | 3880 | 3428 | 3010 | 1981 |
| | Inner Pyro-Carb | 1507 | 1473 | 1566 | 2324 | 1945 |
| | Structure | 713 | 703 | 727 | 925 | 1252 |
| Sidewall @ 110 cm : | Outer Pyro-Carb | 1050 | 1010 | 1003 | 913 | 720 |
| | Outer Structure | 886 | 886 | 887 | 891 | 926 |
| | Heat Pipe | 943 | 943 | 944 | 981 | 967 |
| | Inner Structure | 883 | 883 | 883 | 883 | 885 |
| Sidewall @ 180 cm: | Outer Pyro-Carb | 1042 | 1001 | 1010 | 987 | 724 |
| | Structure | 886 | 886 | 888 | 893 | 933 |
| | Heat Pipe | 968 | 970 | 972 | 976 | 1015 |
| Flare @ 300 cm | Outer Pyro-Carb | 4383 | 4028 | 3871 | 3013 | 1156 |
| | Inner Pyro-Carb | 2651 | 2469 | 2658 | 2812 | 1152 |
| | Structure | 681 | 658 | 680 | 799 | 662 |

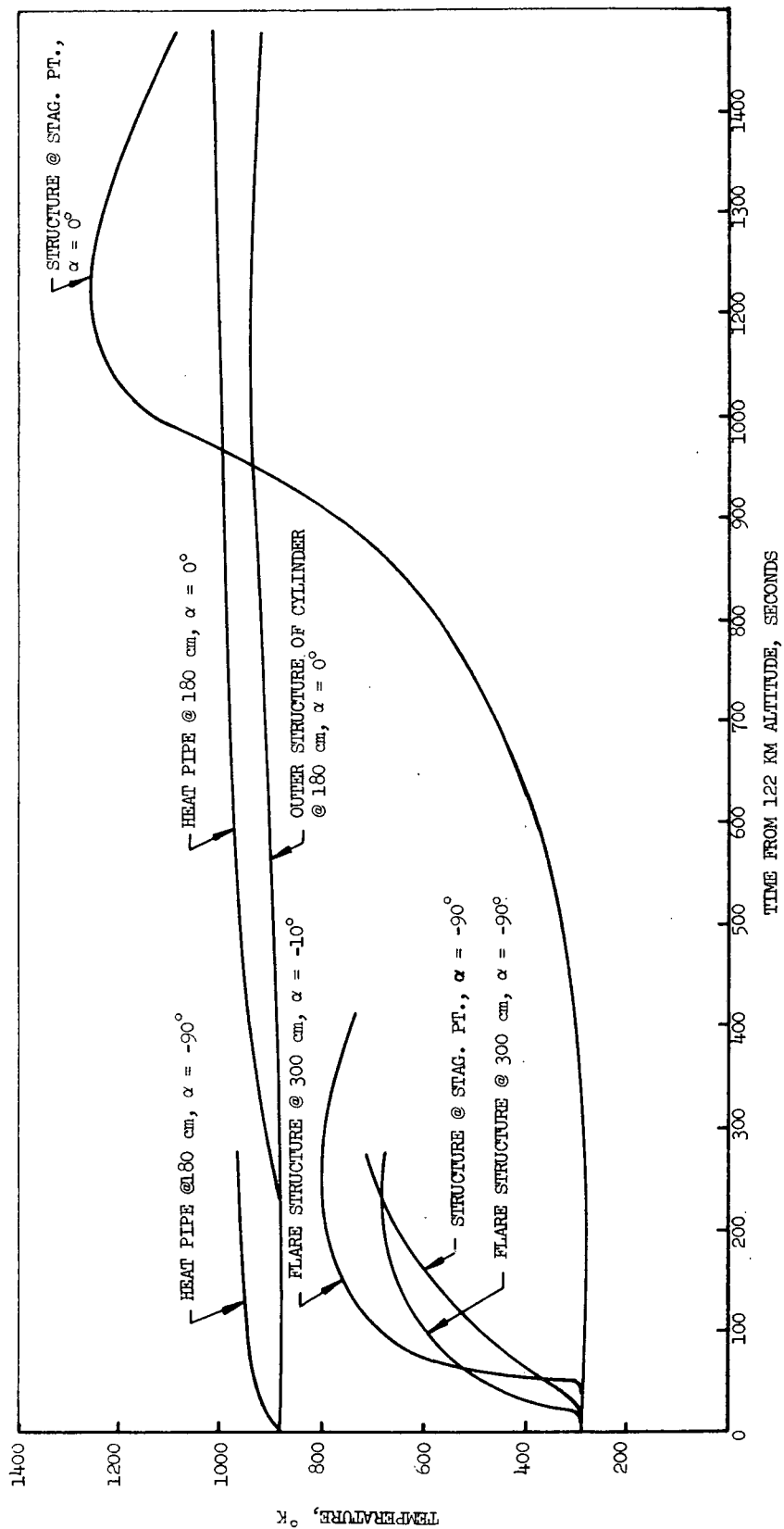


Fig. 6.21. Comparative transient temperatures

6.3.3.3. Graphite Ablation. The predominant mode of graphite ablation in the 1000°C to 2500°C temperature regime is due to diffusion controlled oxidation. This is illustrated in Fig. 6.22 (from Ref. 33). At lower temperature, ablation is reaction rate controlled while at higher temperatures sublimation prevails, and depends upon local pressure.

Figure 6.23 shows the variation of the normalized mass loss as a function of surface temperature and stagnation pressure. The normalizing factor is the diffusion controlled oxidation mass transfer rate. Essentially, the diffusion controlled oxidation regime is independent of surface temperature and can be put into the form

$$\dot{m}_D R_N / P_e^{1/2} = 6.2 \times 10^{-3}$$

where: \dot{m}_D = diffusion controlled mass loss rate, lb/ft²-sec
 R_N = nose radius, ft
 P_e = stagnation pressure, lb/ft²

Transient mass loss rates were calculated from the above equation in conjunction with Fig. 6.23. The results are shown in Fig. 6.24 for the extremes of reentry at superorbital velocities. Although a very high mass loss rate is experienced during -90° reentry due to sublimation, a greater mass loss occurs during -10° reentry as a result of the substantially longer heat pulse. Corresponding dimensional change of the Pyro-Carb 406 is 2.1 cm and 3.6 cm, respectively.

6.4. TERMINAL VELOCITY IMPACT SYSTEMS

6.4.1. Aerodynamic Flare/Honeycomb

Parachutes were used during the initial studies for the RTPS for drag augmentation to limit the earth impact terminal velocity to 26 m/sec. Without parachutes the velocity would be 89 m/sec (292 fps) for the original 122-cm diameter flare. However, a significant reduction in terminal velocity can be realized by increasing the flare diameter. The impact velocity is approximately proportional to the reciprocal of the flare diameter, while

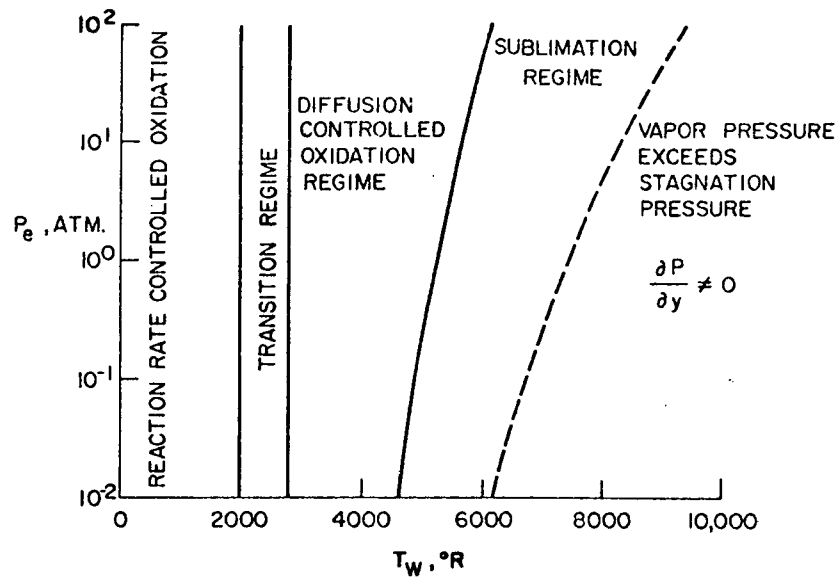


Fig. 6.22. Mass transfer regimes for ablating graphite

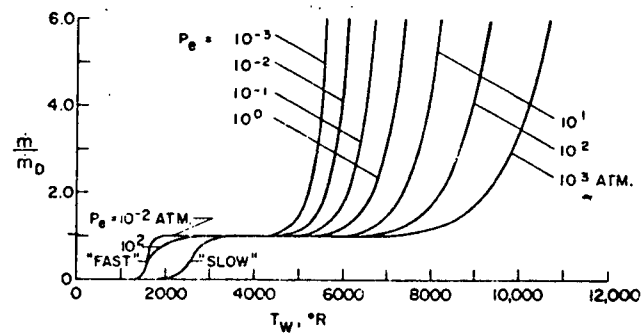


Fig. 6.23. Normalized hypersonic ablation rate of graphite over the entire range of surface temperature

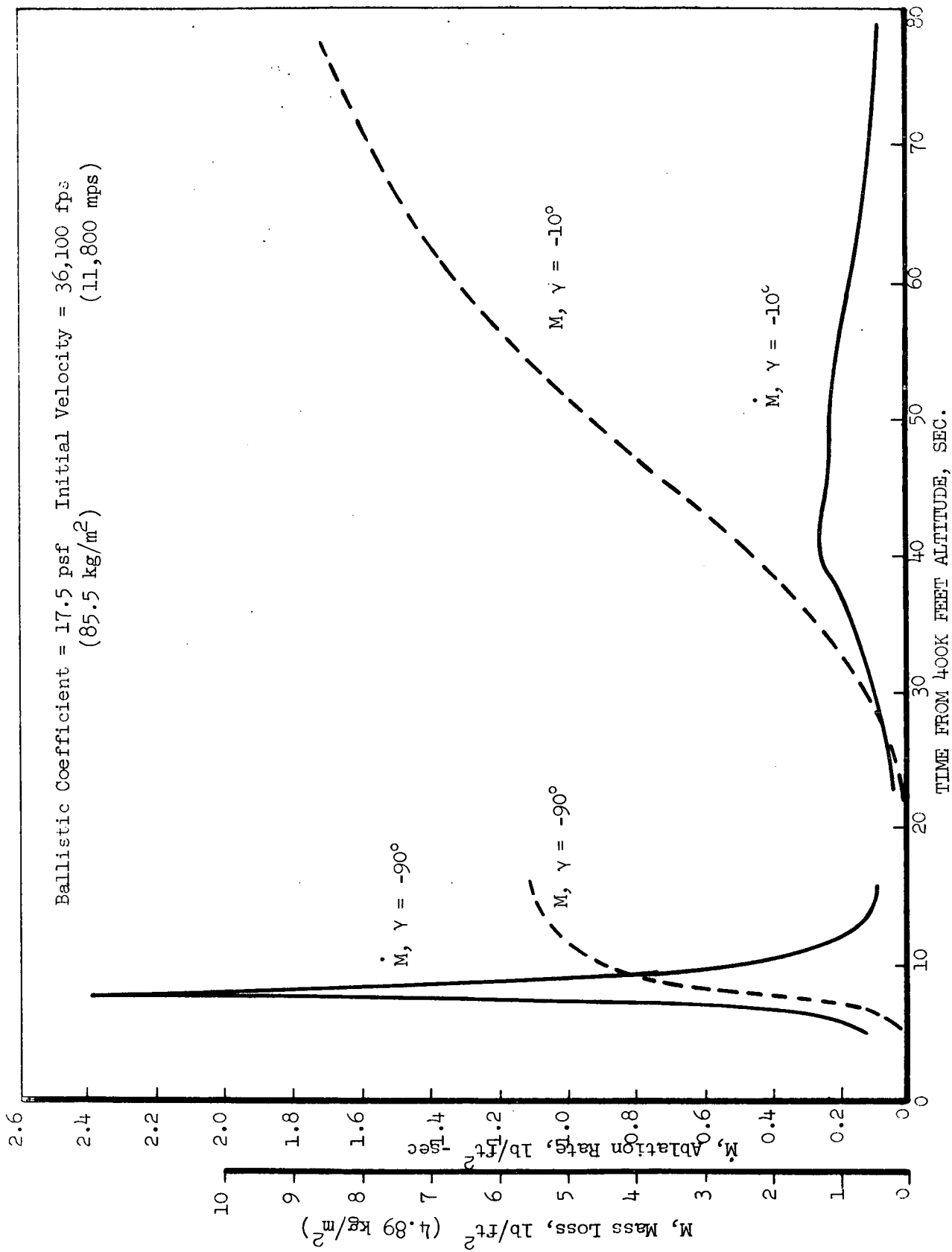


Fig. 6.24. Stagnation point ablation

the mass of the flare varies as the square of the diameter. Consequently, there is a practical limit to the size of the flare.

The effect of higher terminal velocities on the mass of a honeycomb energy absorption system can be evaluated by determining the required crushing strength using the formula:

$$f_{cr} = \frac{WG}{A}$$

where,

W = mass of the impacting system,

G = design deceleration limit in g's, and

A = impact area.

This stress must be corrected for possible variations in the impact angle due to wind and gust effects, and by a safety factor to account for observed decreases in strength with higher velocities. This correction will be between 20 and 50%, depending on the wind velocity. Variations in honeycomb length with terminal velocity are shown in Figure 6.25 and account for the fact that only 70% of the total honeycomb thickness is available for crushing. A summary of the various honeycomb characteristics for two flare diameters is presented in Table 6.14. The specific energy of the system is 20,000 joules/kg, which is comparable with frangible tubes (120,000 joules/kg) when taking into account that a minimum of 5 tubes are required to provide the necessary angular distribution for a 20 mph wind condition. The honeycomb mass for a 244 cm flare is 25.1 kg, compared to 12.0 kg for the reference design with parachutes.

The influence of flare diameter and angle on mass is shown in Figure 6.26. Also shown is the resulting variation in honeycomb mass and the combined masses for the 45° flare angle case. A minimum mass is obtained at a flare diameter between 7 and 8 feet (244 cm). Increasing the flare angle to 60° will reduce the mass slightly and will lower the terminal velocity approximately 9% (due to an increase in the subsonic drag coefficient) and will reduce the required thickness of the honeycomb by 18%. The disadvantage of increasing the flare angle is that the hypersonic drag coefficient will

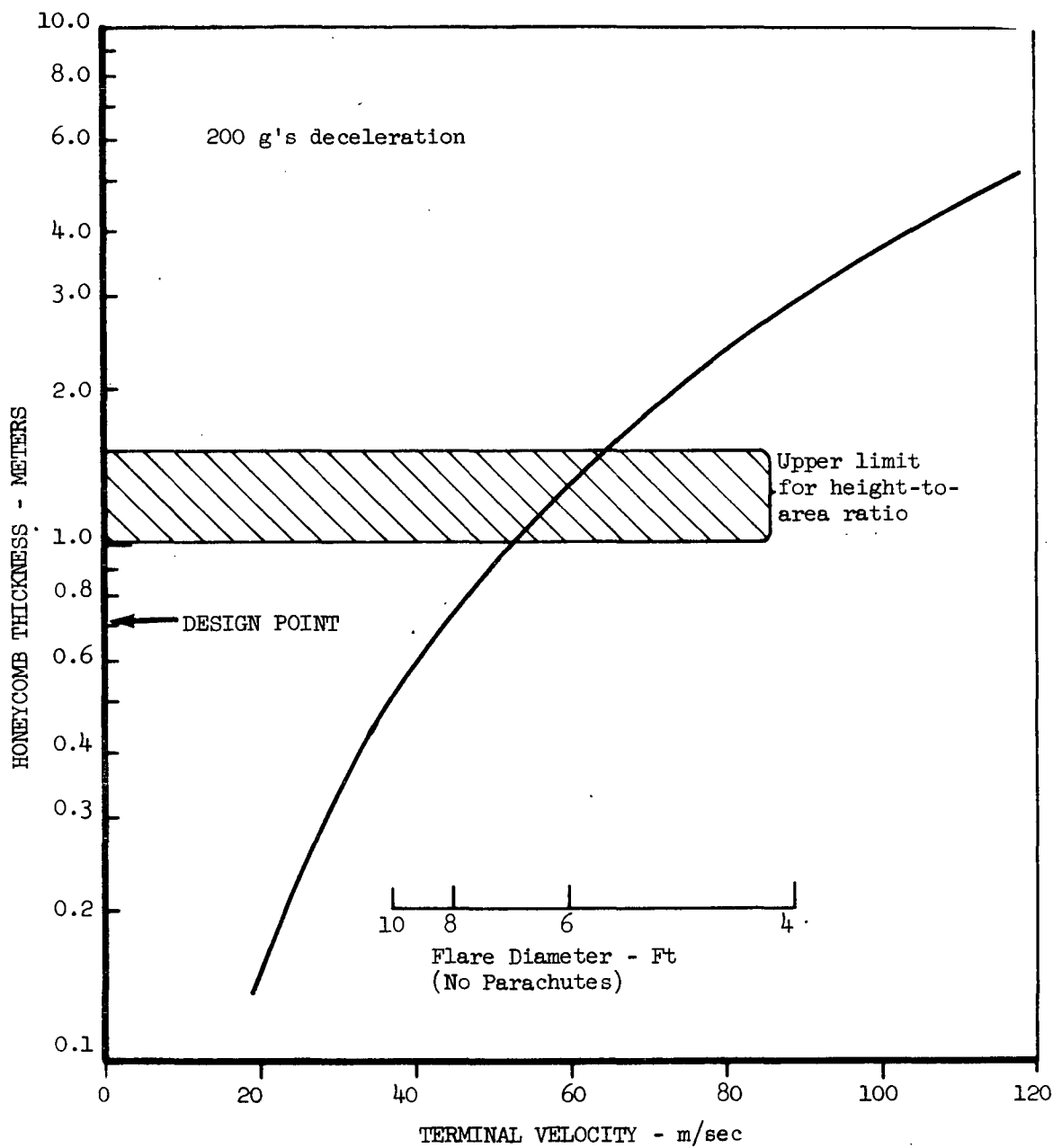


Fig. 6.25. Thickness of honeycomb energy absorption material with sea level terminal velocity

TABLE 6.14
CHARACTERISTICS OF THE HONEYCOMB ENERGY ABSORPTION
SYSTEM WITHOUT PARACHUTES

| | FLARE DIAMETER | |
|--|---|---|
| | 122 cm (4 ft) | 244 cm (8 ft) |
| Sea Level Terminal Velocity | 89 m/sec (292 fps) | 45 m/sec (147 fps) |
| Impact Stopping Distance for 200 g's Deceleration | 202 cm (6.62 ft) | 51.4 cm (1.68 ft) |
| Honeycomb Thickness | 288 cm (9.45 ft) | 73.4 cm (2.41 ft) |
| Honeycomb Crush Strength | 441 n/cm ² (640 psi) | 469 n/cm ² (680 psi) |
| Maximum Impact Angle | 5.7° | 11.3° |
| Loss of Crushing Strength | 22 % | 33 % |
| Honeycomb Density | 148 kg/m ³ (9.2 lb/ft ³) | 172 kg/m ² (10.7 lb/ft ³) |
| Kinetic Energy | 1.8(10) ⁶ Joules (1.3x10 ⁶ ft-lb) | 4.8(10) ⁵ Joules (3.5x10 ⁵ ft-lb) |
| Energy Absorbing Capacity | 9(10) ⁶ J/m ² (6x10 ⁵ ft-lb/ft ²) | 2.4(10) ⁶ J/m ² (1.6x10 ⁵ ft-lb/ft ²) |
| Specific Energy of Honeycomb | 2(10) ⁴ J/kg (7x10 ³ ft-lb/lb) | 1.9(10) ⁴ J/kg (6.3x10 ³ ft-lb/lb) |
| Honeycomb Mass | 84.5 kg | 25.1 kg |
| Aerodynamic Flare Mass | 7.8 kg | 35.7 kg |
| Total Impact Protection Mass | 92.3 kg | 60.8 kg |

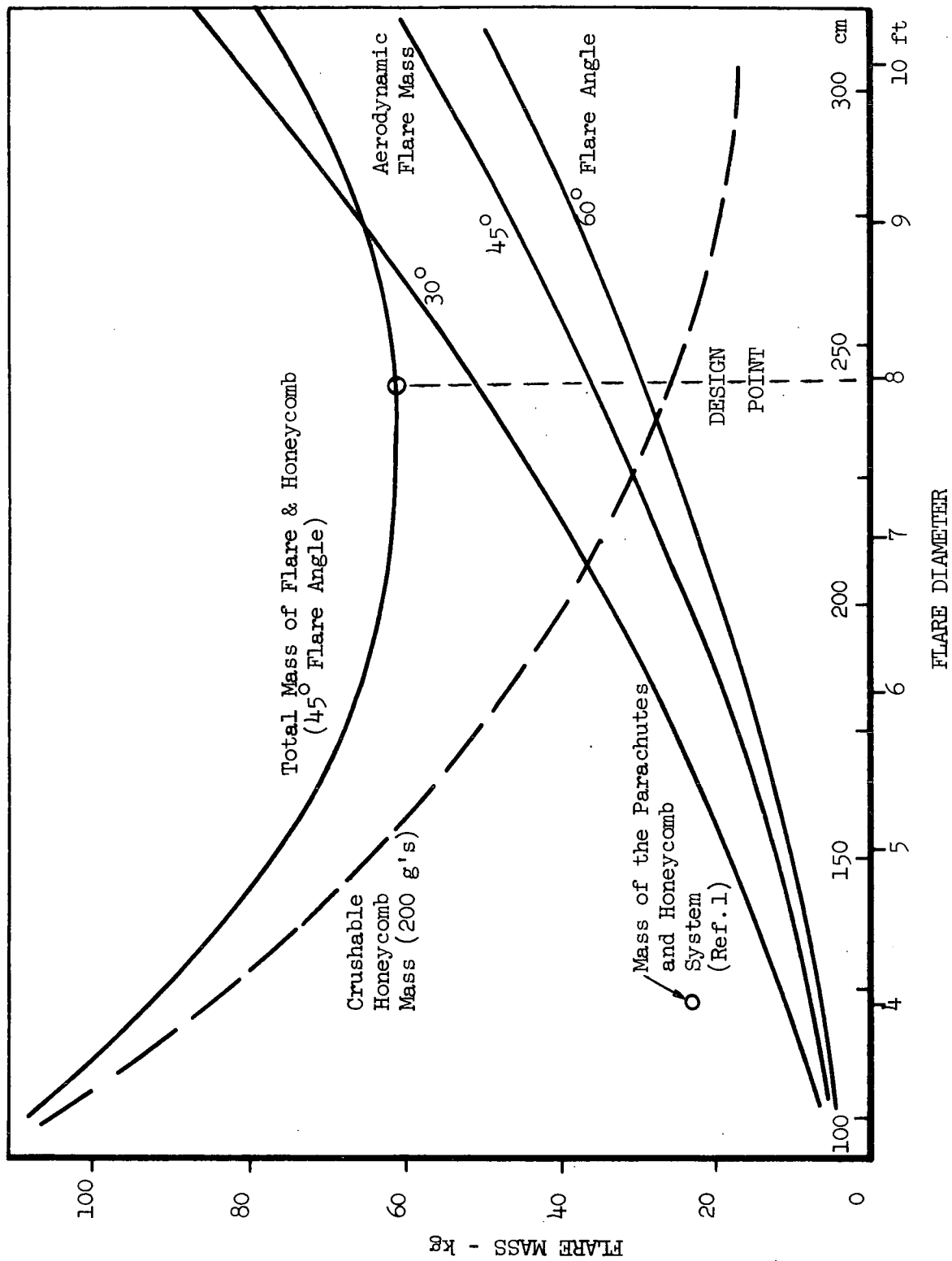


Fig. 6.26. Tradeoff of RTPS Aerodynamic flare mass and honeycomb energy absorber mass with flare diameter

increase due to aerodynamic effects and the heating will rise, with a possible requirement for additional graphite insulation.

Due to wind and gust effects the safety system may have a velocity component parallel to the surface of the earth at the time of impact. If the terminal velocity is comparable with the wind velocity, the angular displacement may be significant enough to reduce the energy absorption capabilities of the honeycomb. Furthermore, a high angular velocity could impose excessive "g" loads on the radiator heat pipes. However, analysis has shown that due to the short time duration of the impact event (23 milliseconds at 45 m/sec), the angular rotation will be only 1° , which will not affect the honeycomb crushing characteristics. Additionally, the maximum predicted sidewise "g" load on the auxiliary radiator will be only 16 g's, which is small relative to the 200 g vertical impact load.

6.4.2. Alternate Energy Absorption Systems

The two energy absorption concepts considered for the safety system have been honeycomb structures and frangible tubes. The frangible tube concept affords a means to achieve the maximum specific energy (joules/kg) of metals, where Maraging steel has one of the highest energy absorption potentials (260,000 j/kg theoretical maximum), which is about twice that of aluminum alloys. However, frangible tubes have the primary disadvantages of unpredictable load levels (Ref. 33) and poor angular capabilities (Ref. 34). Other passive energy absorption schemes, such as collapsible metal tubes and hydraulic cylinders (Ref. 33), have poor efficiency, cause severe load fluctuations and are generally less desirable than honeycomb. Active or cyclic devices, such as retrorockets and cyclic strain devices, have inherent reliability problems associated with controls and orientation.

Frangible tube system mass tradeoff calculations were performed to determine the potential of this design concept to replace the original honeycomb and parachute reentry safety equipment. Table 6.15 tabulates design characteristics of a potential frangible tube energy absorption system. Although the weight is comparable to the honeycomb/flare combination, it was

TABLE 6.15
FRANGIBLE TUBE DESIGN WITHOUT PARACHUTES

| | |
|-----------------------------|--------------------|
| Input Velocity | 89 m/sec (292 fps) |
| Design Deceleration/Mass | 200 g's /400 kg |
| Assumed Cross Wind Velocity | 9 m/s (20 mph) |
| Tube Diameter | 6.31 cm |
| Wall Thickness | 0.34 cm |
| Stroke Length | 202 cm |
| Mass of Tube | 10.4 kg |
| Mass of 4 Dies | 3.7 kg |
| Frangible Tube System Mass | 70 kg |

rejected because of its long length, developmental status, and overall design uncertainty. Honeycomb energy absorption systems, on the other hand, are well developed and can be fabricated in a large variety of configurations with a wide range of energy absorption capacity. In addition, honeycomb systems can be improved by loading the cells with rigidizing foam, which increases the energy absorption and crush strength, and improves the load response characteristics. Lastly, considerable aerospace experience has been obtained on honeycomb systems which were used on the Surveyor and the Apollo Command Module and LEM vehicles (Ref. 33).

The land impact requirement for the RTPS is similar in some respects to that of a mobile nuclear reactor. Recent work on reactor impact protection systems has been discussed with NASA Lewis personnel (Refs. 35 and 36). Their approach has been to abandon energy absorption schemes in favor of surrounding the reactor with a containment vessel. The vessel and its contents then absorb the entire impact energy without rupturing the containment vessel.

Reentry terminal velocities of the RTPS are sufficiently low so that energy absorption systems can be designed and a 4π direct-impact system is not required. Another advantage of the RTPS system is that the impact attitude can be assured with the aerodynamic flare stabilizer. Based on the various energy absorption schemes investigated, the crushable honeycomb appears to be the most acceptable approach considering design confidence, load characteristics and specific energy.

6.4.3. Earth Impact Burial

6.4.3.1. System Burial. Earth penetration models developed by Young (Ref. 37) of Sandia Labs were used to determine if impact velocities were sufficient to cause burial. The empirical relationship developed by Young, based on approximately 200 full-scale penetration tests, is given by the following equation:

$$D = 0.53 \text{ SN}(W/A)^{1/2} \ln(1 + 2V^2 10^{-5}),$$

$V < 200 \text{ feet per second}$

D = depth of penetration, measured along the penetration path, feet
 V = impact velocity, fps
 S = soil constant, depends on specific soil conditions
 N = constant, vehicle nose performance coefficient (taken as 0.82 for a spherical nose)
 W = total vehicle mass, pounds
 A = cross-sectional, or frontal area, square inch.

Table 6.16 summarizes computed burial depths for different flare designs and for three different types of soils. For an 8-foot (244 cm) diameter flare with a 45° angle, the maximum penetration depth is only 0.57 meters. By comparison, the distance from the vehicle nose to the active portion of the auxiliary radiator is approximately 1 meter. Consequently, unless the system impacts into a moist or highly plastic soil, earth penetration depth will not cause burial.

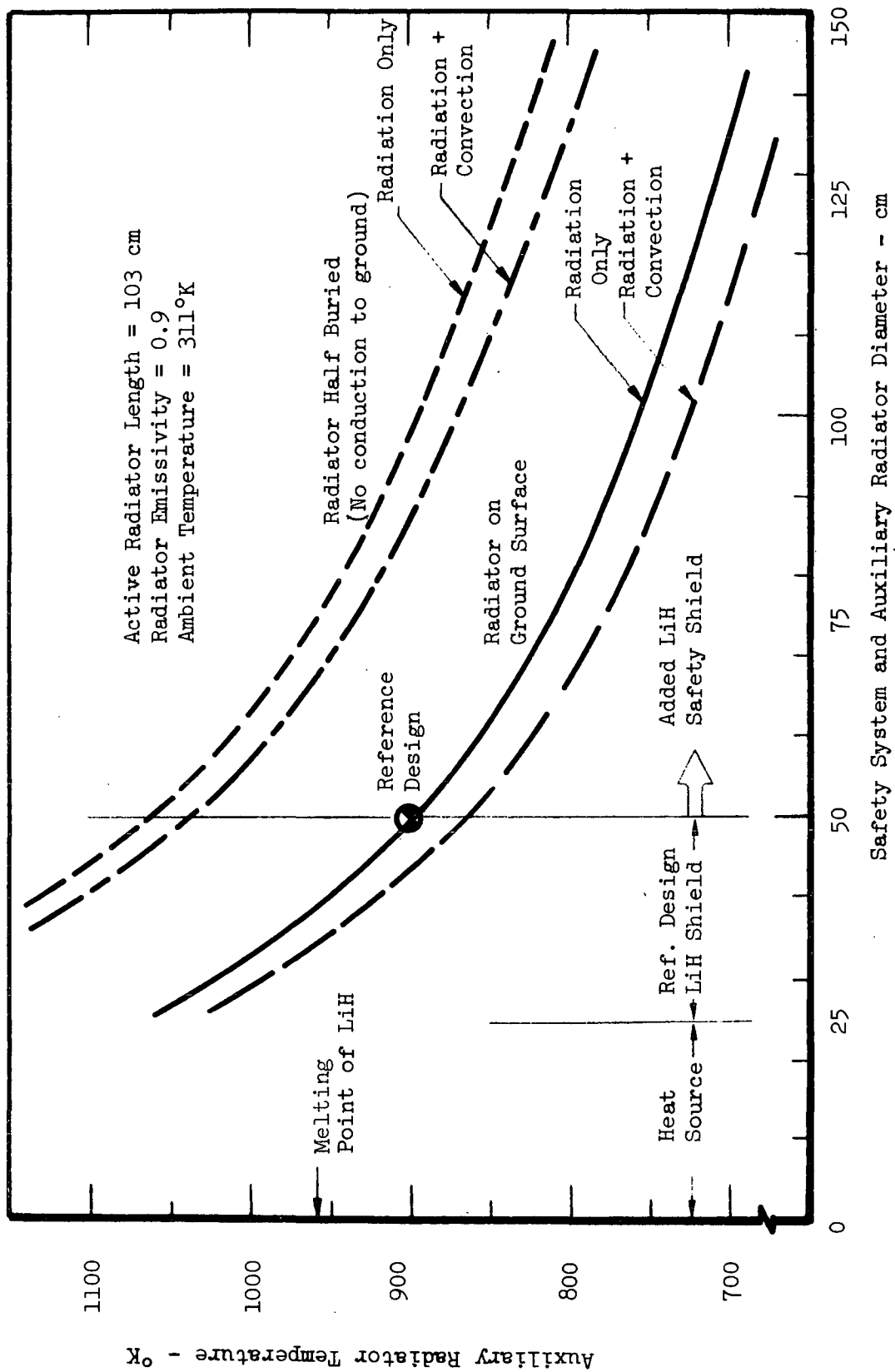
6.4.3.2. Heat Source Temperatures. In the unlikely event that the heat source is broken upon impact with the earth and a capsule is lying upon the ground, it will lose heat through radiation to its surroundings, air convection over the capsule and conduction to the earth. If one-half of the capsule surface is considered to dissipate the 325 watts of isotopic heat, then the capsule surface temperature will be 1060°K , assuming turbulent natural convection and a surface emittance of 0.8. If the capsule becomes completely buried in the earth, then the heat must be dissipated into the earth and from the earth to the atmosphere. For dry sandy loam with $k = .00934 \text{ W/cm } ^\circ\text{K}$ and a burial depth of 30 cm, the ΔT between the earth's surface and the capsule is 836°K . Assuming the heat leaves the earth over a 0.09 m^2 plane, the ΔT between the earth and air is 200°K . Therefore the predicted capsule temperature in case of burial is 1350°K , which is considerably below the melting point of W-Re and in a range where capsule integrity would be maintained for several hours (typical recovery times) prior to air oxidation.

6.4.3.3. Auxiliary Radiator Temperatures. Figure 6.27 shows temperature tradeoffs of the RTPS with diameter of the safety radiator for the case of no

TABLE 6.16
COMPUTED BURIAL DEPTH FOR TERMINAL VELOCITY
IMPACT OF THE RTPS ONTO VARIOUS SOILS

| RTPS Flare Design | Terminal Velocity | Burial Depth for Different Soil Types | | |
|-------------------------|----------------------|--|---|------------------------------------|
| | | Rock Highly Welded, Fine Grained Agglomerate (S = 1.07) | Sand, Silty, Clayey, Dense (Desert Alluvium) (S = 4.4) | Sand, Loose, Moist (S = 6.5) |
| 4 ft flare | 89 mps (292 fps) | .25 m [*] (.81 ft) | 1.10 m [*] (3.32 ft) | 1.49 m [*] (4.91 ft) |
| 6 ft flare | 59 mps (193 fps) | .14 (.46) | .58 (1.90) | .86 (2.81) |
| 8 ft flare (45°) | 45 mps (147 fps) | .09 (.31) | .38 (1.26) | .57 (1.86) |
| 8 ft flare (60°) | 41 mps (134 fps) | .08 (.26) | .32 (1.06) | .48 (1.57) |

* These values are increased by 13% when the high velocity relationships are applied.



• Fig. 6.27. Post Impact Temperature of Auxiliary Radiator Versus Radiator Diameter

burial and partial burial. The results show that temperatures for the burial case will cause melting of the LiH, but should not exceed the 1200°K heat pipe limit.

6.4.4. Effect of Impact on Fuel Form

As described in Section 6.4.1., the crushable honeycomb structure in the nose of the safety equipment limits the rate of deceleration of the radioisotope heat source to 200 G's (19,600 m/sec²). The effect of this deceleration on the fuel form is to produce a compressive stress. If the restraining effect of the cladding is ignored, the stress in the fuel varies linearly from zero at the end of the capsule nearest the aerodynamic flare to a maximum at the end nearest the nose. This maximum is

$$\sigma = \frac{m a}{A} = \frac{0.160 (19600)}{\frac{\pi}{4} (0.898 \times 10^{-2})^2} = 5 \times 10^6 \frac{\text{N}}{\text{m}^2}$$

where m = the mass of fuel (kg),

a = the rate of deceleration (m/sec²), and

A = the cross-sectional area of fuel (m²).

A compressive stress of 5×10^6 N/m² (700 psi), should have no effect on a ceramic material like Cm₂O₃. Thus the fuel is expected to survive impact on land with the fuel form completely intact.

6.5 RADIATION SHIELDING TRADEOFFS

Various shielding studies were performed during the first phase of the RTPS Study (Ref.1). Additional evaluations were required, however, to evaluate system considerations on lowering accident radiation levels from the ²⁴⁴Cm fuel. Results of LiH shielding scaling calculations indicate that the overall system diameter increases 10 cm for 200 kg increase in shield

mass. This mass is nearly twice that of the shield alone, with the balance allowing for mass increases in the structure and other major components. The effect of additional LiH shielding around the heat source on neutron dose rate is shown in Fig. 6.28 as a function of added safety system mass and system outside diameter. Dose at distances of one, three and ten meters were considered, and correspond approximately to: (1) surface conditions, (2) the closest reasonable distance for short-term exposure, and (3) a representative distance for the immediate surrounding area which could be used as an estimate for longer term exposure.

There are no specific guidelines which can be applied to the allowable radiation dose from the accidental land impact of the heat source. A level of 1 r/hr at 1 meter from the surface is the maximum allowable dose due to damage resulting from an isotope fuel cask drop test (Ref. 38). Another applicable limit is the 25 r whole body dose which is used for reactor siting studies (10 CFR-100). This also is the maximum accident or emergency exposure for once in a lifetime occurrence (NBS Handbooks 49, 69, and 92). Applying the 1 r/hr limit at one meter from the surface would require that approximately 20 cm of LiH be added to the reference design thickness of 10 cm. This thickness corresponds to a 400 kg increase in safety system mass. At a distance of 3 meters, a 200 kg increase would be sufficient to limit the dose rate to 1 r/hr or a 24 rem exposure in 1 day. At the 10 meter distance, only 70 kg of additional mass is required to limit the whole body dose to 25 rem in one week. These mass increases must be compared to the masses of other types of safety equipment, such as electronic beacons to enhance recovery capabilities and improved structures to resist impact damage. Considering these factors, in addition to recovery practices employed for other aerospace programs, it was determined that recovery times of 6 to 12 hours on land, with tracking data, could be expected. Consequently, at a 3 meter distance, the maximum possible accidental dose between impact and recovery would be less than 25 mr; and no added LiH shielding is required.

As the thickness of LiH shielding is increased, the cylindrical portion of the safety system radiator increases and the reentry characteristics of the system vary. Figure 6.28 shows preliminary estimates of the effect of

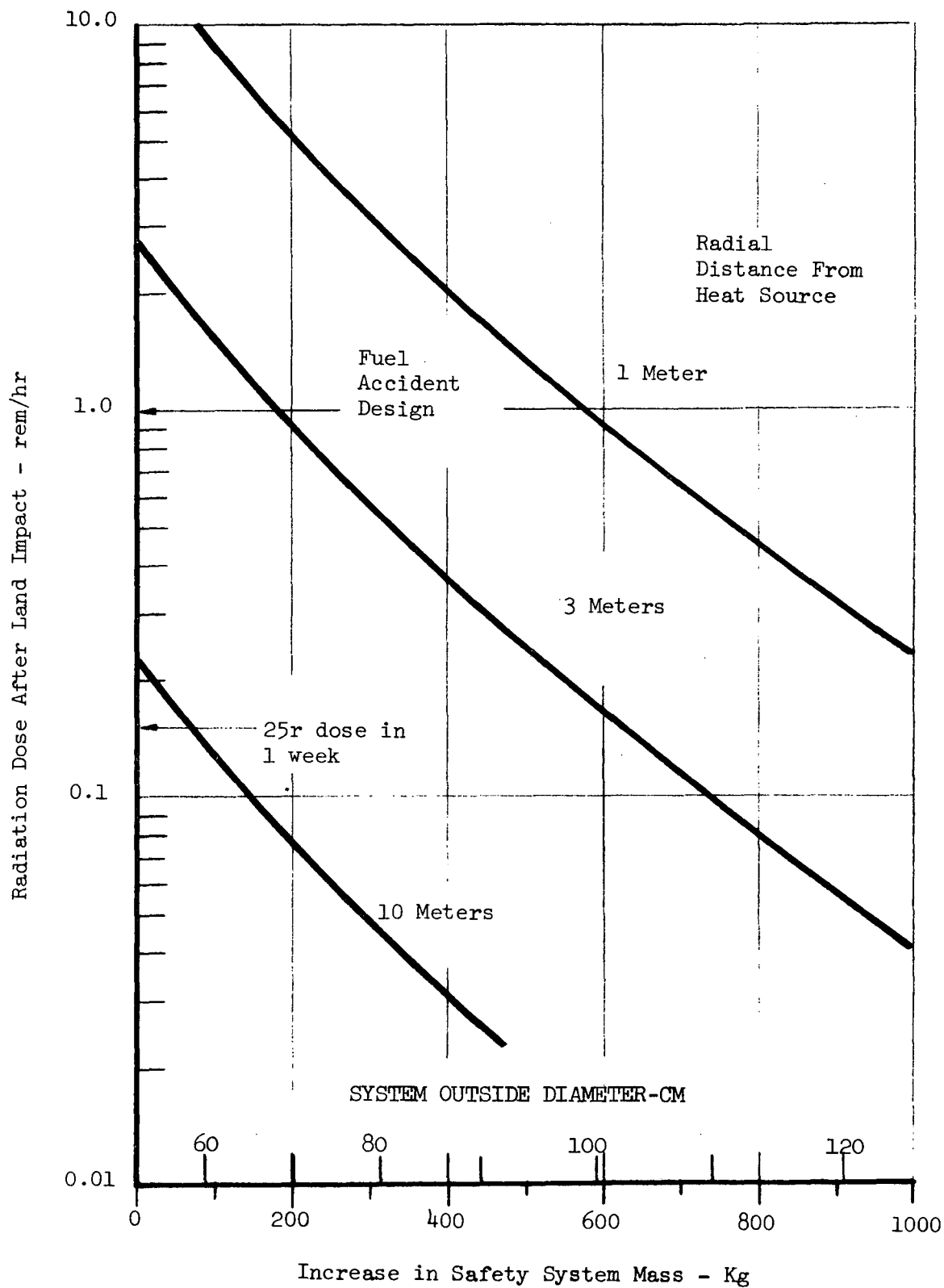


Fig. 6.28. Radial dose rates from heat source after impact versus increase in mass

added safety system shielding mass and diameter on sea level terminal velocity of the heat source without aerodynamic retardation devices. The computed subsonic ballistic coefficient for the reference design was 101 lb/ft² (490 kg/m²) which corresponds to a sea level terminal velocity of 89 m/sec, or 104 m/sec at a 10,000 ft altitude. The terminal velocity was computed with the following relation:

$$V_T = \sqrt{\frac{2g\beta'}{\rho}}$$

where:

V_T = terminal velocity,

β' = subsonic ballistic coefficient (weight/drag coefficient x projected area)

ρ = density of air at a specified altitude.

The curves in Fig. 6.29 show that the terminal velocity will increase rapidly with additional safety system shielding unless the flare diameter is also increased. Table 6.17 compares pertinent design information for the reference design and one that includes an added 200 kg mass--due either to LiH, insulation, graphite addition or other system change. For comparison, values are shown for flare diameters from 122 to 244 cm.

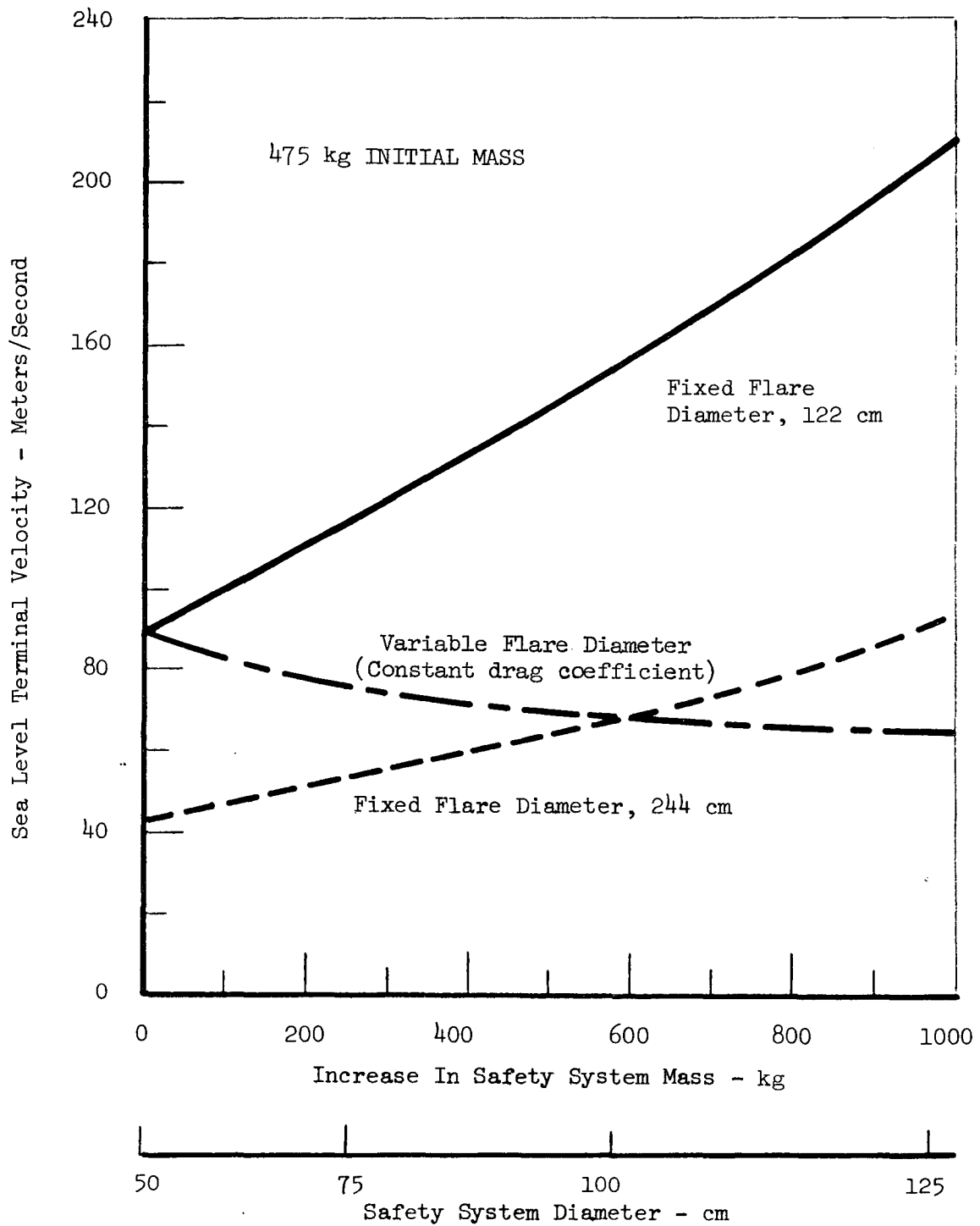


Fig. 6.29. Sea level terminal velocity changes with increases in safety system mass and diameter

TABLE 6.17

SUMMARY OF DESIGN CHARACTERISTICS FOR 200 kg INCREASE
IN SAFETY SYSTEM MASS CASE

| | Reference Design | 200 kg Mass Increase |
|--|---------------------|-------------------------|
| 1. Radiation Dose (r/hr) | | |
| • 1 Meter from Heat Source | 15.6 | 5.2 |
| • 3 Meters from Heat Source | 2.8 | 0.92 |
| 2. Post Land Impact Temperatures (°K) | | |
| • Radiation Heat Transfer | 900 | 820 |
| • Radiation Plus Convection | 865 | 790 |
| • System Half Buried | 1035 | 950 |
| 3. Geometry (cm) | | |
| • Diameter of Safety System | 50.3 | 70.3 |
| • Thickness of LiH Shield | 10 | 20 |
| 4. Drag Coefficient | | |
| • Hypersonic | 1.16 | 1.13 |
| • Subsonic | 0.77 | 0.71 |
| 5. Ballistic Coefficient (kg/m ²) | | |
| • Hypersonic - Fixed Flare | 329.4 | 490.1 |
| | (67.4 psf) | (100.3 psf) |
| - Increased Flare* | 329.4 | 243.9 |
| | (67.4 psf) | (49.9 psf) |
| • Subsonic - Fixed Flare | 495.5 | 776.5 |
| | (101.4 psf) | (158.9 psf) |
| - Increased Flare* | 495.5 | 366.5 |
| | (101.4 psf) | (75.0 psf) |
| 6. Terminal Velocity (Sea Level) m/sec | | |
| • Fixed Flare Diameter (122 cm) | 89.0 | 111.6 |
| | (292 fps) | (366 fps) |
| • Increased Flare Diameter | 89.0 | 76.8 |
| | (292 fps) | (252 fps) |
| • 8' Diameter Flare (244 cm) | 43.3 | 52.4 |
| | (142 fps) | (172 fps) |
| 7. Stagnation Heating Coefficient (Nose) (Heating relative to reference design) | | |
| • Fixed Flare Diameter (4 ft, 122 cm) | 1.0 | 1.03 |
| • Increased Flare Diameter | 1.0 | 0.73 |
| • 8' Diameter Flare (244 cm) | 0.50 | 0.50 |

*Flare diameter increased directly with safety system diameter (170.6 cm for 200 kg case).

7. LIFETIME LIMITING MECHANISM

The potential for achieving the 36,000 hour lifetime, required for a class of missions was examined. The Cm_2O_3 capsule (at 2030°K surface temperature) and emitter heat pipes (at 1900°K) are expected to be the limiting components. Of principal concern is the effect of free oxygen released from Cm_2O_3 on the isotope capsules and the emitter heat pipes.

7.1. EFFECT OF OXYGEN ON THE FUEL CAPSULES

The oxygen pressure over Cm_2O_3 at 2073°K (1800°C) is estimated to be of the order of 10^{-5} - 10^{-6} torr (Ref.39). The exact oxygen pressure will depend on the impurities present and their concentration. Further, the vapor species in the vaporization reaction of Cm_2O_3 have not been definitely characterized.

At 5×10^{-6} torr oxygen pressure and 2073°K (1800°C) a sublimation rate of 7×10^{-3} mg/cm² hr of tungsten from the tungsten -26% rhenium alloy is possible (Ref.40). This is equivalent to an effective removal rate of 5×10^{-9} m/hr. In 36,000 hours the potential sublimation loss would be 0.2 mm. This reaction rate is essentially linear with oxygen pressure. Thus the removal rate would be reduced to 0.02 mm per 36,000 hours at an oxygen pressure of 5×10^{-7} torr.

The effect of this sublimation removal of tungsten would be to leave a porous surface layer rich in rhenium. However, in a 10,000 hour life test of Cm_2O_3 at 2123°K (1850°C) encapsulated in W-26% Re, no such porous layer has been observed (Ref.41). This may have been due to the sealed condition of the capsule which prevents loss of tungsten oxide vapors. Another possibility is that the oxygen pressure over Cm_2O_3 is suppressed by the presence of

impurities such as the Pu_2O_3 formed by radioactive decay of Cm_2O_3 . It would appear that oxygen pressure over the fuel is quite important to the lifetime of the fuel capsule, and, as discussed below, to the lifetime of the emitter heat pipes. Better definition of the vaporization species at temperature is recommended.

Should oxygen induced sublimation of W-26% Re alloy prove to be a problem, remedies may be found. One of these is to coat the surfaces with a layer of rhenium metal. Rhenium sublimation under these conditions is lower than that of tungsten by an order of magnitude.

7.2. EFFECT OF OXYGEN ON THE EMITTER HEAT PIPES

The emitter heat pipes will be exposed to oxygen diffusing through the walls of the capsule and leaking through the helium vent plug. Effects of the oxygen on the tungsten walls of the heat pipes and on the lithium working fluid are both considered.

The permeation coefficient of oxygen through tungsten at 2030°K is $0.7 \text{ cm}^3 (\text{stp})\text{-mm}/\text{cm}^2 \text{ hr atm}^{\frac{1}{2}}$ (Ref.42). If the oxygen pressure is 5×10^{-6} torr within the Cm_2O_3 capsules and the pressure outside the capsules is much lower, the permeation rate of oxygen through the 0.5 mm-thick walls of each capsule is $0.01 \text{ cm}^3 (\text{stp})/\text{hr}$. The leakage of oxygen through a porous plug helium vent designed to build up a helium back pressure of the order of one atmosphere is negligible by comparison. If the rate of oxygen loss were constant over the 36,000 hour lifetime of the system, the total amount of oxygen released from 136 capsules would be 70 g or 0.5 g per capsule. The rate of oxygen loss should, in fact, decrease as the oxygen pressure over the fuel is reduced by depletion of oxygen and buildup of Pu_2O_3 (0.5 g is slightly over 4% of the initial oxygen loading in the capsule, and 15% of the Cm_2O_3 will be converted to Pu_2O_3 after 36,000 hours).

The pressure of oxygen in the heat source will depend on how well the oxygen diffusing through the capsule walls is vented to space. At the initial

release rate of $0.01 \text{ cm}^3/\text{hr}$ per capsule, a vent area amounting to 10 cm^2 is necessary to reduce the oxygen pressure in the heat source to 10^{-6} torr. An oxygen vent of this size would allow about 800 watts, or 2% of the total heat to be radiated to space from the heat source. A more effective method of lowering the oxygen pressure would be to provide an oxygen getter such as tantalum within the heat source.

If the oxygen pressure in the heat source is 10^{-6} torr, the rate of sublimation removal of tungsten from the emitter heat pipe walls would be $2 \times 10^{-9} \text{ m/hr}$ or 70 m in 36,000 hours. At 10^{-6} torr, oxygen permeation of each emitter heat pipe will be $0.0015 \text{ cm}^3(\text{stp})/\text{hr}$ or 70 mg in 36,000 hours. Oxygen entering the heat pipe will be gettered by the lithium working fluid at the rate of about 1 mg of lithium per mg of oxygen. This will make some of the lithium unavailable as a working fluid and require an initial excess. Clogging of the wick with oxides will probably not be serious at the 70 mg level but must be evaluated experimentally.

7.3. TEST PROGRAM TO DETERMINE OXYGEN EFFECTS

A test program is defined here to evaluate the potential effects of oxygen released from the Cm_2O_3 fuel. A parametric test program is recommended to provide data to the system designer. Such data will permit the designer to minimize the effects of oxygen by choice of design and operating conditions. The two questions that must be answered are: How much oxygen is released; and how does oxygen affect the capsules and emitter heat pipes.

The oxygen release from Cm_2O_3 capsules should be measured by fabricating large, thin-walled capsules of W-26% Re alloy, loading them with purified $^{244}\text{Cm}_2\text{O}_3$ and welding them shut. The capsules should be sized with adequate void volume for helium accumulation to permit life tests for 10,000 hours. Each capsule should be tested in a vacuum chamber equipped with a residual gas analyzer to measure the oxygen release rate. Care must be taken to eliminate other sources of oxygen or oxygen gettering materials which could prevent the oxygen release rate from being determined accurately.

Capsule test temperatures of 1900, 2000, and 2100°K would cover the range of interest. Tests of this type could best be performed at a facility with hot cells designed for high level alpha activity, such as Oak Ridge National Laboratory.

The effect of oxygen on the emitter heat pipes should be determined by fabricating heat pipes similar to those in the reference design and operating them at similar heat fluxes in vacuum chambers with controlled oxygen pressure. Here again, long-term testing of 10,000 hour or greater duration is recommended. A range in oxygen pressure from 10^{-5} to 10^{-2} torr and a range in heat pipe temperature from 1800-2000°K are recommended. Tests of this type could best be performed at a laboratory with extensive experience in high vacuum technology and long-term life testing at thermionic temperatures, such as Gulf General Atomic.

8. COST ESTIMATES

The principal cost elements of the radioisotope thermionic power supply are the Cm^{244} fuel and its encapsulation (Ref. 1). The cost of the safety equipment is relatively low, so that the modifications made in this equipment do not have a significant effect on the cost of the power source. The only significant change in cost is a result of the reduction in mission duration from 72,000 hours (Ref. 1) to the present 36,000 hours. The reduction in time for radioisotope decay reduces the initial fuel loading (for the same loading at end-of-mission) from 51.75 kW to 44.2 kW. The cost of the fuel is reduced from \$5,175,000 to \$4,420,000, a saving of \$755,000. A revised estimate for the recurring costs of the power source is given in Table 8.1.

TABLE 8.1
FLIGHT SYSTEM COSTS

| | Unit Cost | Item Cost (10 ³ \$) |
|-------------------------------|---------------------|--------------------------------|
| Curium ²⁴⁴ Fuel | \$ 100/thermal watt | 4,420 |
| Encapsulation costs | \$ 15,000/capsule | 2,040 |
| Emitter heat pipes | \$ 5,000 | 345 |
| Thermionic converters | \$ 5,000 | 345 |
| Radiator heat pipes | \$ 2,000 | 138 |
| Power conditioning | \$ 2,000/module | 16 |
| Beryllium shield | \$ 700/lb | 38 |
| Heat source case & insulation | | 20 |
| Safety System | | |
| Auxiliary heat pipes | \$ 750 | 300 |
| Fire shield | | 30 |
| LiH shielding | | 50 |
| Reentry heat shield | | 60 |
| Structure | | 40 |
| Assembly operations | | 200 |
| Launch support equipment | | 100 |
| Auxiliary prelaunch shielding | | 30 |
| | TOTAL | <u><u>8,172</u></u> |

9. CONCLUDING SECTION

This study showed the feasibility of a passive containment system for the ^{244}Cm isotope. The passive containment system has inherent reliability and safety advantages over the original design (Ref. 1), in which mechanical systems were required to operate in certain launch abort conditions. In the present design, the launch escape rocket system is replaced by a blast shield and a fire shield. The blast shield protects against a booster explosion on the launch pad or during ascent to earth escape. The fire shield, which consists of refractory thermal insulation (zirconia felt) and a heat storage material (lithium hydride), protects the isotopic fuel and its containment vessel from a sustained propellant fire on the launch pad. The aerodynamic flare, which stabilizes the orientation during reentry from an abort trajectory, was enlarged to reduce the ballistic coefficient and the terminal velocity. At the lower velocity, the impact energy is absorbed by a crushable honeycomb structure in the nose of the reentry body, with no parachutes required to reduce the velocity.

The design changes, incorporating a passive containment system and eliminating the need for a launch escape rocket and parachutes, resulted in an increase in the mass of the safety equipment. The mass of the safety equipment, which is discarded once Earth escape has been verified, was increased by 270 kg to 575 kg. Since the safety equipment is jettisoned early in the heliocentric portion of the mission, its mass has a relatively small effect on mission performance. The reduction in payload mass due to the 270 kg increase in the safety equipment is only about 55 kg for a typical mission, such as an orbiter of Saturn.

Calculations of the effects of oxygen released from the Cm_2O_3 fuel showed that oxygen-induced sublimation of the capsule and emitter heat pipe or oxygen contamination of the lithium working fluid in the heat pipe could

limit the lifetime of the system. More experimental data on oxygen release rates and effects of oxygen are required before radioisotope power systems of this type can be designed with reasonable assurance of meeting a specified lifetime objective. It appears that lowering the temperature of the isotopic fuel and using oxygen getters in the heat source will both be effective in reducing oxygen effects on the heat source.

The next step in the development of the radioisotope thermionic power supply for electric propulsion applications should be to establish the materials and fabrication technology for the isotope capsule and emitter heat pipe. Capsule vents must be developed to release helium but minimize the loss of fuel and resist plugging by condensed fuel vapors. The bulk of this development can be performed using a non-radioactive fuel simulant. A few confirmatory tests should be performed with $^{244}\text{Cm}_2\text{O}_3$ -fueled capsules. Fabrication methods for emitter heat pipes should be developed and heat pipes tested over a range in temperature, heat flux, and oxygen pressure so that the results can be extrapolated to the long lifetimes required for electric propulsion missions.

In addition to establishing the feasibility of a 36,000-hour lifetime, the technology development efforts will determine the maximum thermionic emitter temperature and, hence, the maximum performance level for the power system. Coupled with the technology development effort to establish performance levels should be a more thorough and detailed planning effort for the total development program through the first flight. A detailed program plan will permit a more accurate estimate to be made of the development schedule and cost of the system. The decision whether to develop the system would then be made on the basis of more accurate mission performance, schedule, and cost data.

REFERENCES

1. Homeyer, W. G., C. A. Heath, and A. J. Gietzen, "Preliminary Study of a Radiosotope Electric Propulsion System" v. II, "Final Report," Gulf General Atomic Report GA-10339, 1970.
2. Paquin, M. L., "High-Temperature Multi-Foil Thermal Insulation," Inter-society Energy Conversion Engineering Conference Proceedings, Boulder, Colorado, August 1968.
3. Paquin, M. L., "Multi-Foil Thermal Insulation," Society of Aerospace Materials and Process Engineers Symposium Proceedings, 1970.
4. Paquin, M. L., Thermo Electron Corporation, Personal communication.
5. Donnelly, R. G., Oak Ridge National Laboratory, Personal communication.
6. Kemme, J. E., "Ultimate Heat Pipe Performance," in "IEEE Conference Record of 1968 Thermionic Conversion Specialist Conference," Univ. of California, Los Alamos Scientific Lab., for USAEC, 1968, p. 266.
7. Holland, J. W., and J. Kay, "Performance of a Cylindrical Geometry Thermionic Converter with an Improved Work Function Tungsten Emitter," presented at the 1967 Thermionic Conversion Specialist Conference, Oct. 30-Nov. 1, 1967, Palo Alto, California.
8. van Andel, E., "Heat Pipe Design Theory," Second International Conference on Thermionic Electrical Power Generation, 1968, p. 529.
9. Holland, J. W., and D. L. Bossean, "Thermionic Converter Network Reliability," Bureau of Ships Report GA-6102, General Atomic Division of General Dynamics Corp., 1965 (AD 436502).
10. Yates, M. K., "Influence of the Relative Probability of Converter Failure Modes on Thermionic Reactor Designs," 1966 Conversion Specialist Conference Proceedings, p. 430
11. Gutshin, G. I., et al., "Thermionic Converter Electrical Characteristics with Matrix Circuit Connection," in Proceedings of Second International Conference on Thermionic Electrical Power Generation, Stresa, May 27-31, 1968, Section F-5.
12. Fisher, C. R., "Design of a Four Cell Cluster Test, (U)" in Proceedings of Thermionic Conversion Specialist Conference, October 30-November 2, 1968, Palo Alto. (Confidential/Restricted Data)
13. Rimshaw, S. J., and E. E. Ketchen, Curium Data Sheets, USAEC Report ORNL-4357, Oak Ridge National Laboratory, January 1969.

14. "TRANSIT RTG Final Safety Analysis Report," v. I, II, III, TRW(A)-11464-0492, March 1971.
15. "Pioneer F - AEC Safety Study, Phase I and II," (Range Safety Equipment, Launch Pad Hazard and Reentry Environment - II), General Dynamics/Convair Report No. GDC-BTD 70-015, 1971.
16. Ryan, R. L., and T. W. Graham, "Isotope Reentry Vehicle Design Study Preliminary Design - Phase II - Final Report," Report Numbers N69-34989, NASA CR-72555 and AVCO Corporation No. AVSD-0306-69-RR, August 1969.
17. Jeffers, S. L., "Fragment Velocity Measurements from three Project Pyro Experiments," Sandia Laboratories Report No. SC-DR-69-329, June 1969.
18. "Preliminary Safety Analysis Report, Separately Launched Multiuse Space Electrical Power System," v. 3 RDR, GE document GESP-7057-3, August 1970.
19. "Apollo Recovery Operations Manual," MSC-01856, Rev. D, March 1972.
20. Petersen, T. F., "TAC2D, A General Purpose Two-Dimensional Heat Transfer Computer Code," Users Manual, Gulf General Atomic Report No. GA-8868, September 1969.
21. Bradshaw, G. B., Personal communications with Dr. Leonard Topper, USAEC Space Nuclear Systems Office, and Dr. Thomas Bustard and Harold Barr of Hittman Assoc., Inc., January 1972.
22. Princiotta, F. T., and H. N. Barr, "Further Development of Thermal Switch Composite Reentry Protection Material," Trans. of the Am. Nuc. Soc., Los Angeles, July 1970.
23. Metals Handbook, v. 1, "Properties and Selection of Metals," American Society for Metals, Metal Park, Ohio, 1967.
24. Rasuch, T. R., "Aerodynamic Analysis of an Entry Capsule for Radioactive Materials," General Dynamics/Convair Report TN-67-AE-06, February 1967.
25. Wybomy & Kabelitz, J. Spacecraft, v. 8, No. 8, August 1971, pp. 893-895.
26. O'Neil, R. F., et al., "Variable-Boundary II Heat Conduction Program" General Dynamics/Convair Report No. GDC-BTD67-004, August 1967.
27. Detra, Kemp and Riddell, "Addendum to Heat Transfer to Satellite Vehicles," Jet Propulsion v. 27, No. 12, December 1957.
28. Fay and Riddell, "Theory of Stagnation Point Heat Transfer in Dissociated Air," J. Aeron. Sci. v. 25, No. 2 (1958).
29. Nerem, R. M., and G. H. Stickford, "Shock Layer Radiation During Hypervelocity Reentry, AIAA Publication CP-9, October 1964.

30. Holden, M. S., "Shock Wave-Turbulent Boundary Layer Interaction in Hypersonic Flow," AIAA Paper No. 72-74, January 1972.
31. Bramer, S. E., H. Lurie, and T. H. Smith, "Reentry Protection for Radioisotope Heat Sources," NAS 16th Annual Meeting, June 1970.
32. Scala, S. M., and L. M. Gilbert, "The Sublimation of Graphite at Hypersonic Speeds," AIAA Publication CP-9, October 1964.
33. Brentjes, T., "Honeycomb as an Energy Absorbing Material," Hexcel Reprint from the 8th Structures, Structural Dynamics and Materials Conference, March 1967.
34. Puthoff, R. L., and K. H. Gunto, "Parametric Study of a Frangible Tube Energy Absorption System for Protection of a Nuclear Aircraft Reactor," NASA TN D-5730, March 1970.
35. Bradshaw, G. B., personal communication with Richard Puthoff, NASA-Lewis (216-433-4000 x 6619), February 1972.
36. Puthoff, R. L., "A 640 ft/sec Impact Test of a Two-Foot Diameter Model Nuclear Reactor Containment System Without Fracture, NASA TM X-67997.
37. Young, C. W., "The Development of Empirical Equations for Predicting Depth of an Earth-Penetrating Projectile," Sandia Corporation Report No. SC-DR-67-60, May 1967.
38. "Guide to the Safe Design, Construction and Use of Radioisotope Power Generators for Certain Land and Sea Applications," Safety Series No. 33, International AEC, 1970.
39. Buzzeli, G., personal communication with A. C. Schaffhauser, ORNL.
40. Wagner, R. L., "Sublimation of Tungsten-25% Rhenium between 1650 and 1950°C in Low Pressure Oxygen," in Proceedings of the 1969 Thermionic Conversion Specialist Conference, Held by the Institute of Electrical and Electronics Engineers, Wash., D.C., Oct. 21-23, 1969, pp. 411-416 (69C 51 ED).
41. Di Stefano, J. R., "Compatibility of $^{244}\text{Cm}_2\text{O}_3$ with Refractory Metals at Thermionic Temperatures," Proceedings of the 1970 Thermionic Conversion Specialist Conference, Held by the Institute of Electrical and Electronics Engineers, Inc., Las Vegas, Oct. 26-29, 1971, pp. 26-33 (70C 53-ED).
42. Aitken, E. A., et al., "Permeability of Tungsten to Hydrogen from 1300° to 2600°C and to Oxygen from 2000° to 2300°C," Transactions of the Metallurgical Society of AIME, v. 239, October 1967, pp. 1565-1571.